

VO₂ Material Study and Its Application for Terahertz Modulation

by

Yong Zhao, B.S.

A Dissertation

In

Electrical and Computer Engineering

Submitted to the Graduate Faculty
of Texas Tech University in
Partial Fulfillment of
the Requirements for
the Degree of

DOCTOR OF PHILOSOPHY

Approved

Prof. Zhaoyang Fan
Chair of Committee

Prof. Ayrton Bernussi

Prof. Mark Holtz

Prof. Sergey Nikishin

Dominick Casadonte
Interim Dean of the Graduate School

August, 2013

Copyright 2013, Yong Zhao

ACKNOWLEDGEMENT

First and foremost, I thank Prof. Zhaoyang Fan, my advisor and chair of my Ph.D committee for his persistent support and professional instruction. I appreciate the opportunity and resources he offered that allowed me to work at the forefront of semiconductor materials and devices.

I am grateful to the other three of my committee, Prof. Ayrton Bernussi, Prof. Mark Holtz and Prof. Sergey Nikishin for their contribution of time, expertise, thoughtful discussions and helpful advice.

I would like to thank my collaborators, Dr. Yanhan Zhu for her help with THz measurements and Dr. Nazari Mohammad for Raman spectroscopy.

I am obliged to Dr. Changhong Chen for introducing me to the world of VO₂, Dr. Vladimir Kuryatkov for persistent technical help, Dr. Wen Feng for photo-lithography instruction, Dr. Shawn Xu for his help with dry-etch and Mahesh Pandikunta for XRD instruction. I also want to take this opportunity to thank Dr. Sixuan Jin and Weiping Zhao for their advices on semiconductor device fabrication.

Special thanks to my colleague, Dr. Xuan Pan for her help and accompanying, without whom my life here would be much less enjoyable; I also thank Nadim Hoque and Guofeng Ren for making it a good team to stay in.

Thank everyone in Electrical Engineering Department and Nano Tech Center for all your help.

Finally I want to thank my parents and my younger brother for their support and understanding. They are my ultimate momentum and deserve all the credit for whatever I have been able to achieve today.

TABLE OF CONTENS

ACKNOWLEDGEMENT.....	iii
ABSTRACT.....	vii
LIST OF TABLES.....	ix
LIST OF FIGURES	x
Chapter 1 Introduction.....	1
1.1 Mott insulator and metal-insulator transition.....	1
1.2 MIT in Vanadium dioxide (VO ₂)	3
1.2.1 Crystal structure of VO ₂	3
1.2.2 Band structure of VO ₂	4
1.2.3 VO ₂ MIT and its optical modulation characteristics	5
1.2.4 VO ₂ thin films synthesis and applications.....	7
Chapter 2 Experimental Tools and Techniques.....	9
2.1 Reactive magnetron sputtering	9
2.2 X-ray diffractometer	11
2.3 Raman spectroscopy	12
2.4 Device fabrication techniques.....	14
2.4.1 Photolithography.....	14
2.4.2 Dry-etching and e-beam evaporation.....	15
2.4.3 Device fabrication flow diagram.....	15
2.5 Electrical transport measurements	17
2.5.1 Van der Pauw measurement	17
2.5.2 Hall measurement	18
2.6 Terahertz time domain spectroscopy (THz-TDS).....	19
Chapter 3 Structural and Electrical Properties of Polycrystalline VO₂ Thin Films Grown under Different Temperature.....	21
3.1 Abstract.....	21
3.2 Introduction	21
3.3 Experiment	22
3.3 Results and Discussion	23
3.4 Summary.....	30

Chapter 4 Structural, Electrical and Optical Properties of VO₂ Grown on c-cut Sapphire	31
4.1 Introduction	31
4.2 XRD characterization and structural analysis.....	32
4.2.1 XRD θ-2θ scan (in-axis scan).....	32
4.2.2 XRD off-axis scan.....	33
4.2.3 Explanation for off-axis Φ scan results.....	35
4.3 SEM and TEM analysis	37
4.4 Electrical properties.....	38
4.5 Optical properties	39
4.6 Summary.....	42
Chapter 5 Electric Voltage Triggered MIT in VO₂ Two- Terminal Devices	43
5.1 MIT under voltage sweeping	43
5.1.1 Introduction.....	43
5.1.2 Device size effects on MIT of VO ₂ two terminal devices.....	43
5.1.2 Temperature effects on MIT in VO ₂ two terminal devices.....	45
5.2 MIT under voltage pulse stimulation.....	46
5.2.1 Introduction.....	46
5.2.2 Experiments	46
5.2.3 Results and Discussion	47
5.3.4 Summary.....	51
Chapter 6 Electric Current Controlled MIT in VO₂ Thin Films.....	52
6.1 Abstract.....	52
6.2 Introduction	52
6.3 Experiments	53
6.4 Results and Discussion	54
6.5 Summary.....	57
Chapter 7 Structural, Electrical, and Terahertz Transmission Properties of VO₂ Thin Films Grown on c-, r-, and m-plane Sapphire Substrates.....	59
7.1 Abstract.....	59
7.2 Introduction	59
7.3 Experiments	61
7.4 Results and Discussion	63
7.5 Summary.....	75

Chapter 8 Tuning Properties of VO₂ Thin Films Through Growth Temperature for IR and THz Modulation	77
8.1 Abstract.....	77
8.2 Introduction	78
8.3. Experiments	79
8.4 . Results and Discussion	80
8.5. Summary:	89
Chapter 9 Electric Current Controlled THz Spatial Light Modulator Based on Metal-Insulator Transition in Sputtered VO₂ Thin Films.....	91
9.1 Abstract.....	91
9.2 Introduction	91
9.3 Experiment	93
9.4 Results and discussion	93
9.5 Conclusion.....	99
Reference	101

ABSTRACT

Metal-insulator transition (MIT) in vanadium dioxide (VO_2) can be triggered by different mechanisms, and the resulted electronic conductivity variation of 4-5 orders of magnitude is accompanied by dramatic optical properties change. This makes VO_2 a promising material for optical modulation and switching, especially in terahertz (THz) range. This dissertation work focuses on VO_2 thin-film growth study, property characterization, and its application for THz wave modulation with the aim to achieve a large modulation depth.

Using reactive sputtering method, epitaxial VO_2 thin films was deposited on *c*-cut sapphire substrates. The film was characterized to be (010) oriented multi-domain hetero-epitaxial structure based on high-resolution x-ray diffraction study. In transmission mode, a 95% THz modulation depth was found for ~ 150 nm thick VO_2 film across its MIT.

The sapphire substrate orientation (*c*-, *r*- and *m*-cut sapphire) influence on structural, electrical and THz properties of VO_2 thin films was systematically studied, and *r*-cut samples was found to have the best THz modulation performance. Growth temperature influence on material properties and optical modulation was investigated. It was found that introduction of intrinsic vanadium or oxygen vacancies, simply by adjusting growth temperature, the electrical and optical properties of VO_2 can be effectively tuned for better device applications.

MIT in VO_2 thin films triggered by electric method was investigated based on 2-terminal devices. Voltage sweeping test unveiled a critical current density at the occurrence of MIT, and voltage pulse measurement demonstrated fast transition within sub-microsecond. Moreover, current sweeping test displayed a 3-stage transition process, which offers the possibility to gradually control the transition process.

As initial demonstration, two types of 2×2 pixel THz spatial light modulator (TSLM) were demonstrated. TSLM1 was controlled through electrical Joule heating effect, and TSM2 was directly controlled by electric current. Both TSLMs were

demonstrated to be able to independently turn on and off individual pixels, and display reasonable uniform modulation. In comparison, TSLM2 suffered less influence from thermal cross-talk and displayed a superior modulation depth up to 99%, showing great potential for future THz signal and image processing.

LIST OF TABLES

Table I Summary of different insulators	2
Table II Comparison of THz modulation performance, electrical properties at 300 K, and MIT properties of the three samples	64

LIST OF FIGURES

FIG. 1.1 Lattice structures of <i>R</i> -phase and <i>M</i> -phase VO ₂	3
FIG. 1.3 Resistivity-temperature (R-T) hysteresis curve of a typical VO ₂ thin film during cooling and heating cycles. Inset plot is the differential of log (ρ). .	5
FIG. 1.4 UV-VIS-NIR transmittance spectra of ~120nm VO ₂ thin film at different temperature.....	7
FIG. 2.2 (a) Principle of x-ray diffraction and (b) schematic of XRD system. .	11
FIG. 2.3 Schematics of (a) Rayleigh scattering, (b) Stokes and (c) anti-Stokes Raman scattering.....	14
FIG. 2.4 Standard process to fabricate VO ₂ two-terminal devices.	16
FIG. 2.5 Schematics of (a) Van der Pauw method and (b) Hall measurement..	18
FIG.2.6 Typical THZ-TDS schematic setups used for VO ₂ thin films transmission measurement.	20
FIG. 3.1 XRD 2θ scan of VO _x thin films sample grown at different O ₂ /Ar ratio.	
24	
FIG. 3.2 (a) XRD 2θ glancing scan patterns for VO ₂ /Si ₃ N ₄ /Si sample grown at 575°C. Inset plot is SEM image of the sample surface morphology. (b) R -T hysteresis curves acquired from Van der Pauw method.	25
FIG. 3.3 R-T hysteresis curves for S1-S5 samples. The inset plot shows the differentials of log (ρ) during heating cycle.	27
FIG. 3.4 (a) Average carrier density and carrier type for S1-S5 samples at room temperature and (b) ln(ρ) vs (kT)-1 plots for S1-S5 samples in low-temperature at 282K≤T≤300K.	28
FIG. 3.5 (a) Single Peak 2θ scan of the (011) peak, and (b) ΔE_a dependence of strain along the am axis in S1-S5 samples.....	29
FIG. 4.1 XRD θ-2θ scan patterns of as-grown VO ₂ epitaxial films on c-cut sapphire substrate.....	33
FIG. 4.2 (a) Off-axis VO ₂ (011) plane Φ scan and Al ₂ O ₃ (1̄102) plane, and (b) off-axis VO ₂ (220) plane.....	34
FIG. 4.3 (a) The schematic configuration of atoms at the interface between the VO ₂ thin films and the sapphire substrate. (b) 3 possible arrangements of VO ₂ domains, D1-D3.....	36

FIG. 4.4 Schematic diagram for the origination of sixfold and twin-peak for VO ₂ (011) planes and 3 peaks for Al ₂ O ₃ (1̄102) plane during off-axis Φ scan.....	37
FIG. 4.5 (a) High resolution TEM image of the film-substrate interface area. Inset shows the SEM image of the VO ₂ films surface morphology. (b) SAED pattern along the sapphire [10̄10] zone axis.	38
FIG. 4.6 R-T curves of VO ₂ thin films grown on c-plane measured during heating and cooling process.	39
FIG. 4.7 (a) Time-domain and (b) frequency-domain THz transmission of VO ₂ thin films on c-cut sapphire.....	40
FIG. 4.8 Measured THz field amplitude transmission vs temperature for VO ₂ thin films grown on c-cut sapphire. The solid curves are simulated transmission.	
41	
FIG. 5.1 V-I characteristics of VO ₂ thin films based two-terminal devices: (a) device group with fixed gap width but varied gap length and (b) device group with fixed gap length but varied gap width.	44
FIG. 5.2 V-I characteristics of VO ₂ two-terminal devices at different temperature.	
45	
FIG. 5.3 Voltage response of a two-terminal VO ₂ device under electric pulses. The inset plot is the diagram of circuits setup.	47
FIG. 5.4 Voltage over VO ₂ two-terminal device under varied pulses period....	48
FIG. 5.5 Voltage over VO ₂ two-terminal devices under varied pulses width at room temperature (25 °C).....	49
FIG. 5.6 Voltage over VO ₂ two-terminal devices under varied pulses amplitude at room temperature (25 °C).....	50
FIG. 5.8 Voltage over VO ₂ two-terminal devices under different substrate temperature.	51
FIG. 6.1 Voltage drop on a representative two-terminal device ($L=20\ \mu\text{m}$, $W=120\ \mu\text{m}$) with injected current ramped up. The inset is the optical microscopic image of VO ₂ channel at E point, and the dark color current path is clearly observable.	55
FIG. 6.2. (a) Micro-Raman spectra along the current path at different injected current, and (b) its zoom-in view of selected modes. (c) Micro-Raman spectra for the area out of the current path, and (d) its zoom-in view of selected modes. The spectra were shifted in vertical direction for clear view.....	57
FIG. 7.1 Representative (a) time-domain and (b) frequency-domain THz transmission of VO ₂ thin-film on sapphire substrate (R-sample). Only the	

dominant peak in (a) was used in the Fourier transformation to obtain the frequency-domain transmission in (b).	64
FIG. 7.2 Resistivity vs. temperature for the three samples through the MIT process.....	65
FIG. 7.3 The surface morphology of the three samples (a) C-sample, (b) R-sample, and (c) M-sample observed by SEM.....	66
FIG. 7.4 XRD patterns of VO ₂ thin film on <i>c</i> -sapphire. (a) In-plane θ-2θ scan, (b) Off-axis (011) plane Φ scan, and (c) Off-axis VO ₂ (220) plane Φ scan.....	68
FIG. 7.5 TEM study of C-sample: (a) Cross-sectional TEM image, and (b) SAED pattern along <i>c</i> -sapphire [1010] zone	69
FIG. 7.6 XRD patterns of VO ₂ thin film on <i>r</i> -sapphire. (a) In-plane θ-2θ scan (b) θ-2θ scan for (211)/(200) peak at room temperature and (011) _T peak at 353 K.	70
FIG. 7.7. TEM study of VO ₂ on <i>r</i> -sapphire: (a) cross-sectional TEM image, (b) HRTEM image of interfacial region, and (c) SAED pattern from the VO ₂ -sapphire interface with sapphire in zone [2201] and VO ₂ from zone [111].	
71	
FIG. 7.8. VO ₂ thin-film grown on m-cut sapphire: (a) in-plane θ-2θ scan , Cross-section TEM image, and (c) HRTEM image of VO ₂ -sapphire interfacial region.	73
FIG. 7.9. Room-temperature measurement of Raman Spectra for the three samples.....	74
FIG. 8.1 SEM images of surface morphology for all 7 samples.....	81
FIG. 8.2 (a) Typical XRD 2θ–θ full scan patterns for VO ₂ epitaxially grown on <i>c</i> -cut sapphire, and (b)-(h) are high-resolution scan of VO ₂ (020) peak for all 7 samples, with peak intensity normalized for comparison.....	83
FIG. 8.3 Sub-peak position of VO ₂ (020) for samples grown vs their substrate growth temperature.	84
FIG. 8.4 Resistance-Temperature (R-T) curves of all 7 samples.	85
FIG. 8.5 Optical modulation performance of S575, S625 and S700: (a) NIR transmittance across the MIT process at $\lambda = 3 \mu\text{m}$, (b) THz time-domain responses at insulating and metallic states and (c) insertion loss and modulation depth calculated with data from (a) and (b).	89
FIG. 9.1 (a) R-T curves of two VO ₂ thin films samples and the inset plot shows the respective differentials of log (ρ) during heating cycle. (b) Shows the THz-TDS response of these two VO ₂ thin films samples at 300K and 363K. Black arrow indicates the reflected THz peaks from the samples.	94

FIG. 9.2 (a) Device diagram of TSLM1. (b) THz-TDS response of the pixel with varied current injection. (c) Gray graph of THz-TDS raster-scan with two pixels turned off and 0.5 mm scan step. (d) Thermal cross-talk influence on THz transmittance of ‘on’ pixel under current injection of 80 mA..	96
FIG. 9.3 (a) Device diagram of TSLM2. (b) THz-TDS response of the pixel under current injection. (c) Gray graph of THz-TDS raster-scan with one pixel turned off at 580 mA and 0.5 mm scan step. (d) THz response in frequency-domain at selected current value, acquired from Fourier transform of dominant peak in (b).	99

Chapter 1

Introduction

This chapter gives a brief introduction of several theories and mechanisms describing metal-insulator transition (MIT) in varied material systems. The structural phase transition (SPT), band structure, MIT characteristics as well as optical modulation performance of VO₂ thin films were also discussed.

1.1 Mott insulator and metal-insulator transition

Free-electron approximation is a popular model in conventional band theory, which well predicted and explained the band structure, electrical resistivity, optical absorption properties of insulators, e.g., AlN and diamond, as well as undoped semiconductors. In this model, it is assumed that each electron is independent of the motion of other electrons, or in other words, negligible interaction. The electron orbitals introduce Eigen-functions in periodically arranged lattice structure, which extend through the lattice and open up energy gap to form energy bands.¹ This type of semiconductors is normally referred as band insulator, or Bloch-Wilson insulator.

However, for correlated matter system, especially for some transition metal oxides, e.g, NO, V₂O₃, the free-electron model fails to explain the conduction properties of the materials. According to the conventional band theory, those highly correlated materials should behave conductively as metals but actually act as insulators. The failure of free-electron model on those materials stems from the fact that it did not take into account the strong electron correlation effect. This is particularly true for transition metal oxides having *d* electrons and with wave-functions localized at each atomic site, which produce strong many-body electron-electron interaction. Insulators falling into this category are

often referred as Mott-insulator or Mott-Hubbard insulator.²⁻⁴

In a Mott insulator, the main electron interactions are kinetic energy and Coulombic repulsive energy, both of which are a function of the carrier density. When carrier density is dilute, the dominant repulsive interaction results in electron localization, and the material system will behave as an insulator; however, when the carrier density reaches some critical value, the kinetic energy will dominate and generate itinerant electrons, and hence the material transits into metallic phase (conductive behavior). The critical carrier density n_c is proposed by Mott and referred as Mott criterion:^{2, 5}

$$(n_c)^{1/3} \alpha_B \approx 0.25 \quad (1)$$

Where α_B is the Bohr radius, and n_c is the critical carrier density and estimated to be in the order of 10^{18} - 10^{19} cm⁻³ for Mott insulator. The interesting phase transition in Mott-insulator, during which it transits from an insulator to a metal (or vice versa), is defined as metal-insulator transition (MIT).

Table I Summary of different insulators.

Insulator type	MIT origination	Typical materials
Band Insulator	Conventional band theory, no MIT	Diamond, GaN
Mott-Hubbard Insulator	Electron-electron correlation	NiO, V ₂ O ₃
Peierls Insulator	Electron-phonon (lattice) interaction	K _{0.3} MoO ₃ , (TaSe ₄) ₂ I
Anderson Insulator	Disorder-induced electron localization	Heavily doped Si

Besides Mott's theory, several other theories were also proposed to explain the MIT phenomenon. Peierls suggested that the MIT phenomenon is mainly induced by electron-phonon (electron-lattice) interaction other than electron-electron correlation, which occurs during structure-phase transition (SPT). The SPT reconstructs the ionic position and changes the ionic potential inside oxides, which will open up a band gap for the material system. Insulators which apply to Peierls' definition are named as

Peierls insulator.⁶ Anderson also describes a type of insulators undergoing MIT triggered by disorder. In his theory, the introduction of randomly distributed impurities, e.g., defects, can localize Fermi level electron states and leads to transition from conductive phase to insulating states. This type of insulator is defined as Anderson insulator.^{7,8} Table I briefly summarizes the abovementioned four types of insulators.⁹

1.2 MIT in Vanadium dioxide (VO_2)

1.2.1 Crystal structure of VO_2

Vanadium dioxide (VO_2) crystal is well-known for its first-order metal-insulator transition (MIT) when it goes across the critical temperature (T_C) of around 68°C , during which it transits from low-temperature insulating monoclinic phase (M, space group $P2_1/c$) to high-temperature metallic rutile phase (R, space group $P4_2/mnm$), with a sharp resistivity drop up to 4-5 orders of magnitude.¹⁰⁻¹² As shown in Figure 1.1,¹³ VO_2 shows a tetragonal (rutile) structure when it is heated up above transition T_C , denoted as *R*-phase, with each unit cell containing a tetragonal body-centered vanadium atoms surrounded by 6 distorted octahedron oxygen atoms; when the temperature drops below T_C , VO_2 transits into monoclinic structure, denoted as *M*-phase, with vanadium atoms dimerized and paired to form a zigzag chain, and the unit cell volume is also doubled.

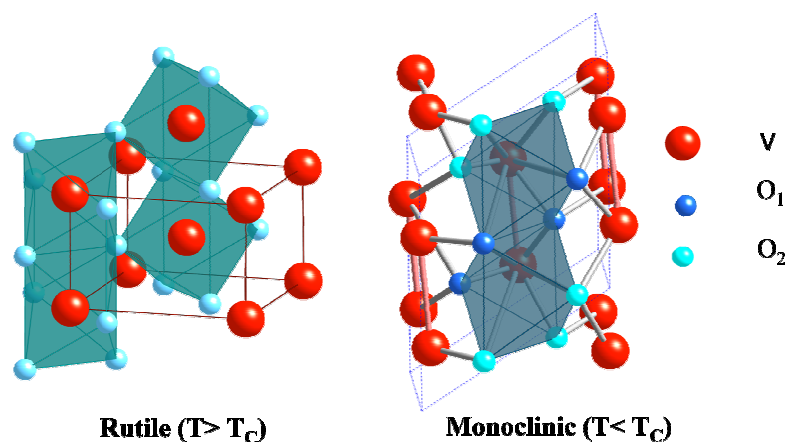


FIG. 1.1 Lattice structures of *R*-phase and *M*-phase VO_2 .

1.2.2 Band structure of VO₂

In VO₂ crystal, each V atom ($4s^23d^5$) was bounded to two O atoms ($2s^22s^22p^4$), and give out four electrons to fill up the O_{2p} energy shells, and only one valence electron was left with V⁴⁺ cations. As shown in Figure 1.2, the O_{2p} electron energy level lies far below the Fermi energy E_F, hence does not contribute to the conductivity of the material. For metallic VO₂, the single electron bound to V⁴⁺ occupies the lowest V_{3d} level, accounting for the R-phase high conductivity. However, during the structural transition from rutile to monoclinic phase, the V-V chain along c-axis of rutile phase dimerizes and forms tilted pairing atom chain, which causes the splitting of V_{3d_{||}} into filled bonding states (V_{3d_{||}}) and empty anti-bonding states (V_{3d_{||}*}).¹⁴ Meanwhile, the V-V pairing increases the overlap of V_{3d_{||}} and empty anti-bonding states (V_{3d_{||}*}).¹⁵⁻¹⁷ Moreover, the V-V pairing increases the overlap of V_{3d_{||}} and O_{3p} states, shifting the o_{3d_π} band to a higher energy levels. As a results, a energy gap is opened up with a measured value to be ~0.6 - 0.7 eV,^{14,18} as illustrated by Fig. 2(b).

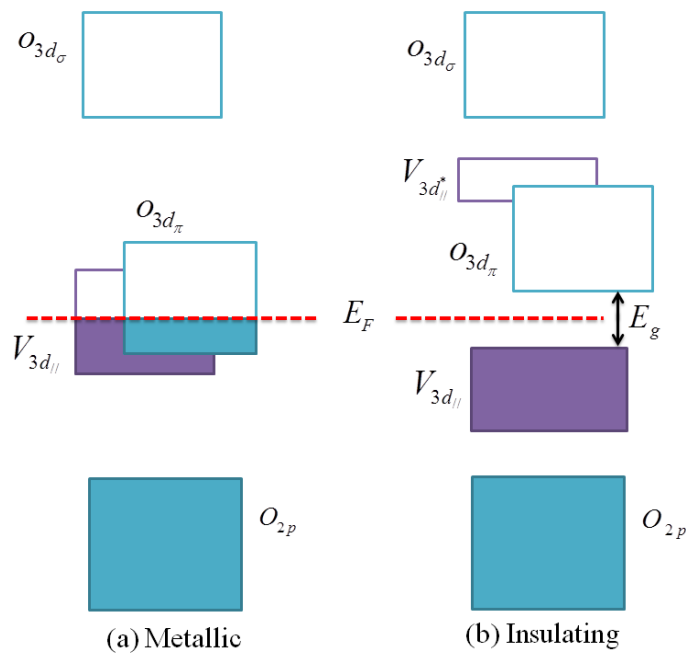


FIG. 1.2 Band structure diagrams for (a) metallic state and (b) insulating state VO₂.

1.2.3 VO₂ MIT and its optical modulation characteristics

As aforementioned, the electrical resistivity of VO₂ undergoes sharp change across the structural phase transition. Figure 1.3 shows a typical VO₂ thin film resistivity-temperature (R-T) hysteresis curve measured during cooling and heating process. The inset plot shows the differential of log (ρ), whose peaks suggest the transition critical temperature, denoted as T_C. Curves for heating and cooling process show two T_C, denoted as T_{C1} and T_{C2}. For convenience, T_{C1} is generally referred as T_C. Several parameters, e.g., resistivity change ratio (ΔR), hysteresis window ($\Delta H = T_{C1} - T_{C2}$), transition slope, transition critical temperature (T_C), are normally used to characterize the MIT performance. It is generally agreed that R-T curves with larger ΔR , sharper transition slope and narrower ΔH indicate better MIT characteristics and hence better crystal quality in VO₂ films. ΔR could reach up to 5 orders in high quality undoped VO₂ crystal with a hysteresis window as narrow as 1~2 K. As for VO₂ thin films, their MIT characteristics are susceptible to films quality,¹⁹ doping,^{20, 21} grain size/boundary,^{22, 23} lattice mismatch built-in strains,^{24, 25} etc.

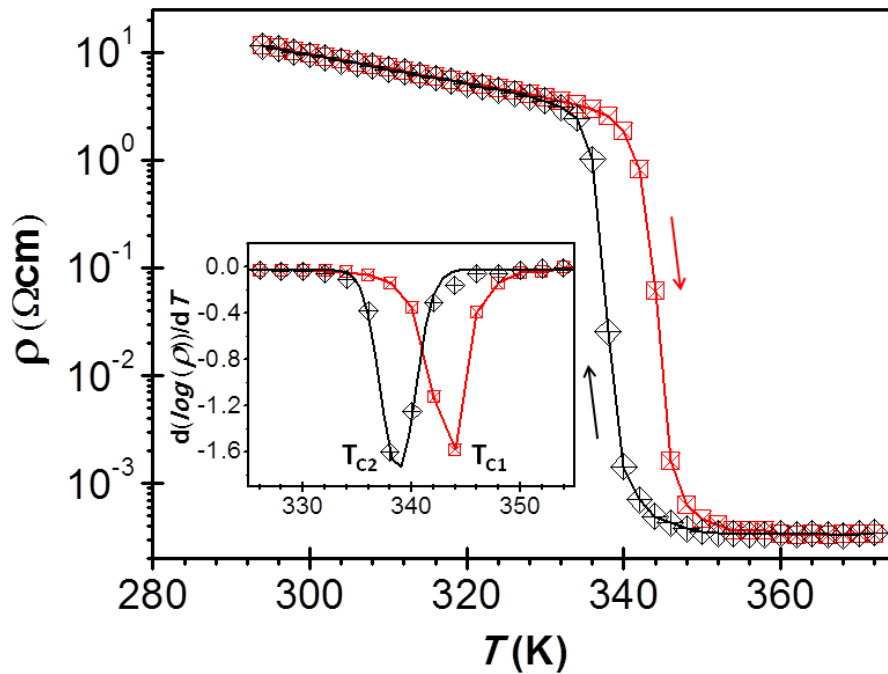


FIG. 1.3 Resistivity-temperature (R-T) hysteresis curve of a typical VO₂ thin film during cooling and heating cycles. Inset plot is the differential of log (ρ).

More interestingly, the MIT in VO₂ is observed to be accompanied by dramatic changes in its dielectric function and optical properties, e.g., transmittance and reflectivity, especially within IR and THz range.²⁶⁻²⁹ At temperature above T_C, the VO₂ material performs metallic behavior and reflects most of the radiation, while at low temperature it transits back to the transparent insulating state with negligible reflection and absorption. Figure 1.4 shows the UV-VIS-NIR transmittance spectra of 120 nm VO₂ grown on c-cut sapphire. Obvious modulation in NIR range could be observed when the temperature raised above T_C.

The dramatic change in optical properties of VO₂ thin films comes from the fact that the carrier density increased by 3 to 4 orders of magnitudes across the MIT, which also accounts for the large resistivity change. At the insulating state, VO₂ has a carrier density on the order of 10¹⁸ to 10¹⁹ cm⁻³, while it increases to ~10²² cm⁻³ after transition. The carriers play a vital role to determine optical conductivity of VO₂ thin films. Increased carriers will intensify the scattering and absorption of photons, which results in reduction in transmittance, as described by the Drude model:³⁰

$$\tilde{\sigma}_{Drude} = \frac{\omega_p^2 \tau_D}{4\pi(1-i\omega\tau_D)} \quad (1)$$

where τ_D is the carrier scattering time, and ω_p is the plasma frequency defined as $\omega_p = 4\pi Ne^2 / m_e$, where N is the carrier density, e is carrier elementary charge and m_e is the effective mass. It is found that except for the large change in carrier density, the mobility and effective mass of carrier do not change too much, which suggest that high-density carriers play a dominant role for optical properties switching. Following the same idea, 2-dimensional electron gas (2DEG) based high electron mobility transistor (HEMT) were also proposed for THz modulation.³¹ However, the transmittance modulation depth is trivial due to the tiny thickness of 2DEG.

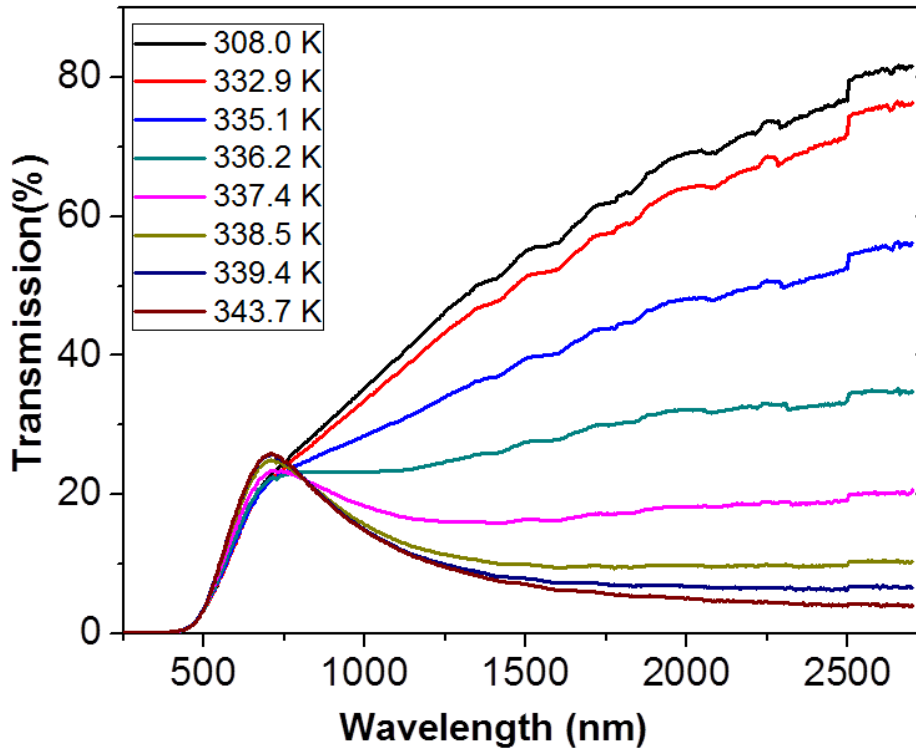


FIG. 1.4 UV-VIS-NIR transmittance spectra of $\sim 120\text{nm}$ VO_2 thin film at different temperature.

The question whether VO_2 is a Mott-Hubbard insulator or a Peierls insulator, or whether the transition is induced by carrier-interaction or by the aforementioned structural change, has been a hot topic of debate for decades. Both views have been supported by certain experimental results and theoretical arguments,³²⁻³⁶ but no final answer has been concluded for this debate yet. This dissertation work is not focused on investigation of the ultimate mechanism that drives MIT in VO_2 , but on effectively controlling the MIT process and optimizing VO_2 thin films growth for THz modulation.

1.2.4 VO_2 thin films synthesis and applications

VO_2 thin films can be synthesized through different methods, including metal-organic chemical vapor deposition (MOCVD),³⁷ physical vapor deposition, e.g., pulsed laser deposition (PLD)^{38, 39} and sputtering^{24, 29, 40}, and sol-gel.^{41, 42} In this work, we employed DC reactive magnetron sputtering for VO_2 thin films growth, which will

be further discussed in Chapter 2. The target we used is a high purity (99.95%) vanadium metal target. Argon/oxygen gas mixture was injected into chamber and maintained at pressure of 3 mTorr. It is well known that vanadium oxides includes a series of complex compounds, such as V_2O_3 , V_2O_5 , which complicates the process to yield pure phase VO_2 . To grow pure phase VO_2 , the oxygen to argon (O_2/Ar) flow ratio as well as the substrate temperature T_S should be precisely controlled.^{43, 44} For our growth, the O_2 / Ar ratio is adjusted at 11% and the substrate temperature was held between 550 °C to 700 °C. SiO_2 or Si_3N_4 coated Si, quartz and glass were normally chosen for polycrystalline VO_2 growth; as for epitaxial growth, sapphires, TiO_2 are two most frequently used substrates. For this work, Si_3N_4 coated Si (100) substrate was used for polycrystalline VO_2 growth and sapphire was chosen for epitaxial films growth.

The unique electrical and optical properties of VO_2 across its MIT make VO_2 a promising material for tunable switching and modulation applications in infrared, THz and even microwave range.^{29, 45, 46} Besides, VO_2 could also be used in other applications, e.g., tunable metamaterials,^{47, 48} varistor,⁴⁹ electronic oscillators,⁵⁰ non-volatile memory^{51, 52} and smart windows⁵³. Highly correlated metal oxides are good candidates to build so-called Mott-FET,⁵⁴ which can take advantage of its much shorter carrier coherence length and can be further scaled down. VO_2 was reported to have a coherence length that as small as 2 nm,⁵ and an extremely fast transition speed that measured to be in sub-picosecond,⁵⁵ which makes it interesting material platform for Mott-FET research.⁵⁶⁻⁵⁸

Chapter 2

Experimental Tools and Techniques

This chapter describes the experimental techniques and instruments that were employed for VO₂ thin films growth, structural, electrical and optical characterization, as well as VO₂ thin film based device fabrication and testing.

2.1 Reactive magnetron sputtering

Figure 2.1 shows basic function diagram of a typical DC reactive magnetron sputtering system. Sputtering deposition system consists of a pair of electrodes: cathode and anode. The target material is placed on the cathode while the substrate is put on the anode position for vapor deposition. Low pressure argon /oxygen gas mixture is injected into chamber and then certain DC voltage is applied to the electrodes to start plasma discharge. As for VO₂ growth, the positive ions in plasma are accelerated in the plasma sheath close to the cathode and then hit the vanadium species out of target. The sputtered vanadium will react with the oxygen on the heated substrate to form VO_x film. Sputtering process controlled by DC power and reactive gas is called DC reactive sputtering. It is noted that for targets that made of insulating materials, radio frequency (RF) power should be applied to the electrodes to achieve effective sputtering. The flux of positive ions will accumulate near the target surface to upset the voltage applied to the electrodes, and consequently block the ions striking on the target. The application of RF voltage to the electrodes will avoid the charge effect on target surface. Sputtering method using RF power source is called RF sputtering. The system used in this work is PVD 75 model from L. J. Lesker Company. It has a magnetron component installed with cathode to confine the plasma close to the target region and substantially improve the sputtering yield. A high purity (99.95%) vanadium metal target was used for sputtering growth. The argon/oxygen mixture gas ambient in

the growth chamber is maintained at a low pressure of 3 mTorr. As aforementioned, vanadium oxides include a series of complex compounds, such as, V_2O_3 , V_2O_5 , and V_3O_7 , which seriously complicates the growth of pure phase VO_2 . To yield high quality VO_2 , O_2 to Ar (O_2 /Ar) flow ratio as well as the substrate temperature should be precisely controlled. The O_2 /Ar ratio was adjusted to be at 11% and the substrate temperature was held between 550 °C to 700 °C in this work. The choice of appropriate substrate also considerably affects the VO_2 crystal growth. SiO_2 or Si_3N_4 coated Si,⁴⁰ quartz⁵⁹ and glass⁶⁰ are normally chosen for polycrystalline VO_2 growth; as for epitaxial VO_2 thin film growth, sapphires and TiO_2 are the two most frequently used substrates. As for epitaxial growth, sapphires and TiO_2 are two most frequently used substrates.^{25, 61} For this work, Si_3N_4 coated Si (100) substrates were used for polycrystalline VO_2 growth and sapphire substrates with varied orientations were used for epitaxial growth.

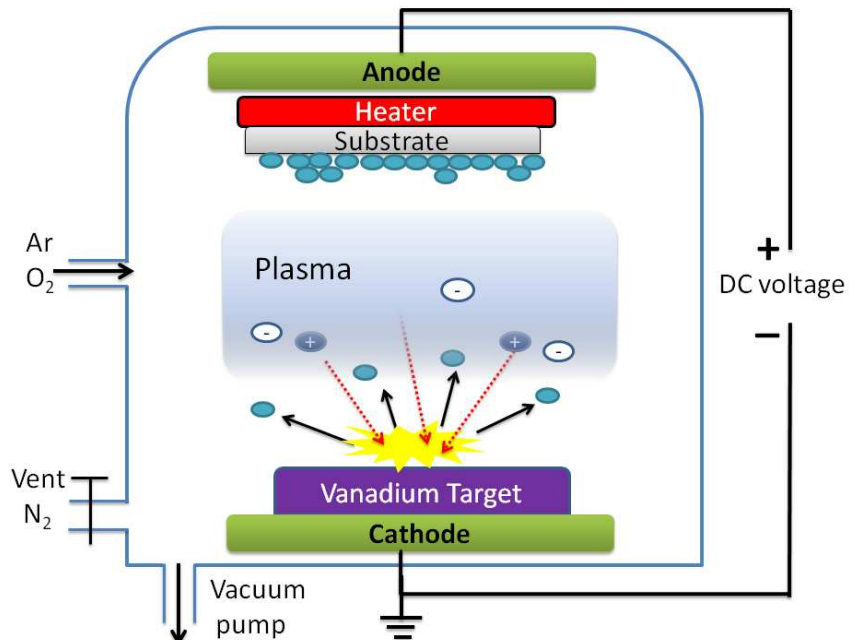


FIG. 2.1 Schematic of a typical reactive magnetron sputtering system.

2.2 X-ray diffractometer

X-ray diffraction (XRD) is used to characterize both polycrystalline and epitaxial thin films. XRD is a powerful non-destructive technique for material phase characterization and a useful tool to investigate crystal structure, grain size, strains, etc. The system employed in this work is a Philips X'pert diffractometer with Cu K- α_1 radiation source at 40 kV/40 mA, with a minimum step size of 0.0001°. The working principle of a typical XRD system is simple. The monochromic X-ray beam with wavelength $\lambda=1.540598$ Å was projected on to a testing material. Assume the lattice spacing for the materials is d , the beam incident angle is θ . According to the Bragg's law, the constructive interference beam will be observed at θ angle when the equation $\sin\theta=n\lambda/2d$ stands, as indicated in Figure 2.2(a).

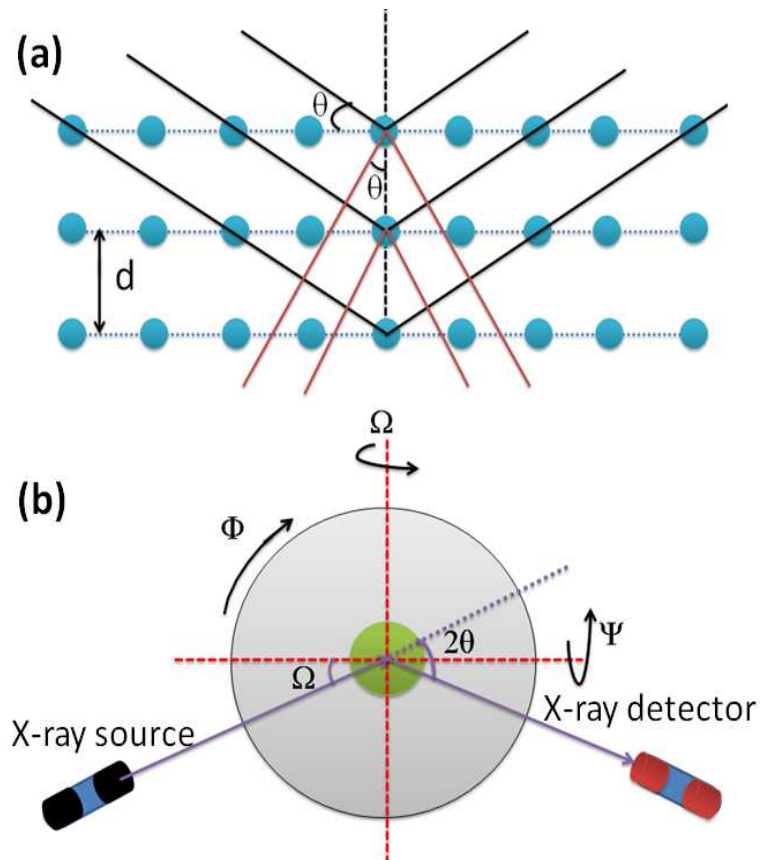


FIG. 2.2 (a) Principle of x-ray diffraction and (b) schematic of XRD system.

The used XRD system is equipped with two detectors: one thin film detector and one triple-axis detector. To conduct phase analysis on polycrystalline thin films, the thin films detector is used and a small incident angle (Ω) was chosen, normally $\Omega = 0.5^\circ$, and XRD 2θ scan that adopts small incident angle is normally called as glancing method. However, for epitaxial thin films, the tripe axis detector is used, and $\theta - 2\theta$ scan mode is chosen for measurement, as indicated in Figure 2.2(b).

2.3 Raman spectroscopy

Raman spectroscopy is a spectroscopic technique used to observe vibrational, rotational and other low-frequency phonon modes in a material system, which detects the inelastic scattering, or Raman scattering that generated when a laser beam is shed on the material. Raman scattering, also known as Raman effect, is the inelastic scattering of a photon. It was first discovered by Sir C. V. Raman that when photons are scattered from atoms or molecular, most phonons scattered photons still maintain the same kinetic energy and wavelength, and scattering following into this category is defined as Rayleigh scattering or elastic scattering, as shown in Figure 2.3(a); on the other hand, a small fraction of the scattered photons are scattered by an excitation, so that the scattered photons having a frequency change (energy change) compared with the incident photon, this type of scattering is named as Raman scattering. The energy of photons underwent Raman scattering can be either increased (blue-shift) or decreased (red-shift). The scattering that lowers down the photon energy is defined as Stokes Raman scattering, while the one that increase the photon energy is known as anti-Stokes Raman scattering. At a given temperature, the anti-Stokes scattering occurs with a much smaller probability than Stokes scattering. The schematic diagram of Raman scattering is shown in Figure 2.3, in which hv_0 is the original energy of incident photons, hv_{vib} is the energy of vibration mode involved in Raman scattering. The Raman scattering process involves the emission (Stokes) or absorption (anti-Stokes) of

an optical phonon. It is found that the energy change in Raman scattering corresponds to the energy variation between two resonant states in the material, and is independent of the absolute energy of the incident photon. During Raman spectroscopy, the original incident photons were filtered out and the energy difference resulting from the Raman scattering were detected formed the so-called Raman spectrum.

Since VO_2 undergoes structural-phase transition (SPT) during heating and cooling across its critical temperature, hence its vibrational spectrum will also dramatically changes correspondingly. In this method, Raman spectroscopy can be employed to investigate the mechanism of metal-insulator transition in VO_2 thin film as well as the material composition analysis, when measured under different temperature. Moreover, since Raman spectroscopy employs laser beams for probing, whose beam size could be in micrometer scale, it could be used for micro-scale material investigation and system like that is called Micro-Raman system. For the micro-Raman system used in this study, a confocal Raman microscope was equipped with the spectroscopy system to focus the laser beam into a few microns and so that it can be used to probe micro-scale structural information for VO_2 thin films, especially for investigating the channel area of VO_2 two-terminal devices. For all the Raman measurement in this work, a small laser power of a few mWs was used for probing, so that the thermal heating effect of the laser beams could be minimized. Two kinds of measurements were conducted: (1) Raman spectrum change of VO_2 in two-terminal devices under varied current injection condition; and (2) Raman spectrum of VO_2 thin films grown at different conditions at room temperature.

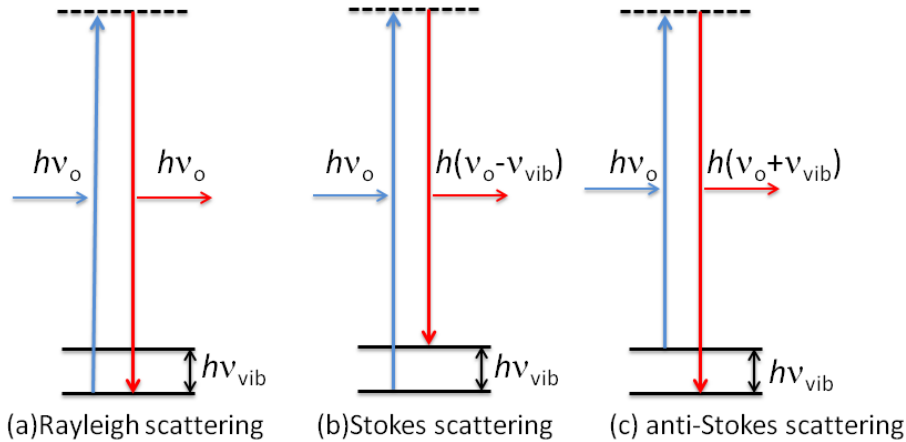


FIG. 2.3 Schematics of (a) Rayleigh scattering, (b) Stokes and (c) anti-Stokes Raman scattering.

2.4 Device fabrication techniques

2.4.1 Photolithography

Photolithography plays a vital role in micro- and nanoscale device fabrication to transfer sub-micron patterns onto a substrate. Standard photolithography steps consist of sample rinsing, photoresist coating, prebake, UV exposure, development. The photoresist used in this work is S1813 (Rohm and Haas Electronic Materials LLC) positive photoresist, which means the UV exposed pattern area will be removed during development with MF319 Microposit developer (Rohm and Haas Electronic Materials LLC). The mask aligner and UV exposure system (ABM Inc.) consists of 365 nm and 400 nm two UV wavelengths, and the latter one is selected. The photolithography procedures are summarized as following:

- 1) Sample cleaning: sample surface was rinsed in acetone, isopropanol and then DI water with the assistance of sonication;
- 2) Photoresist coating : S1813 was coated onto the sample surface by spinning method at 3500 rpm for 30 seconds;
- 3) Pre-bake (softbake): sample was transferred to an oven or a hotplate and

baked for 2~3 minutes at 115 °C;

- 4) UV exposure: the cooled sample were aligned to a mask using a mask aligner and exposed to UV light for around 7.5 seconds;
- 5) Development: after exposure, the sample was quickly developed in MF319 developer for 45 to 50 seconds, and then the sample was blown dry using air gun. Samples now are ready for e-beam evaporation to form metal contacts.
- 6) Post-bake (optional): As etching mask, another time of bake is necessitated after developing to strengthen the photoresist so that it can serve as etching mask.

2.4.2 Dry-etching and e-beam evaporation.

Samples with patterned photoresist layer can be loaded into the dry-etching system to etch away the extra VO₂ to form device mesa. The ICP/ RIE dry-etching system (Oxford Plasmalab 80 plus) was used. For dry etching process, RF power of 150 W and ICP power of 300 W were selected. Cl₂ (5 sccm) and Ar (25 sccm) gas mixture were conducted into chamber to form plasma, and the total pressure in chamber was maintained at 5 mTorr. The achieved etch rate is around 30 nm per minute. A customized e-beam evaporator was used for metal deposition. 20 nm titanium and 120 nm gold stacks (Ti /Au) were deposited to form good ohmic contacts on VO₂ thin film.

2.4.3 Device fabrication flow diagram

Figure 2.4 shows standard process steps to fabricate a two-terminal device on VO₂ thin films, which involve two photolithograph steps, once dry etching and e-beam evaporation steps.

- (1) spin-coating of S1813 photoresist;
- (2) UV exposure through mesa mask;
- (3) developing in MF 319 to remove exposed photoresist;

- (4) ICP/RIE dry-etch to remove extra VO₂ and form mesa;
- (5) remove residual photoresist in acetone;
- (6) Second spin-coating of S1813;
- (7) UV exposure through contact mask;
- (8) development in MF319;
- (9) e-beam evaporation of Ti/Au metal films and
- (10) lift-off in acetone to remove photoresist with assistance of sonication.

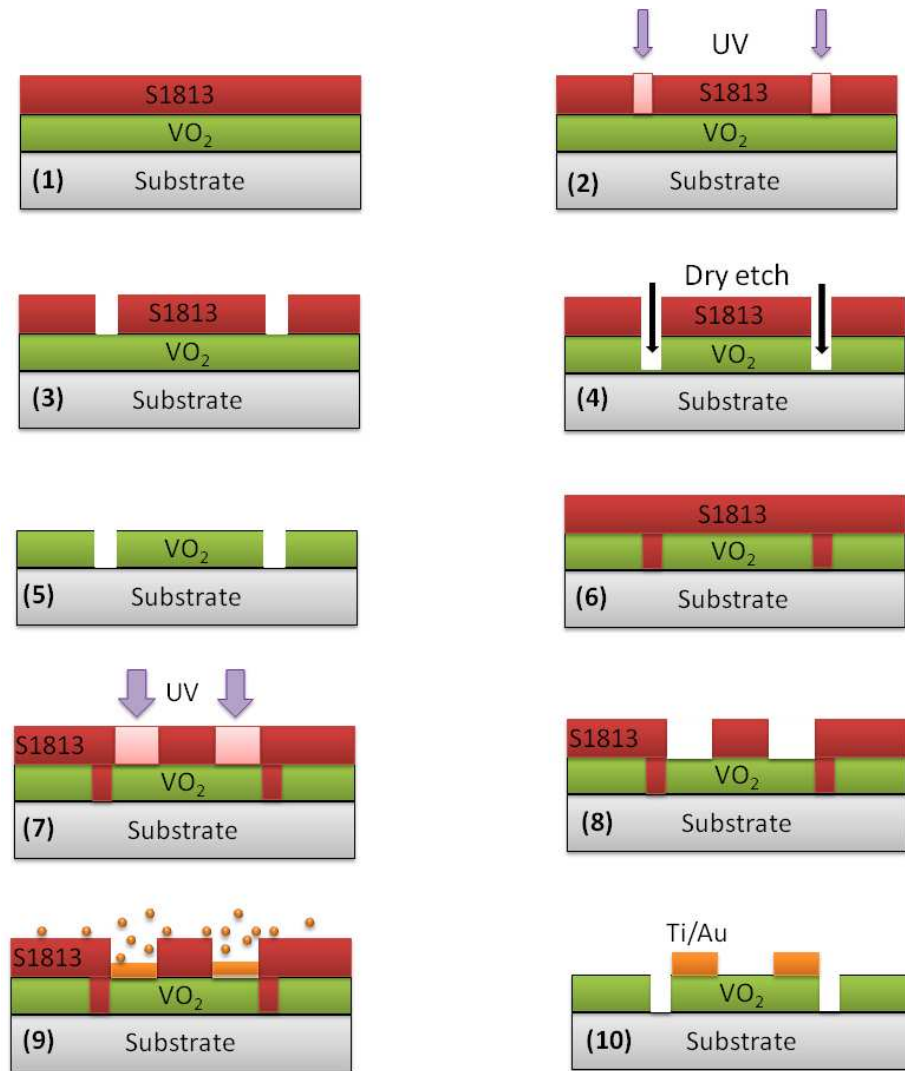


FIG. 2.4 Standard process to fabricate VO₂ two-terminal devices.

2.5 Electrical transport measurements

2.5.1 Van der Pauw measurement

The resistivity of VO₂ thin film was measured using Van der Pauw method. Four symmetric Ti/Au contacts were deposited onto corners of each VO₂ samples through standard photolithography, deposition, and lift-off techniques. A schematic of our square sample for Van der Pauw testing is shown in Figure 2.5(a). Four contacts are denoted as 1, 2, 3, 4, respectively.

An appropriate current is firstly applied through two adjacent contacts; meanwhile a voltage will be measured across the other two contacts. For example, I₁₂ indicates the current flowing from contact 1 to 2, and the voltage measured across contact 3 and 4 is denoted as V₃₄, the corresponding resistance calculated from Ohm's law is defined as : R_{12, 34} = I₁₂ / V₃₄. Similarly, the value of R_{23, 41} could also be measured. According to van der Pauw's discovery, the resistivity of thin films could be calculated using following equations:

$$\rho = \frac{\pi d F (R_{12,34} + R_{23,41})}{2 \ln 2} \quad (2)$$

Where *d* is the thickness of VO₂ thin films, and *F* is a factor that related with the symmetry of the sample contacts. For the measurement of resistivity-temperature curves, samples were placed onto a program-controlled thermal stage, and thermal paste was put between VO₂ sample and thermal stage to maintain good thermal conduction. The system has a temperature resolution of 0.01 K, and for measurement below room temperature, nitrogen gas was injected into the high-vacuumed case for refrigeration. Theoretically the nitrogen refrigeration can achieve a temperature as low as 77 K. During cooling and heating process, a constant temperature step of 2 K and a soaking time of 3 minutes were used.

2.5.2 Hall measurement

Van der Pauw method is the method to measure the resistivity of thin film. However, to extract other parameters such as carrier mobility, carrier density, hall coefficient, etc., Hall measurements need to be conducted instead. Hall measurement has the identical circuit setup as Van der Pauw method, the only difference is that a varied high magnetic field should be applied normal to the sample surface, as illustrated in Figure 2.5(b). Firstly, the magnetic field was set at B_1 , $R_{13,24}$ and $R_{23,41}$ were measured; then the magnetic was changed to be B_2 (for our system, a reverse B_1 filed was used), and the system re-measure $R_{13,24}$ and $R_{24,31}$. The difference of these two resistance from two measurements were calculated and denoted as $\Delta R_{13,24}$ and $\Delta R_{24,31}$. Then the carrier mobility can be acquired using following equation:

$$\mu = \frac{10^8(\Delta R_{13,24} + \Delta R_{24,31})d}{2\rho\Delta B} \quad (3)$$

where $\Delta B=B_2-B_1$, and resistivity ρ is acquired from the Van der Pauw method. Assuming the carriers are electrons with elementary charge of q , the carrier density is given by:

$$n = \frac{1}{\rho q \mu} \quad (4)$$

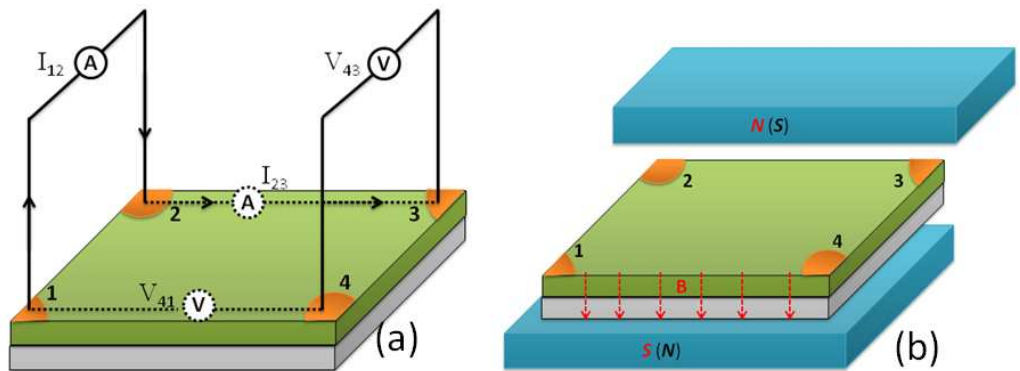


FIG. 2.5 Schematics of (a) Van der Pauw method and (b) Hall measurement.

Other parameters such as Hall coefficient, sheet carieer density, sheet resistivity

and carrier type can also be determined through Hall measurements.

2.6 Terahertz time domain spectroscopy (THz-TDS)

Terahertz time-domain spectroscopy is a powerful non-destructive technique for materials' property investigation, chemical detection and biomaterial study. Figure 2.6 shows the schematic setup for the system (MenloSystem GmbH) used for VO₂ thin film testing. An ultrafast fiber laser emits 1560 nm radiation beam, which is divided into two parts: the first part is projected to the low-temperature InGaAs/InAlAs multilayer photoconductive antenna to generate 90 fs THz pulses at 100 MHz repetition rate with an average power around 250 mW; the other part was conducted to drive the THz detector for THz pulse detection. The modulated photocurrent from the THz detector is then measured using a lock-in amplifier. It is noted that the THz detector has identical structure as THz emitter. The detected pulses are in time-domain and can be transformed into frequency domain information by performing Fourier transform, which shows a wide bandwidth range from 0.1 THz to around 2.0 THz for our system. Since the optical properties of VO₂ are temperature dependent, our samples were placed on a thermal stage with a hallow center for beam to pass. THz-TDS measurements were conducted at varied temperature with resolution of 0.1 K. For the raster-scanning measurements for VO₂ spatial modulators, a computer-controlled micro-position system was used to adjust the position of the devices, which will be discussed in details later.

Besides the transmission properties in THz range, the transmission in UV-VIS-NIR range was also investigated using a UV-VIS-NIR spectrophotometer (Shimadzu UV 3600). A home-made thermal stage was installed into this system to adjust sample temperature. The measurement range is between 190 nm to 3300 nm.

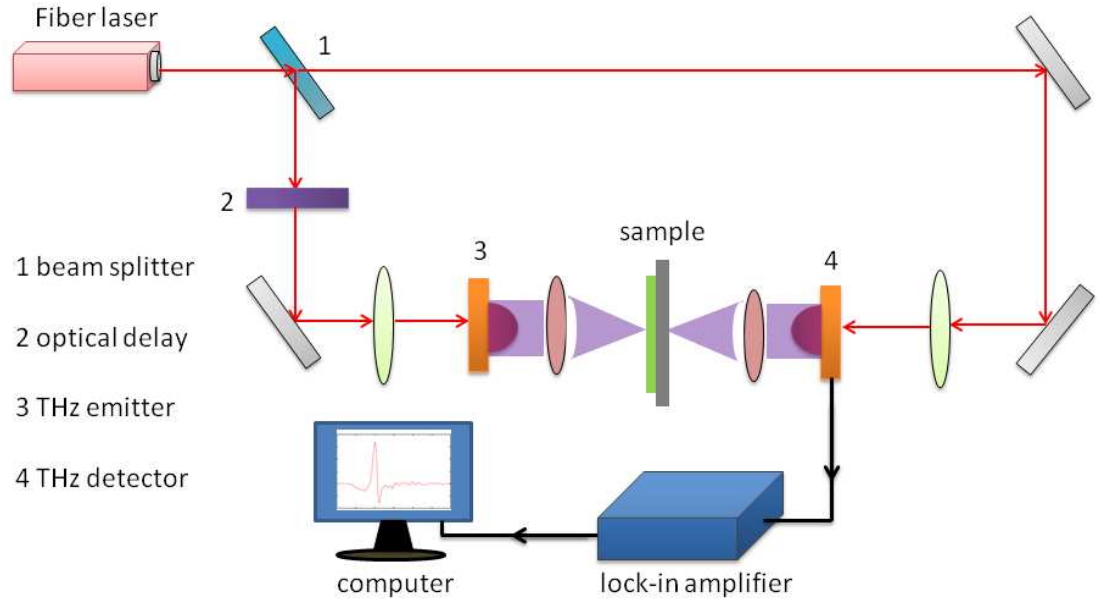


FIG. 2.6 Typical THZ-TDS schematic setups used for VO₂ thin films transmission measurement.

In addition to the aforementioned techniques and equipments, several other systems were also involved in this work, as summarized in the following list:

- 1) Transmission electron microscopy (TEM)
- 2) Scanning electron microscopy (SEM)
- 3) Dicing machine
- 4) Surface profiler (Deltak 3030)
- 5) O₂ plasma etching system
- 6) Wire-bonder (West Bond)
- 7) Temperature controller (Newport 350B)
- 8) Pulse generator (Hewllet Packard 8114A)
- 9) Oscilloscope (Tektronix TDS 2012)
- 10) Sourcemeter (Keithley 2400A)

Chapter 3

Structural and Electrical Properties of Polycrystalline VO₂ Thin Films Grown under Different Temperature

3.1 Abstract

We present the structural and electrical properties of (011) preferred polycrystalline (Poly-) VO₂ thin films grown at different temperature (T_S) with variable defects. These defects cause variation in strain, metal-insulator transition (MIT) critical temperature (T_C), activation energy (ΔE_a), and charge carrier type in insulating phase. The Poly-VO₂ behaves n-type conductivity when grown at relative low T_S. As T_S increases, defects related acceptor density increases to alter conductivity from n- to p-type in the Poly-VO₂. Moreover, the strain along monoclinic α_m axis dramatically reverses from tensile to compressive in the Poly-VO₂ (848 K < T_S < 873 K) and eventually approaches to a constant value in the Poly-VO₂ (T_S ≥ 898 K) in particular. T_{MIT} decreases with increasing the carrier density independent of the conductive type in the lightly doped Poly-VO₂. ΔE_a is associated with the carrier density and thus the strain or strained interfacial layer thickness in the Poly-VO₂. The larger tensile strain leads to lower carrier density and higher ΔE_a , while the constant strain produces saturated ΔE_a .

2.2 Introduction

Vanadium dioxide (VO₂) undergoes a first-order metal-insulator transition (MIT) from a high-temperature tetragonal (rutile) metal phase to a low-temperature monoclinic insulator phase at around 340K, and several interesting applications based on MIT of VO₂ thin films were proposed, as described in Chapter 1. It is well-known that vanadium oxides have a series of complex compounds, which complicates the

process to yield pure phase VO₂. To grow high quality and pure phase VO₂, the oxygen to argon (O₂ /Ar) flow ratio and the substrate temperature T_S should be precisely controlled.^{43, 44} The variation in growth conditions exerts obvious influence on films' MIT characteristics. The temperature coefficient of resistivity (TCR) in the insulator phase, transition critical temperature (T_C), and defect concentrations are some critical characteristics for applications. It has been reported that the TCR related activation energy (ΔE_a) and T_C , MIT parameters of VO₂ thin films could be modified by films quality,¹⁹ doping,^{20, 21} grain size / boundary,^{22, 23} lattice mismatch built-in strains,^{24, 25} etc. It is also reported that charge localization and surface segregation exhibits strong dependence on T_S during growth, inducing changes in V⁴⁺-V⁴⁺ pair distance and VO₂ band structure.¹⁶ Higher carrier density reduces the Thomas-Fermi screening length and lowers T_C, while shifts of the Fermi level (E_F) causes ΔE_a change. In addition, although both *p*- and *n*- type conductivity in the VO₂ were reported in the past, there are few reports discussing the mechanism leading to the different types of conductivity. In this part of work, a systematic study of T_S dependent defects influence on uniaxial strain, T_C and *M*-phase of polycrystalline VO₂ thin films will be discussed and the mechanism to produce *p*- or *n*-type conductive behavior in the VO₂ grown on coated Si substrate will be revealed..

3.3 Experiment

As aforementioned, vanadium oxides (VO_x) have a complex compound family, which makes it challenging to grow pure phase VO₂ out of VO_x. For reactive magnetron sputtering of VO₂ thin films growth, there are two critical operation parameters playing vital roles to affect the quality of as-grown thin films: the oxygen to argon flow ratio (O₂/Ar) and the growth temperature of the substrate (T_s). Besides these two factors, the choice of appropriate substrate also considerably affects the VO₂ crystal growth. An around 100 nm thick Si₃N₄ buffer layer was deposited onto Si (100) substrate for insulating purpose. Two control groups of samples were grown to figure

out the appropriate O₂/Ar ratio and T_S range for pure VO₂ yield. For the first group of growth, the substrate temperature was fixed at 550°C and the O₂/Ar ratios were adjusted to be 5%, 7%, 9%, 11%, 13% and 15% respectively, with a step of 2% for each growth. XRD was employed for material characterization. It is found that when the O₂/Ar ratio was set at 11%, the as-grown sample showed the purest VO₂ phase (see Figure 3.1). The other group of growth was conducted with O₂/Ar ratio fixed at 11%, but with substrate temperature varying from 773 K to 973 K to find out the best T_S. 50 nm Ti and 120 nm Au metal film stacks ohmic contacts were deposited onto the well-rinsed samples by standard photolithography, e-beam evaporation and lift-off procedures. MMR Hall system was employed to test the resistivity-temperature (R-T) curves and the transport parameters.

3.3 Results and Discussion

Figure 3.1 shows the measured XRD scan patterns for 6 samples from the first group. The incident angle was set at 0.5 degree ($\Omega=0.5^\circ$) to perform glancing scan. Pattern peaks from different VO_x compounds were indicated by different symbols. The as-grown VO_x phase changes obviously corresponding to the O₂/Ar ratio: i) when O₂/Ar ratio was 5% and 7%, the synthesized VO_x thin films were characterized to be mixtures of VO₂ and V₂O₃; ii) when the O₂/Ar ratio was increased to 9%, the mixture became VO₂ and V₅O₉; iii) when the ratio was 11%, all peaks from the XRD patterns were characterized to be from VO₂, indicating pure phase yield at this growth condition; iv) then when the ratio was further increased to 13% and 15%, only V₂O₅ phase peaks could be found from XRD scans. It is concluded that the optimum O₂/Ar ratio for VO₂ thin films growth is around 11%. The VO_x mixtures change trend is also in consistence with O₂ ratio increment, which suggests that more oxygen in the ambient will yield VO_x with larger vanadium valence potentials. The corresponding reference card for XRD patterns were: V₂O₃: JCPDS Card No.84-0318; VO₂: JCPDS Card No.72-0514; V₅O₉: JCPDS Card No.80-2027; V₂O₅: JCPDS Card No.85-2422.

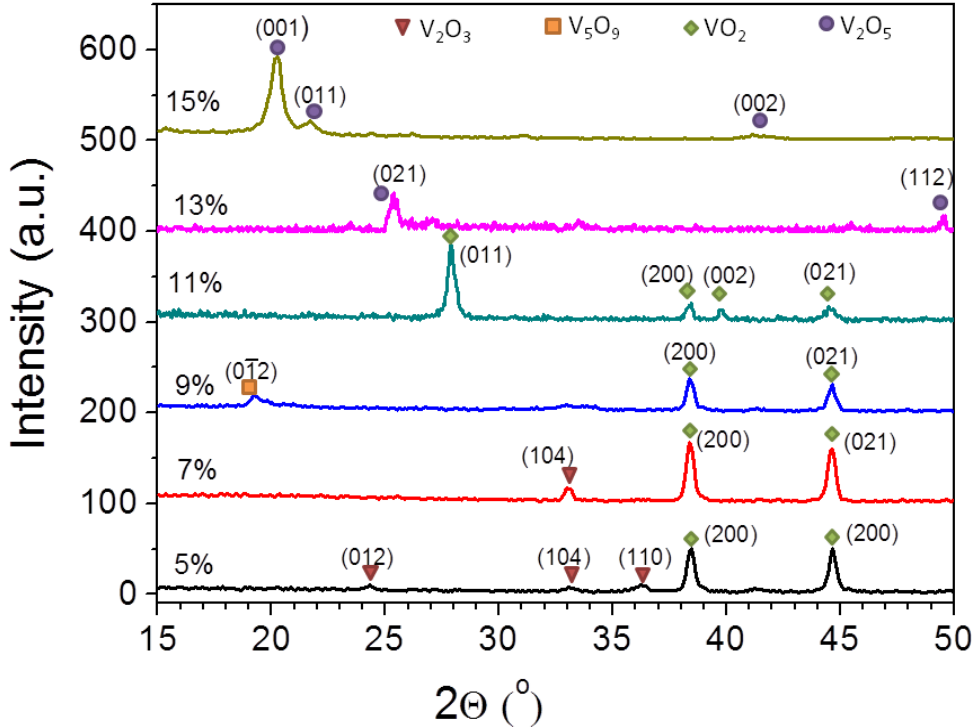


FIG. 3.1 XRD 2θ scan of VO_x thin films sample grown at different O₂/Ar ratio.

Figure 3.2(a) shows the XRD patterns of the sample grown at 575 °C with O₂ / Ar ratio set at 11%. 7 peaks located at 27.97°, 37.11°, 39.90°, 42.42°, 44.87°, 55.65°, 57.78° were respectively assigned to (011), (200), (002), (210), (021), (220), (022) patterns of monoclinic VO₂, with (011) being the dominating peak. According to the XRD patterns, VO₂ thin films grown on Si₃N₄/Si were characterized to be polycrystalline VO₂. The inset plot in Figure 3.2(a) shows the SEM image of the samples, and obvious and well-connected crystal structures could be observed. Figure 3.2(b) shows the resistance-temperature (R-T) hysteresis curves of the Poly-VO₂ sample. Generally, the R-T curves can be characterized by several specific factors, such as the resistance change ratio (ΔR) across the MIT, the critical transition temperature under temperature ramping-up (T_C), the hysteresis window (ΔH) and the transition slope. It is noteworthy that the insulating and metallic resistivity were also important factors that affect the optical properties of the sample, which will be further discussed later on. Sharp resistance change with obvious hysteresis curve was observed during

both the cooling and heating cycles. According to Figure 3.2(b), the ΔR is calculated to be around 200 folds, T_C is read to be around 344 K, and ΔH is found to be around 13 K. The ΔR in this sample is 2-3 orders of magnitude smaller than that of undoped VO_2 crystal, and the poly-crystalline nature of the sample is one of the main reasons, which introduced a lot of defects to reduce the low-temperature insulating resistivity and lift the high-temperature metallic resistivity and hence resulted in a small ΔR .

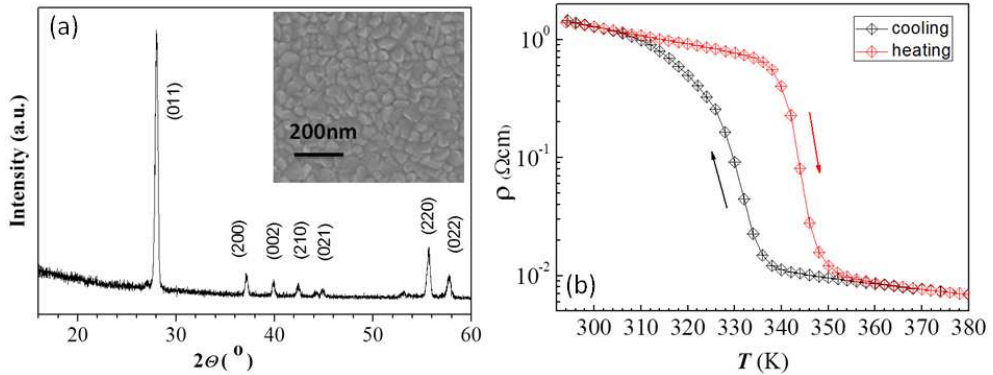


FIG. 3.2 (a) XRD 2θ glancing scan patterns for $\text{VO}_2/\text{Si}_3\text{N}_4/\text{Si}$ sample grown at 575°C. Inset plot is SEM image of the sample surface morphology. (b) R -T hysteresis curves acquired from Van der Pauw method.

The other group of samples was grown with the O_2/Ar ratio fixed at 11%, ambient pressure set at 3 mTorr but with varied T_S . It is found that pure VO_2 phase could be achieved in a wide temperature range from around 823 K to 923 K. However, T_S will affect the introduction of intrinsic defects, i.e., oxygen or vanadium vacancies into the films, and as a result, it will change the surface morphologies, crystal quality and finally the metal-insulator transition characteristics of the thin films. A set of 150 nm thick VO_2 samples were grown at T_S of 823 K, 848 K, 873 K, 898 K and 923 K, denoted as S1-S5 for convenience. All samples showed typical VO_2 XRD patterns, indicating pure phase polycrystalline VO_2 .

It was reported that there were two ways to introduce intrinsic defects into VO_2 films, either by V vacancy or O vacancy.¹⁶ The point defects of V vacancies in VO_2 introduce acceptors with localized holes, while O vacancies are donors with localized

electrons. Since subtle fluctuations in deposition may cause dynamic departure from the stoichiometry, O or V excess is proposed as the source of V or O vacancy defects. For O excess, V vacancies (V_V^4) are introduced to keep charge neutrality. Corresponding defect reaction: $O_2 \leftrightarrow V_V^4 + 4h^\bullet + 2O_O^\times$ is described in Kroger-Vink notation, where O_O^\times is O in the lattice. Holes (h^\bullet) will be trapped at nearest-neighbor V^{4+} sites to create V^{5+} ($3d^0$ in electron configuration) so that the V^{4+} - V^{4+} pairs become V^{5+} - V^{4+} pairs in analogy to Cr^{3+} substitution forming a Cr^{3+} - V^{5+} pair. V^{5+} introduces an acceptor level (E_A) in the gap at $\Delta E_A'$ (ionizing energy of acceptor) above the filled a_{1g} band. For V excess, the charge neutrality requires creation of O vacancies ($V_O^{\bullet\bullet}$) [$O_O^\times \leftrightarrow V_O^{\bullet\bullet} + 2e^\circ + 0.5O_2$], and electrostatic forces trap electrons (e°) at V^{4+} octahedral sites to create $V^{(4-n)+}$ - V^{4+} pairs (n=1, 2, or 3). In $3d^2$ or $3d^3$ configuration, the lower valence states of $V^{(4-n)+}$ introduce multiple donor levels (E_D) located at $\Delta E_D'$ (ionizing energy of donors) below the e_g^π band.

Figure 3.3 shows the R-T curves for S1-S5. In the low-temperature phase of VO_2 , the resistivity decreases with increasing T, and is found to change nearly 3 orders through the MIT in the Polycrystalline VO_2 . Derivatives of the resistivity variation curves {i.e., $d[-\log(\rho)/dT]$ } for heating cycle are shown in the inset plot. In the Poly- VO_2 , the extracted T_C results show a steady decrease for S1-S5: 349.4, 346.1, 341.8, 340.6, and 333.0 K, respectively, caused by an increase in T_S -dependent acceptor density in the Poly- VO_2 . As electron-correlation mechanism was suggested to be the driving force for metal-insulator transition in VO_2 , it is the strongly correlated nature of charge, spin, and lattice that causes the dependence of T_C on the doping. We can conclude that T_{MIT} has a decreasing trend as the carrier density increases regardless of its conductive type for the lightly doped Poly- VO_2 samples; however it exhibits strong dependence on the conductive type for the heavily doped samples. The high carrier density in S5 also reduces phase-transition sharpness.

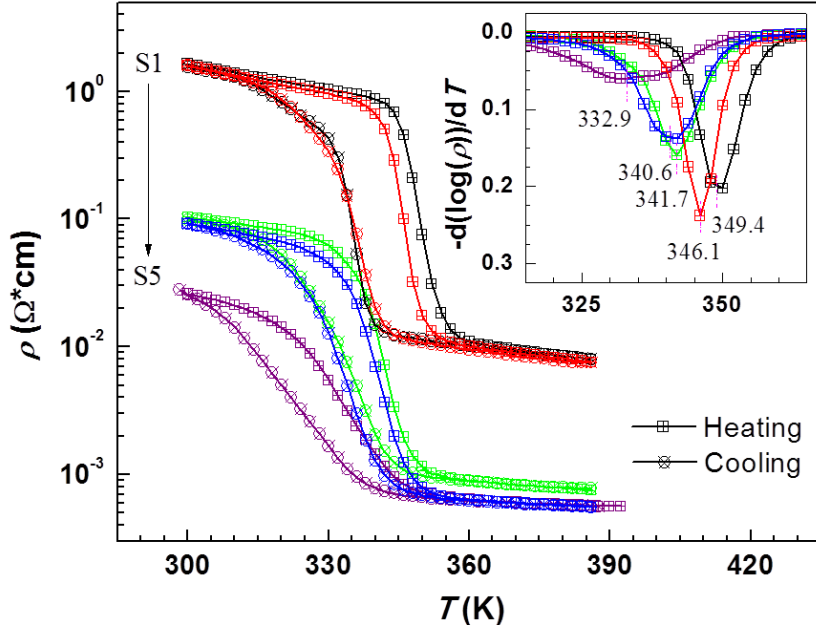


FIG. 3.3 R-T hysteresis curves for S1-S5 samples. The inset plot shows the differentials of $\log(\rho)$ during heating cycle.

The electrical transport information concerning these 5 samples was also investigated by conducting Hall measurement on the square samples designed for R-T curves testing. Room-temperature Hall effect measurements reveal different types of electrical conduction in the investigated samples. Samples grown at lower temperatures on $\text{Si}_3\text{N}_4/\text{Si}$ (S1 and S2) exhibit n-type conductivity, while samples (S3-S5) grown at higher temperature were confirmed to be p-type. The change in conducting type in Figure 3.4 (a) implies that both donors and acceptors are present in the samples studied here. As T_S increases, the increased V vacancies create holes to compensate donors introduced by O vacancies, and an excess of V vacancies changes the conduction from n-type to p-type in the Poly- VO_2 samples grown on the buffered silicon substrates.

In Mott insulators with intrinsic defects, electrical conduction may be described by a variable range hopping process and (or) thermally activated process. An Efros-Shklovskii variable range hopping mechanism is demonstrated to dominate low-temperature charge transport in amorphous vanadium oxide (VO_x); while in the poly - VO_2 , the thermally activated process exhibits the Arrhenius dependence, and the

resistivity of either the *n* - or *p*-type VO₂ can be expressed as:

$$\ln(\rho) = \ln(\rho_0) + \Delta E_a / kT \quad (5)$$

where $\rho_0 = \lim_{T \rightarrow \infty}(\rho)$. Figures 7(b) show that $\ln(\rho)$ varies linearly with $1/kT$ when VO₂ is in the low-temperature phase. From the Arrhenius plot in Figure 3.4 (b), ΔE_a was calculated to be 80.4, 73.8, 41.9, 49.9, and 43.3 meV for S1-S5. The temperature coefficient of resistivity, defined as $TCR = (1/\rho)(d\rho/dT)$, varies linearly with ΔE_a according to $\Delta E_a = -kT^2 \times TCR$, and the values of TCR, in %K, are -1.04, -0.95, -0.54, -0.65, and -0.56 for S1-S5 at T=300K.

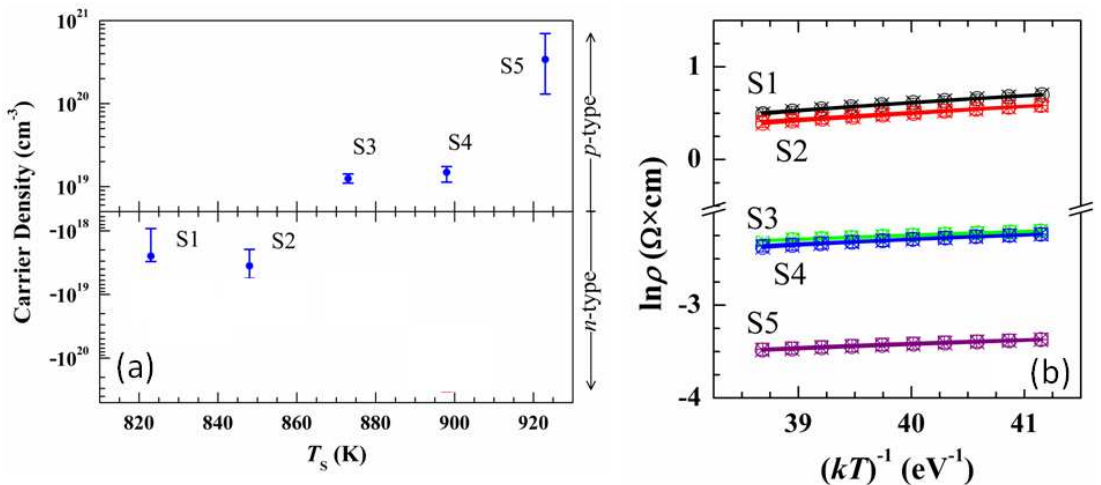


FIG. 3.4 (a) Average carrier density and carrier type for S1-S5 samples at room temperature and (b) $\ln(\rho)$ vs $(kT)^{-1}$ plots for S1-S5 samples in low-temperature at $282\text{K} \leq T \leq 300\text{K}$.

XRD glancing scan were also conducted on all 5 samples and all scans (not shown here) displayed similar XRD patterns as shown in Figure 3.5(a), with (011) peak located at 27.9 ° being the dominant peak and no other impure phase was found. As shown in Fig. 3.5(a), the (011) diffraction peak from S1-S5 shifts to higher 2θ angle with the exception of S4 as compared to the identical unoriented powder, indicating an enhanced out-of-plane compressive strain with T_s , and the strain changes from -0.467% (S1) to -0.557% (S5). In the case of V-O bond length being shortened, two apical O²⁻ of

the octahedron move closer with a decrease in (011) lattice plane spacing. Deducing from the data of x-ray photoelectron spectroscopy¹⁶ and Hall-effect experiments, we consider that as T_S increases, O vacancy density remains essentially constant at lower T_S , while V vacancies significantly increase for $T_S \geq 873$ K. This reduces the O²⁻-O²⁻ apical distance in the octahedron, leading to an increased uniaxial compressive strain along [011]. Measured (200) lattice-plane spacing are $d_{(200)}=2.421$ Å (S1), 2.419 Å (S2), 2.416 Å (S3), 2.418 Å (S4), and 2.418 Å (S5). Invariable β angle with impurity was demonstrated for the powder of *M*-phase $V_xW_{1-x}O_2$ ($x > 0.98$);⁶² under the assumption of fixed β angle for the Poly-VO₂ with the preferred (011) nearly parallel to the substrate surface, we obtain $a=5.748$ Å, 5.744 Å, 5.736 Å, 5.741 Å, and 5.741 Å for S1-S5, correlated with V⁴⁺-V⁴⁺ pair distance.

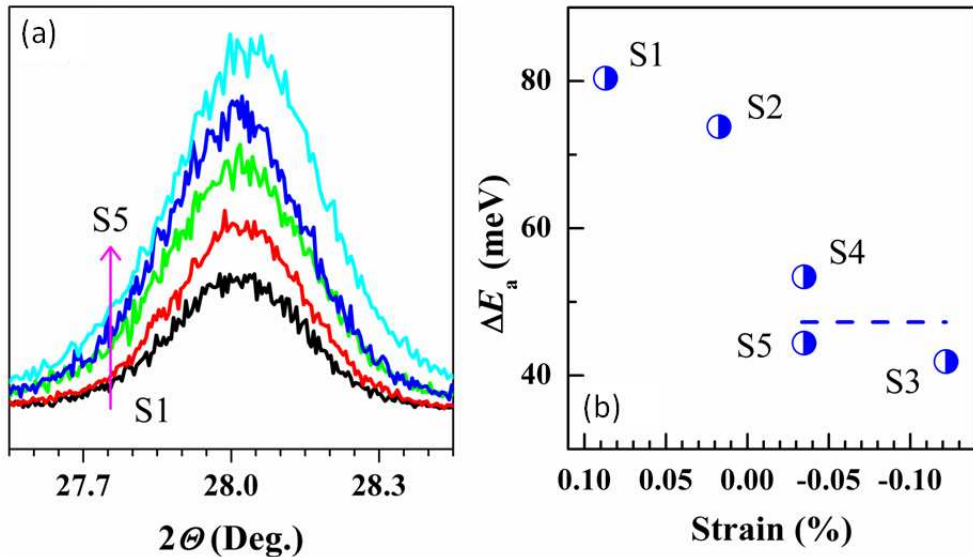


FIG. 3.5 (a) Single Peak 2θ scan of the (011) peak, and (b) ΔE_a dependence of strain along the am axis in S1-S5 samples.

For the Poly-VO₂, the strain along the a_m axis is tensile in S1 and S2 whereas compressive in S3, and finally tends to constant when further increasing T_S , as shown in Figure 3.5 (b). It is concluded that the larger tensile strain along a_m axis leads to lower density of intrinsic dopants but higher ΔE_a , while the constant compressive

strain produces the saturated ΔE_a in the Poly-VO₂ grown at $T_S \geq 898$ K; in addition, TCR has the same variation trend as ΔE_a .

2.4 Summary

In summary, this part of work reveals remarkable impacts of growth temperature and defects on the structural and MIT properties of intrinsic VO₂ polycrystalline thin films, in a view of changes in the strain along the a_m axis, conductive behaviors, transition temperature, and *M*-phase ΔE_a (or the related TCR).

The VO₂ samples have (011) preferred polycrystalline structure when grown on Si₃N₄/Si substrate. As T_S increases, defect related acceptor density increases to alter conductivity from n- to p-type in the Poly-VO₂. Moreover, the strain along monoclinic a_m axis dramatically reverses from tensile to compressive in the poly-VO₂ (848 K < T_S < 873 K), and eventually approaches to constant with phase segregation in the Poly-VO₂ ($T_S \geq 898$ K) in particular. As a consequence, T_C decreases with increasing the carrier density independent of the conductive type for the poly-VO₂. ΔE_a of the *M*-phase is associated with the carrier density and hence the strain in the poly-VO₂. The larger tensile strain leads to lower carrier density but higher ΔE_a , while the constant compressive strain produces saturated or the minimum ΔE_a . These observations and interpretations related with the intrinsic VO₂ growth will be helpful for developing VO₂ based materials for applications in sensing, switching, and modulation through structure modifications by different methods.

Chapter 4

Structural, Electrical and Optical Properties of VO₂ Grown on c-cut Sapphire

4.1 Introduction

Recently considerable efforts have been focused on developing terahertz (THz) wave switches,⁶³ filters,⁶⁴ and modulators for imaging,⁶⁵ spectroscopy,⁶⁶ and wireless communication applications.⁶⁷ However, the progress in this field is strongly limited by the modulation depth, with the state-of-the-art meta-material based THz switches and modulators having a modulation depth of 50%.⁶⁸ Other materials and approaches to realize THz switches and modulators with larger modulation depths are in great need. Previous study reported that insulating VO₂ is highly transparent for wavelength above 45 μm (i.e., below 6.7 THz), with very low loss mainly caused by low-density free carrier absorption. Since metallic VO₂ has a high free carrier concentration in the order of 10²¹ cm⁻³ with large absorption, VO₂ could be an ideal candidate for THz wave modulation. To achieve a large modulation depth, it is critical that VO₂ thin film has a large resistivity variation in the phase transition, which requires a high crystalline quality. Hence growing epitaxial structure of VO₂ is of great interest. Sapphire was selected as substrate because VO₂ can be epitaxially grown on it with relatively high crystalline quality. Also, sapphire is almost transparent at THz frequencies.

120 nm thick VO₂ thin films were grown on c-cut (0001) sapphire substrates using pulsed reactive magnetron sputtering system, with 99.9% vanadium as the target in 3 mTorr O₂/Ar gas environment (11% O₂ flow ratio). The substrate heater temperature was maintained at 575 °C. The film structure was characterized by x-ray diffractometry (XRD) and transmission electron microscopy (TEM), and R-T hysteresis curves were measured using the Van der Pauw method.

Temperature-dependent THz transmission measurements were performed using a time-domain THz spectrometer with VO₂ samples sitting on a thermo-electric heater/cooler sample stage. All THz transmission measurements were performed at normal incidence in the 0.1-2.0 THz range. Although the VO₂ films were deposited at high growth temperatures, corresponding to a metallic phase with rutile (*R*) crystal structure, the structural characterizations reported here were performed at room temperature, which corresponds to the insulating phase with a monoclinic (*M*) structure.

4.2 XRD characterization and structural analysis

4.2.1 XRD θ-2θ scan (in-axis scan)

Figure 4.1 shows the XRD pattern in θ-2θ scan. In addition to the (0006) and (00012) diffraction peaks from the sapphire substrate, two VO₂ peaks located at 39.83° and 85.85° were observed. As pointed out by Gupta et al.,⁶⁹ these two peaks can either correspond to the (002) and (004) or to the (020) and (040) diffractions. Off-axis Φ scans were performed in order to elucidate the azimuthal orientation of VO₂ films.

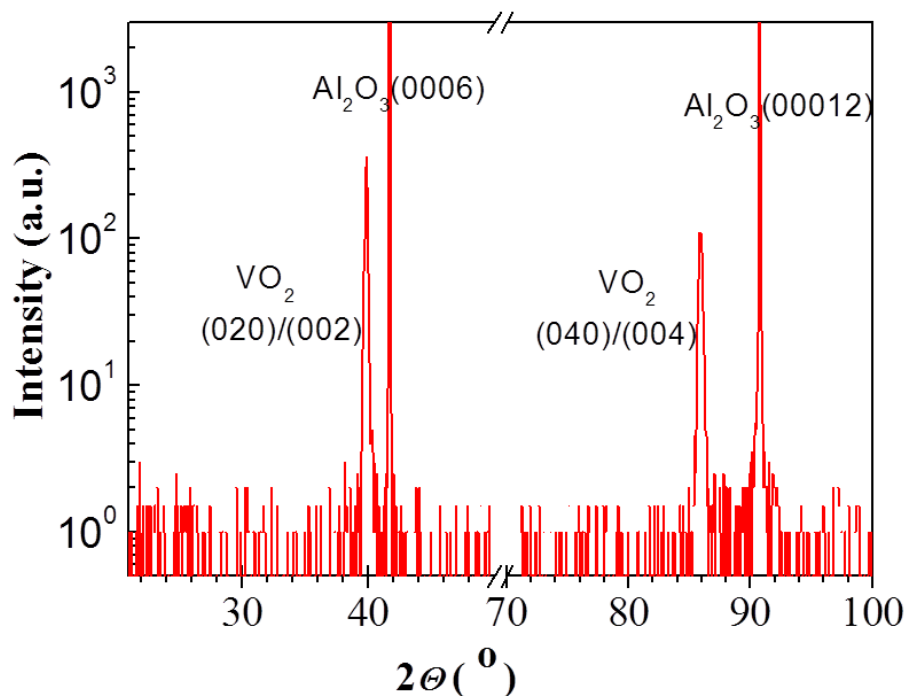


FIG. 4.1 XRD θ - 2θ scan patterns of as-grown VO₂ epitaxial films on c-cut sapphire substrate.

4.2.2 XRD off-axis scan

As stated above, it is hard to determine the actual growth direction for the epitaxial layers simply by conducting Ω - 2θ scan, because peak positions of M-VO₂ (020) and (002) peaks are very close to each other. The off-axis Φ scans (also known as azimuthal scan) were conducted to figure out azimuthal orientation of the growth orientation of VO₂ films on c-cut sapphire. We conducted off scan of both the (011) and (220) peaks to figure out the structural information of VO₂ thin films. The detailed procedures of off-axis Φ scan of VO₂ (011) are described as follow:

- (1) The (020)/(002) peaks were located and the Ω_0 was optimized and determined to be 19.93°.
- (2) Then according to standard reference card, 2θ angle of VO₂ (011) is find to be $2\theta_{(011)} = 27.878^\circ$; and the detector was then set at 27.878°;
- (3) Then the angle between VO₂ (011) / (020) plane ($\Delta\Psi$) was calculated using the following equation:

$$\cos(\Delta\Psi) = \frac{d_1 d_2}{\sin^2 \beta} \left[\frac{h_1 h_2}{a^2} + \frac{k_1 k_2 \sin^2 \beta}{b^2} + \frac{l_1 l_2}{c^2} - \frac{(l_1 h_2 + l_2 h_1) \cos \beta}{ac} \right] \quad (6)$$

In which $(h_1 k_1 l_1) = (011)$ and $(h_2 k_2 l_2) = (020)$, d_1 and d_2 is the plane distance for (011) and (020) planes and could be calculated by $d = \lambda / 2 \sin \theta$, and $\beta = 122.61^\circ$, $a = 5.743$, $b = 4.517$, $c = 5.375$, which is acquired from the standard card: JCPDS Card. No. 72-0514. The $\Delta\Psi_{(020)/(011)}$ is then calculated to be 44.7°, and then the Ψ angle of the XRD system was changed to be 44.7°.

The Φ scan was then conducted from 0 to 360° with a step of 1°. The measured scan peaks were plotted in Figure 4.2(a). Following the same procedure, we also trying to get the Φ scan of (102) peak based on the assumption that the growth orientation is (002), hence the $(h_1 k_1 l_1) = (102)$, and $(h_2 k_2 l_2) = (002)$. For this scan, the 2θ was set at 51.105° and the $\Delta\Psi_{(002)/(102)}$ was calculated and set to be 17.61°. However, this Φ scan

with these setting come out of no peaks. Combing with the off-axis Φ scan patterns based on (020) orientation, the possibility of (002) grown orientation was excluded, therefore the growth direction was demined as (020). Figure 4.2(a) is from the off-axis Φ scan of (011) plane, which shows a six-fold symmetry but with twin peaks at each 60° position. The off-axis scan of $\text{Al}_2\text{O}_3(1\bar{1}02)$ peak was also conducted and plotted in figure 4.2(a), which shows a three-fold symmetry with single peak separated by 120° . It is also noted that the peak from the sapphire is in the middle of two neighboring peaks from VO_2 . To calculate the actual structural parameters of the VO_2 unit cell, another off-axis scan of $\text{VO}_2(220)$ peaks were measured ($2\theta = 55.645^\circ$, $\Delta\Psi = 42.76^\circ$), which also displayed six-fold symmetric peaks, but with each peak consisting of 3 peaks, as shown in Figure 4.2(b). The peak-to-peak value of $\text{VO}_2(011)$ plane is denoted as $2\Delta\beta$ and the peak-to-peak value for $\text{VO}_2(220)$ is denoted as δ_1 and δ_2 , respectively. The origination of these multiple peaks is related with the actual structure of the unit cell and a tentative explanation will be offered in the following paragraph.

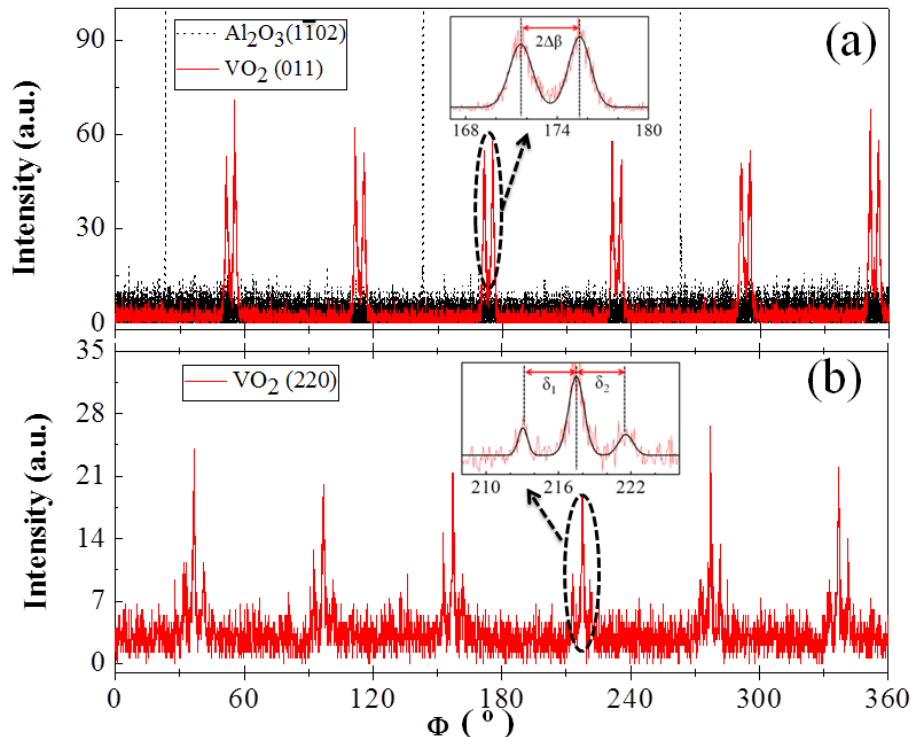


FIG. 4.2 (a) Off-axis $\text{VO}_2(011)$ plane Φ scan and $\text{Al}_2\text{O}_3(1\bar{1}02)$ plane, and (b)

off-axis VO_2 (220) plane.

4.2.3 Explanation for off-axis Φ scan results

Sixfold symmetry of the (011) peaks observed in Figure 4.2(a) is attributed to its triple-domain structure that is invariant to 60° rotation in the (020) basal plane, and (011) peaks appear in pairs because the angle β of VO_2 deviates from the 120° angle of the sapphire hexagon. These can be understood based on the schematics shown in Figure 4.3. In the initial stage of the epitaxial growth, V ions form bonds with substrate surface O ions and stack on a triangle of the O ions to minimize the electrostatic potential, as illustrated in Figure 4.3(a). In the next stage, O^{2-} and constructed octahedra VO_6 in sequences are grown to form VO_2 cells with the monoclinic b_m axis perpendicular to the substrate surface. As illustrated in Figure 4.3(b), the hexagonal symmetry of c- Al_2O_3 leads to three equally probable arrangements of VO_2 with 60° rotation relative to each other to form a multi-domain structure, leading to a 60° symmetry of the (011) scan. Since the angle β of VO_2 bulk is 122.61° , deviating from the 120° angle of the Al_2O_3 hexagon, V⁴⁺ ions at the interface are not positioned strictly right above the center of O²⁻ ions triangle. It is already illustrated in Figure 1.1 that the vanadium atom pairs form a zig-zag chain in monoclinic phase. The paired V⁴⁺-V⁴⁺ chain forms angle δ_1 with a_m axis and the unpaired neighboring V⁴⁺-V⁴⁺ gives angle δ_2 . Based on the relative angle of the three peaks at each 60° symmetric position in Figure 4.2(b), and average values $\delta_1 = 4.40^\circ$ and $\delta_2 = 4.29$ were determined. Separation of the twin peaks in the (011) Φ scan corresponds to twice the angle mismatch ($\Delta\beta$), and $2\Delta\beta$ is measured to be 4.32° from Figure 4.2(a), which determined an average value of 122.16° for β .

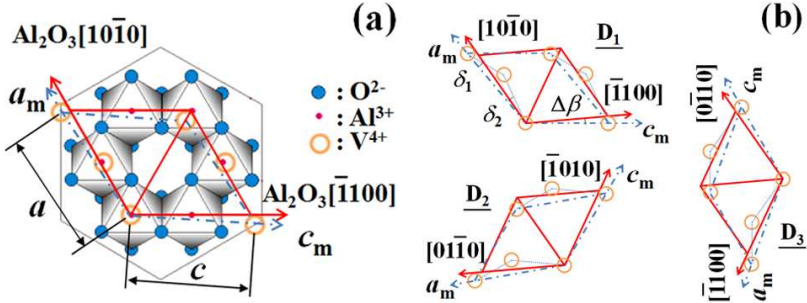


FIG. 4.3 (a) The schematic configuration of atoms at the interface between the VO₂ thin films and the sapphire substrate. (b) 3 possible arrangements of VO₂ domains, D1-D3.

Figure 4.4 shows the schematic origination of the sixfold double-peaks acquired from the off-axis scan of VO₂ (011) planes, and origination of three peaks from Φ scan of Al₂O₃ (1102) plane. It is already known that the β angle of the VO₂ unit cell is around 122°, which is ~2° mismatch with the sapphire hexagonal angle of 120°, hence the a_m and c_m of the unit cells is deviated from the ideal boundary as indicated by the black dash lines. As a result, those 3 VO₂ unit cells have to share the boundary area and form twining structure. For the off-axis Φ scan of (011) plane, six-fold peaks could be demonstrated, which came from two sets of reflection, (011) and (011̄), with each sets having 3 symmetric peaks. Each peak consists of two reflection patterns: one is from the atoms along a_m axis and the other one from atoms along c_m axis. The Φ scan of sapphire (1102) was also included in Figure 4.4, which shows that the peaks were actually from three symmetric planes, and each peaks was located in the middle of two consecutive peaks from off-axis Φ scan of (011) plane, which is consistent with the XRD measurements shown in Figure 4.2(a).

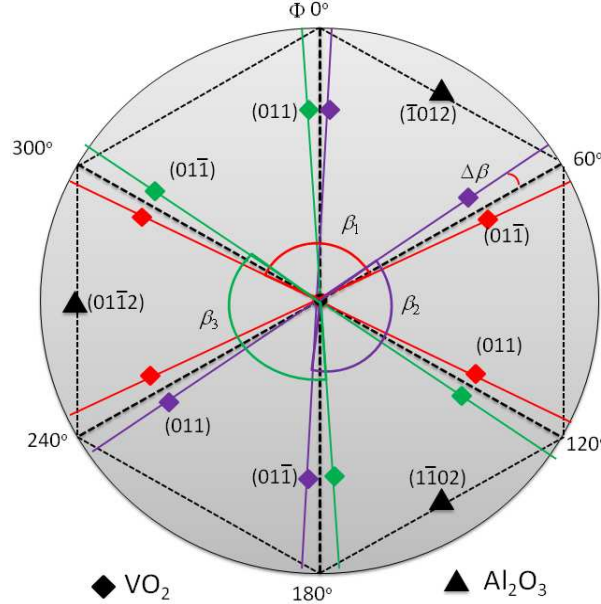


FIG. 4.4 Schematic diagram for the origination of sixfold and twin-peak for VO_2 (011) planes and 3 peaks for Al_2O_3 (1̄102) plane during off-axis Φ scan.

In combination with the off-axis scans for the VO_2 (011) and (220) planes, the film lattice parameters were calculated as: $a=5.751 \text{ \AA}$, $b=4.522 \text{ \AA}$, $c=5.360 \text{ \AA}$, and $\theta=122.16^\circ$; moreover, the bonded $\text{V}^{4+}-\text{V}^{4+}$ pairs were separated by 2.847 \AA along a zigzag chain. The lattice mismatch between VO_2 and the underlying sapphire substrate introduces strains in the epitaxial thin-films, while this strain can be partially released through vacancies generation, especially in the film close to the interface.

4.3 SEM and TEM analysis

Figure 4.5(a) shows the high-resolution TEM image, which exhibits clear films / substrate interface, demonstrating the good epitaxial quality of the films. A higher density of defects, related with V^{4+} and O^{2-} vacancies and other structural defects, are observed close to the interface between the VO_2 and the substrate; however, the defect density decreases with the film thickness, and the VO_2 lattice fringes becomes much more defined for regions of film close to the top surface. The inset plot shows the image of VO_2 grains, which displays very good crystal grains with size up to 200 nm, which is

much larger than grain size of polycrystalline VO₂ deposited on Si₃N₄ coated Si substrate. The SAED pattern from Figure 4.5(b) is consistent with the results obtained from the previous XRD measurements. The growth direction of VO₂ is confirmed to be (010), and the complete epitaxial relationship between the VO₂ thin films and the c-plane sapphire can be concluded as VO₂ [010] // Al₂O₃ [0001] and VO₂ (-202) // Al₂O₃ (11-20).

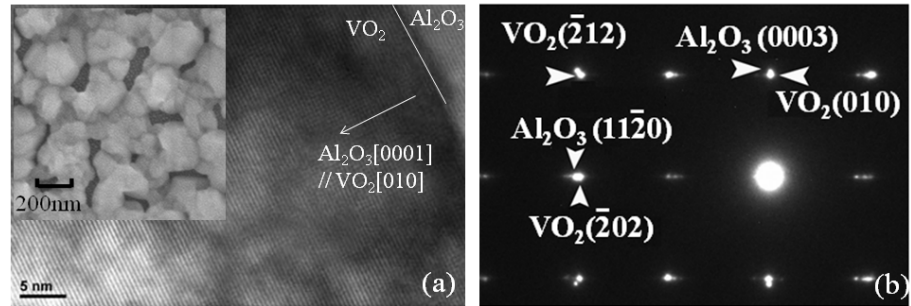


FIG. 4.5 (a) High resolution TEM image of the film-substrate interface area. Inset shows the SEM image of the VO₂ films surface morphology. (b) SAED pattern along the sapphire [10\bar{1}0] zone axis.

4.4 Electrical properties

Figure 4.6 shows the R-T curves of VO₂ thin films grown on c-plane sapphire. The resistivity has over 4 orders of magnitude change (ΔR) during the metal-insulator transition, changing from around 20 Ωcm to $3.6 \times 10^{-4} \Omega\text{cm}$. The much larger ΔR indicates better quality of these thin films deposited on c-cut sapphire, as compared to the films deposited on Si based substrate under the same growth condition (as shown in Figure 3.2). The phase transition temperature T_C is determined to be 344 K during the heating process and 338 K for temperature ramping down, accounting for a transition hysteresis window $\Delta H \approx 6\text{K}$. The good MIT characteristics, unveiled by R-T curves, suggested good quality of VO₂ hetero-epitaxial growth on c-cut sapphire, making it desirable for optical modulation applications.

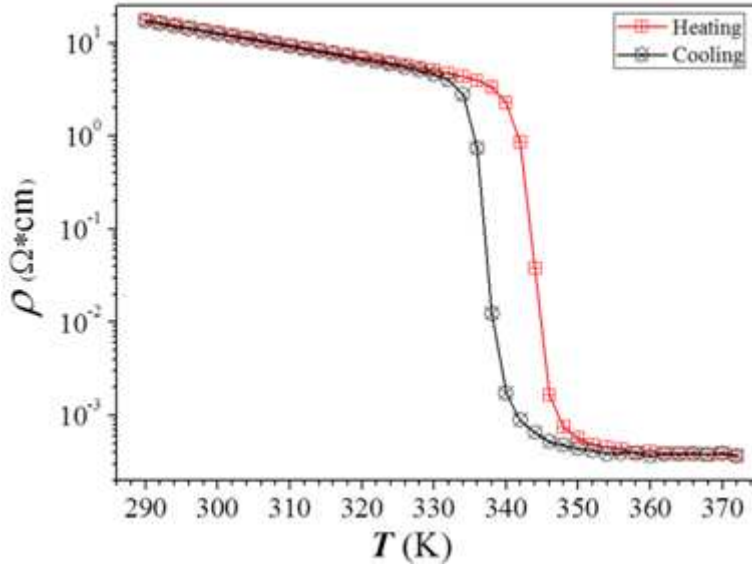


FIG. 4.6 R - T curves of VO_2 thin films grown on c-plane measured during heating and cooling process.

4.5 Optical properties

It is well-known that VO_2 shows dramatic optical properties change across its metal-insulator transition, especially in the Infrared and Terahertz range, hence terahertz time-domain spectroscopy (THz-TDS) were conducted at temperature above T_C (80 °C or 353 K) and far below T_C (25 °C or 298 K) respectively to check the modulation performance of the as-grown c-cut samples. The details of the THz-TDS have already described in the introduction section, and the thin films sample was put on a thermal-resistor. Thermal paste was used to achieve good thermal conduction. Figure 4.7(a) shows the typical transmission pulses from the THz-TDS system. It is obvious that more than 4 times change in the amplitude of the pulse peaks could be observed, indicating very good transmission modulation performance of VO_2 thin films across the MIT. It is noted that there is a phase reversal for the second peak, as indicated by the black arrow, which is reflected pulses from the thin films. The π phase change suggested that at 80 °C, the VO_2 had fully transited into metallic phase. The reversal of peak can serve as the fingerprint of the MIT during THz-TDS measurements. Figure 4.7(b) was obtained by Fourier transformation of the dominant peak in the time-domain

response , which shows uniform modulation across 0.1-2.0 THz range.

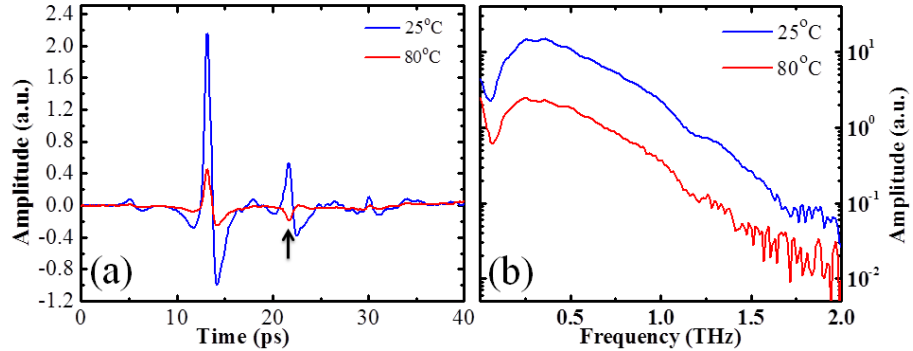


FIG. 4.7 (a) Time-domain and (b) frequency-domain THz transmission of VO₂ thin films on c-cut sapphire.

To further obtain the detailed modulation performance of VO₂ thin films across MIT, we conducted series of scans at different temperatures during cooling and heating process. The measured amplitude of the dominant peak is plotted vs temperature in Figure 4.8. Combing Figure 4.6 and 4.8, it is found that the THz transmission shows a positive relationship with the electrical conductivity of metallic state. The Drude model was proposed to quantatively analyze the conductivity influence on the modulation depth, i.e., on the transmission of metallic state VO₂ thin films. The transmission through metallic films can be calculated by equation:^{30, 70}

$$\frac{\tilde{E}_{f+s}(\omega)}{\tilde{E}_s(\omega)} = \frac{1 + n_s}{1 + n_s + Z_0 \tilde{\sigma}(\omega) t_f} \quad (7)$$

Where ω is the angular frequency, $Z_0 = 377 \Omega$ is the vacuum impedance, $t = 120$ nm is the film thickness and $\tilde{\sigma}(\omega)$ is the complex conductivity of the VO₂ films. The complex conductivity of the films can be approximated by their DC conductivity since the imaginary part value is negligible compared to that of real part. Substitute data in Figure 4.6 into Equation (7), the simulated THz transmission can be acquired. Since complex conductivity and complex dielectric constant is related through following equation:

$$\tilde{\sigma}(\omega) = \sigma_1 + i\sigma_2 = -i\epsilon_o\omega[\tilde{\epsilon}(\omega) - 1] \quad (8)$$

hence the complex dielectric constant can be calculated as:

$$\tilde{\epsilon}(\omega) = [n(\omega) + ik(\omega)]^2 = 1 + i \frac{\tilde{\sigma}(\omega)}{\omega\epsilon_o} \quad (9)$$

From Equation (9), the refractive index $n(\omega)$ and extinction factor $k(\omega)$ can also be acquired based on transmission data.

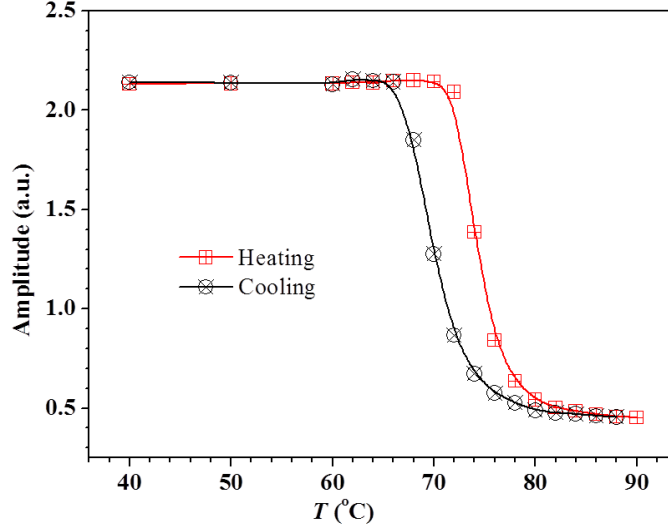


FIG. 4.8 Measured THz field amplitude transmission vs temperature for VO₂ thin films grown on c-cut sapphire. The solid curves are simulated transmission.

The THz transmission of VO₂ thin films across MIT could also be interpreted by Maxwell-Garnett effective medium theory (MG-EMT),⁷¹ according to which the metal-insulator transition in VO₂ thin films is suggested to be a percolation process. When the sample is heated up close to T_C, metallic puddles firstly form and expand themselves, and finally connect with each other to form continuous metallic phase.⁷². The fraction of metallic phase in VO₂ is given by

$$f(T) = f_{\max} \left(1 - \frac{1}{1 + \exp[(T - T_C)/\Delta H]} \right) \quad (10)$$

Where T_C is the critical temperature, and ΔH is the transition window, all of which could be determined from resistivity-temperature (R-T) curves from Figure 4.6. According to the MG-EMT theory, the effective complex dielectric is determined by

the following equation:⁷³

$$\epsilon_{eff}(T) = \epsilon_i \times \frac{\epsilon_m[1+2f(T)] - \epsilon_i[2f(T)-2]}{\epsilon_i[2+f(T)] + \epsilon_m[1-f(T)]} \quad (10)$$

4.6 Summary

In summary, by conducting XRD in- and off- axis scans, VO₂ thin-films grown on c-sapphire substrate were confirmed to be triple-domain hetero-epitaxial structured, with an epitaxial relationship of VO₂ (010) // Al₂O₃(0001) and VO₂ [2̄02] // Al₂O₃ [11̄20]. The triple-domain structure is caused by the crystal structure difference between monoclinic VO₂ and hexagonal sapphire. As revealed by time-domain terahertz spectroscopy measurements, THz pulses demonstrate fourfold amplitude change through VO₂ thin films during the metal-insulator transition. Uniform modulation performance was achieved in wide bandwidth ranging from 0.1-2.0 THz, indicating strong potentials of VO₂ for terahertz wave switching and modulation applications.

Chapter 5

Electric Voltage Triggered MIT in VO₂ Two-Terminal Devices

This part of work mainly discussed the MIT response of VO₂ thin films based two-terminal devices under electric sources stimulation, namely, voltage sweeping and voltage pulses. Since electric source is one of the most convenient approaches to trigger MIT, it is of great interest to investigate the transition process and characteristics under varied electric sources, which will benefit applications based on electrically controlled MIT in VO₂ thin films.

5.1 MIT under voltage sweeping

5.1.1 Introduction

Metal-insulator transition in VO₂ thin films is a promising approach for optical and electrical switching applications, therefore investigate its mechanism, especially under electric stimuli,⁷⁴⁻⁷⁶ is of great interest, which provides the possibility for high-speed and convenient operations, as compared to optical,⁷⁷ strain/stress induced MIT⁷⁸. In this section, electric voltage (field) induced MIT in VO₂ two-terminal devices will be investigated. A series of two-terminal devices with different gap dimensions were fabricated on VO₂ thin films grown on c-cut sapphire by standard photolithography and deposition process. Ti/Au stacks were deposited to serve as ohmic contacts. In this work, both sweeping voltage and voltage pulses were applied to these two-terminal devices to investigate their transition characteristics.

5.1.2 Device size effects on MIT of VO₂ two terminal devices.

Gap width of the first group of two terminal devices is fixed at 120 μm and the gap length varied from 10 to 30 μm. A sweeping voltage with step of 0.1 volt was

applied to the contacts by sourcemeter, and the measured voltage-current (V-I) curves were plotted in Figure 5.1(a). All measurements were conducted at room temperature. It is obvious that for each scan, a sharp current jump occurred when the sweeping voltage reached certain critical value (V_C). This sudden current jump originated from dramatic drop in the device resistance, mainly from VO_2 thin films channel, indicating that occurrence of MIT in device. It is also noted that for larger gap length, a relatively larger V_C is necessitated to trigger the transition, moreover, as denoted by the red-dash line, all current started to jumped at a almost constant current value (I_C).

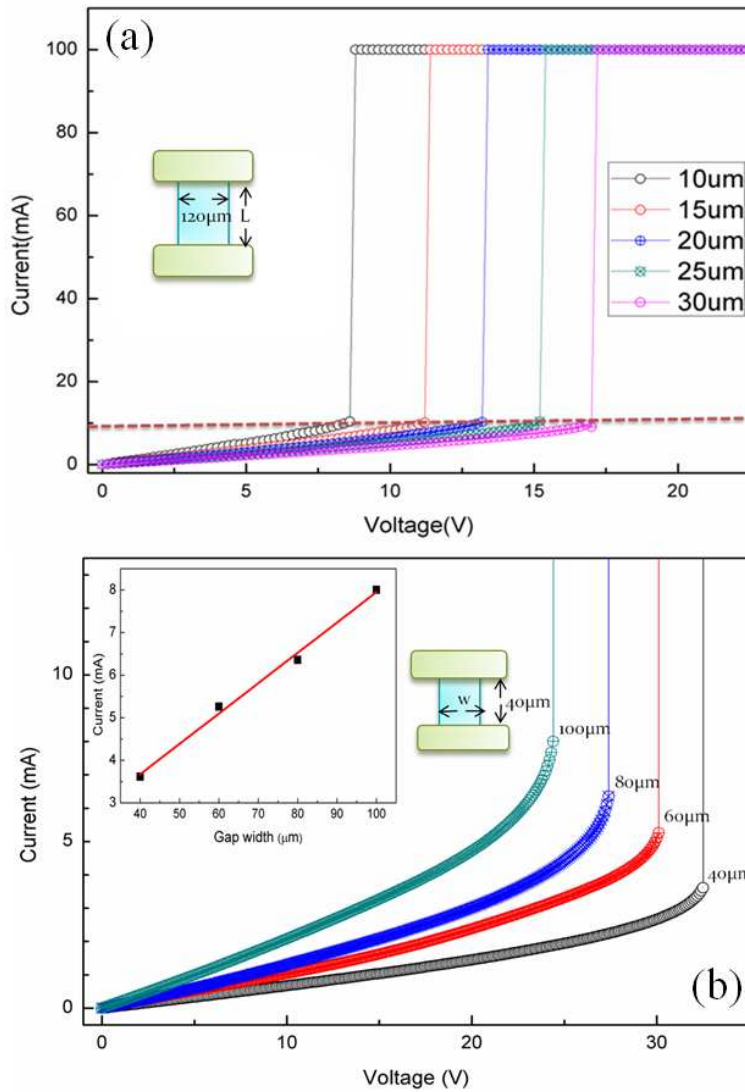


FIG. 5.1 V-I characteristics of VO_2 thin films based two-terminal devices: (a) device group with fixed gap width but varied gap length and (b) device group with fixed gap length but varied gap width.

Figure 5.1(b) shows the V-I curves for the other group of VO_2 two-terminal devices, which have fixed gap length of 40 μm but varied gap width, designed to be 40 μm , 60 μm , 80 μm and 100 μm , respectively. Again sudden current jump occurred for each sweeping process, but the critical current value varied from each other. The inset plot of Figure 5.1(b) shows the critical current I_C vs device gap width w , which shows a clearly linear relationship, implying that a constant current density (J_C) around $6 \times 10^4 \text{ A/cm}^2$ when transition occurred.

5.1.2 Temperature effects on MIT in VO_2 two terminal devices.

Since thermal effects play a vital role in MIT of VO_2 , and the fact that the joule heat generated by applied electric source could not be excluded, we conducted another group of measurements to investigate the ambient temperature affects on electric voltage induced transition in a VO_2 two terminal devices. A device with 120 nm in gap width and 20 μm in gap length was placed on a thermal-resistor. The measured data were plotted in Figure 5.2.

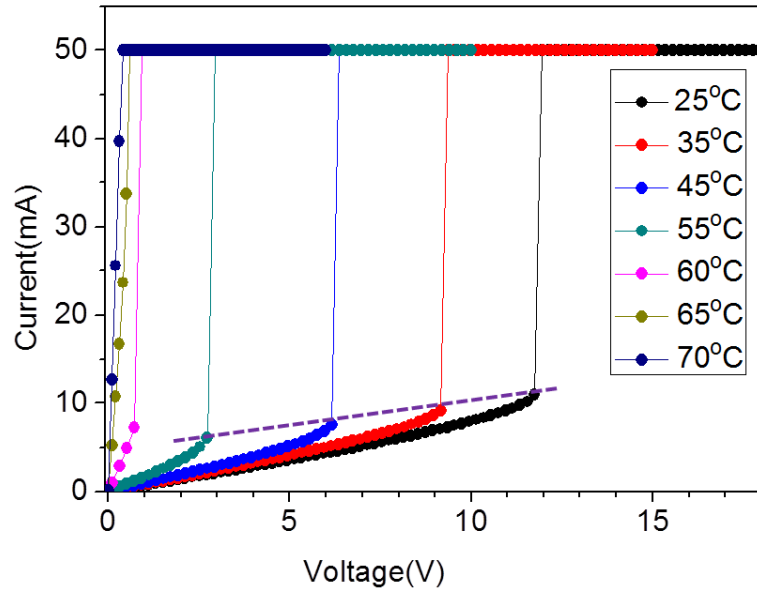


FIG. 5.2 V-I characteristics of VO_2 two-terminal devices at different temperature.

Obviously, when the temperature was increased, the MIT occurred at smaller voltage, meanwhile, the critical current also seriously decreased. Interestingly, when

the temperature was not closed to transition temperature, a linear relationship could be found between the transition voltage and current. However, it is impossible to determine whether the electric factor or the thermal heat triggered the transition, but it unveiled that a much smaller voltage/current can trigger MIT in heated VO₂ devices, which is helpful for practical application based on MIT in VO₂ thin films.

5.2 MIT under voltage pulse stimulation

5.2.1 Introduction

For electrically controlled electrical and / or optical switching applications, switching speed is one of the key parameters that determine device's potentials and practical operation method. Cavalleri et al⁵⁵ reported a sub-picosecond transition time when VO₂ thin films was stimulated by optical excitation, and Stefanovich et al⁷⁴ reported a transition time in nanosecond scale when triggered by electric voltage pulses. However, the parameters of pulses and the ambient temperature effects on the transition speed have not been studied yet. In this part of work, the electric pulses parameters, e.g., period, width, amplitude and the substrate temperature influence on transition were systematically investigated.

5.2.2 Experiments

The experimental set-up is illustrated in inset plot of Figure 5.3. The electrical pulses were generated by an HP4284A pulse generator and the voltage over VO₂ device were recorded and read out by an oscilloscope (Tektronix TDS 2012). A 580 Ω resistor (R_{LOAD}) was connected in series with the device to limit the current jump following MIT and protect the device. Figure 5.3 shows the voltage change across the device (V_D) when electric pulses were applied to trigger the MIT. The pulse amplitude $V_P = 20$ V, pulses period = 5 us, and pulse width = 800 ns. Electric pulses (V_P) were generated by a pulse-generator and recorded by an oscilloscope. As can be told by the V_D curve, a

sharp voltage drop occurred during pulses, with a response time as short as 400 ns. After the sharp drop, V_D then gradually decreased and overshot at the end of the pulse, which was caused by circuit oscillation. Combined with the R_{LOAD} , V_P and V_D , we can indirectly get the real-time resistance values of the device (R_D) using the equation: $R_D = V_D \times R_{load} / (V_P - V_D)$. It is noteworthy that R_{load} was measured to be stable with vibration of only 1~2 Ω even though it was heated up by the large current following MIT.

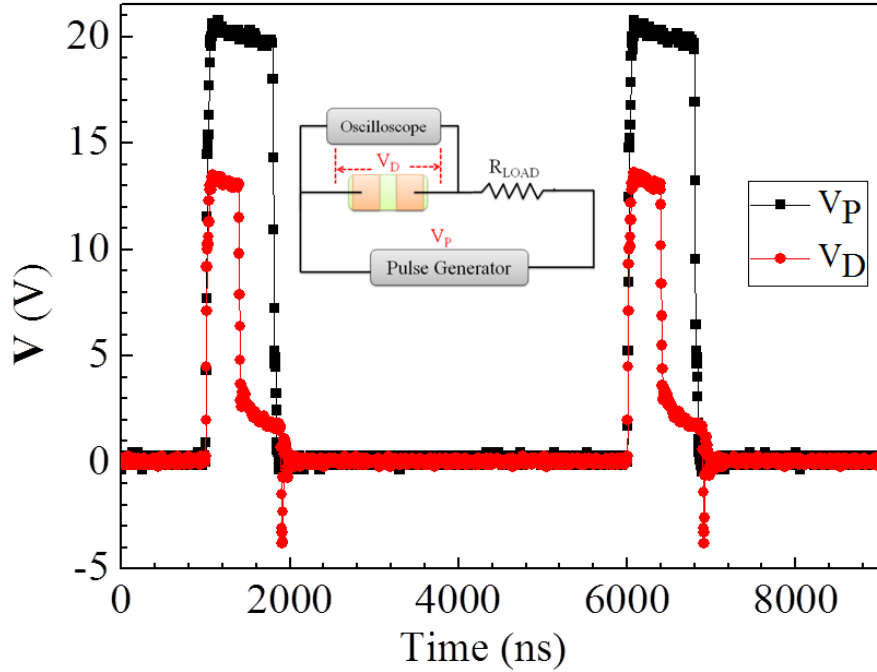


FIG. 5.3 Voltage response of a two-terminal VO_2 device under electric pulses. The inset plot is the diagram of circuits setup.

5.2.3 Results and Discussion

Figure 5.4 displays the voltage changes under pulses with varied pulse periods. Pulses amplitude is fixed to be 20V and width is 1 μ s, ambient temperature is measured to be 25 °C. When the period is 6.5 μ s, no sharp voltage drop was observed, indicating that the MIT had not been triggered yet. When the period shorten to 6.0 μ s, after about 600 ns response time, the voltage suddenly dropped from around 13V to around 4.0 V, with a transition time of around 30 ns. The resistance dropped from about 1010 Ω down

to 131Ω using aforementioned equation. When further shorten the period to $5.5\ \mu s$, $5.0\ \mu s$, $4.5\ \mu s$ and $4.0\ \mu s$, the response time gradually decreased and at period of $4.0\ \mu s$, the transition happens almost the same time as the pulses was applied onto the devices, implying the feasibility of fast MIT control. It is interesting that the initial resistances of each transition started at almost the same value around $1080\ \Omega$ and drop to almost the same value (131Ω), then it gradually decreased to final resistance of around 47Ω . The initial resistance is much smaller than the device resistance at room temperature as displayed in Figure 5.3 ($1.466\ k\Omega$), implying that the device was already heated up by the previous pulses. Before transition, the device gradual decreased from $1180\ \Omega$ to around $1010\ \Omega$, which is the effect of joule heating under voltage pulses. A general conclusion from Figure 5.4 is that the current pulse induced MIT is affected by previous pulses.

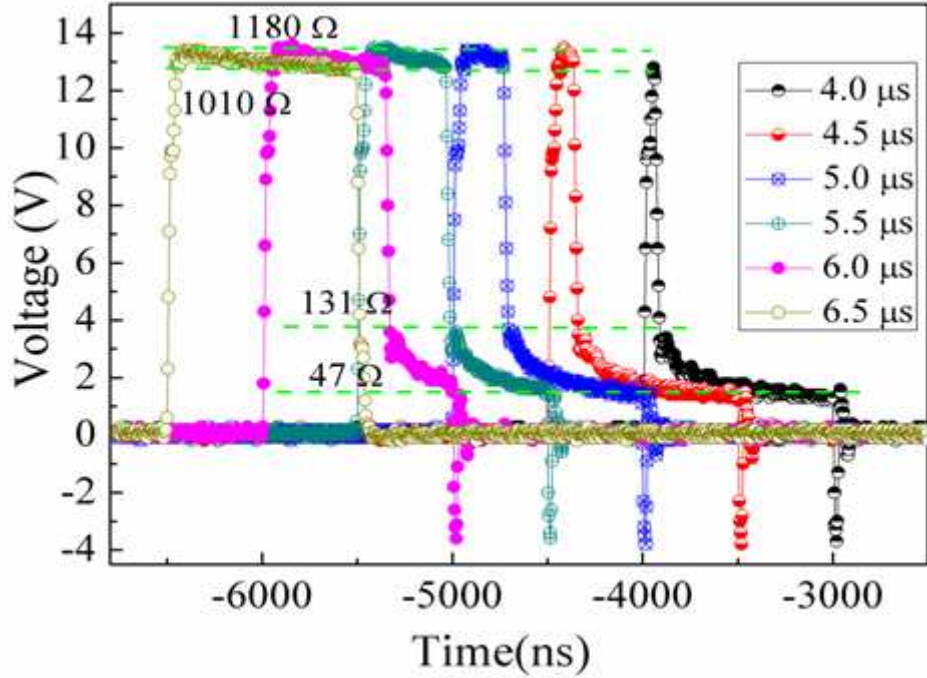


FIG. 5.4 Voltage over VO_2 two-terminal device under varied pulses period.

Figure 5.5 is a plot of voltage change under pulses with different width, varying form $1000\ \text{ns}$ to $800\ \text{ns}$. The pulses amplitude is $20\ \text{V}$ and period is $1\ \mu\text{s}$. When width

was set to be 800 ns, no MIT was observed, and when the pulse width was increased to 850 ns, an obvious voltage drop occurred. The response time of the MIT became shorter when further increased pulse width. Same as that in Figure 5.4, all MITs started and ended at almost the same resistance. It is obvious that the MIT is affected by the different joule heating ensuing MIT. The wider pulses generate more heating and kept the device at a relatively higher temperature when the next pulse arrived; hence it took shorter time for it to heat up the device. However, the device temperature difference is not apparent, as shown by the voltage value where it started to drop.

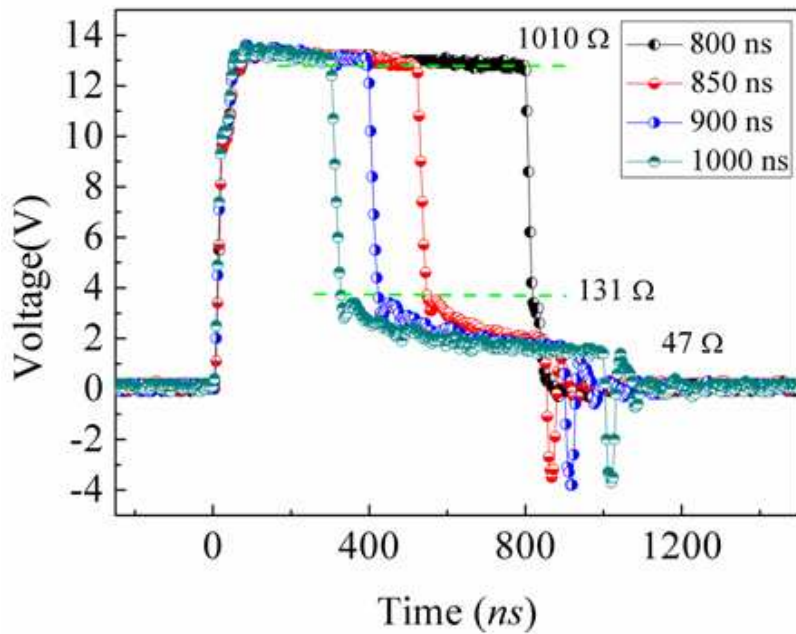


FIG. 5.5 Voltage over VO₂ two-terminal devices under varied pulses width at room temperature (25 °C).

Figure 5.6 displays the plot of voltage changes under pulses stimulation in time scale. The pulse width is 1μs and period is 5μs. The pulses amplitude was set with varied values: 20.0 V, 21.5 V, 22.5 V and 23.0 V. It is shown that for higher pulse amplitude, the time needed for MIT response was shorter. Similar with Figure 5.4 and 5.5, all transitions again occurred when the resistance of device reached a value close to 1010 Ω, though with small variation, which is reasonable considering the measurement error. When the voltage was higher, the RC oscillation became more obvious after

occurrence of MIT. Moreover, larger pulse amplitude leaded to shorter response time.

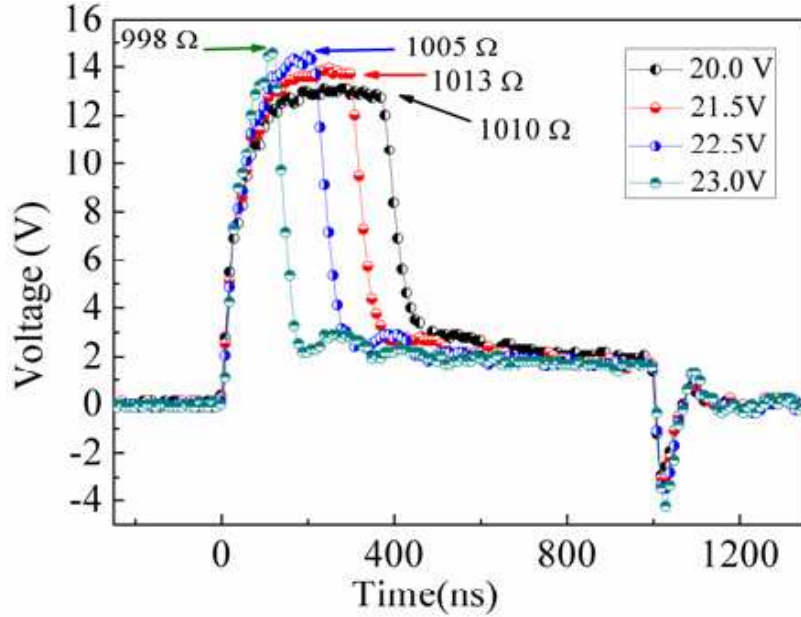


FIG. 5.6 Voltage over VO₂ two-terminal devices under varied pulses amplitude at room temperature (25 °C).

Figure 5.7 shows the voltage response of two-terminal devices under the same electric pulse but varied ambient temperature. The pulse width is 1μs, period is 5 μs and amplitude is 20 V. With higher substrate temperature, MIT occurred at smaller voltage (device resistance), which is consistent with previous report. The higher substrate temperature leaded to smaller resistance the end of the pulses. More heating was generated for transition under higher substrate temperature, which resulted in a smaller resistance between two consecutive pulses. When the temperature ramped up to 65 °C, partial of device gap was already tuned to metallic VO₂ and supported strong RC oscillation. The device resistance at end of each pulses decreased with the increase of the substrate temperature. These results again confirm that thermal heating got involved and closely related with MIT in VO₂ two-terminal channel, and higher ambient temperature resulted in smaller voltage (electric-field) to trigger MIT.⁷⁹

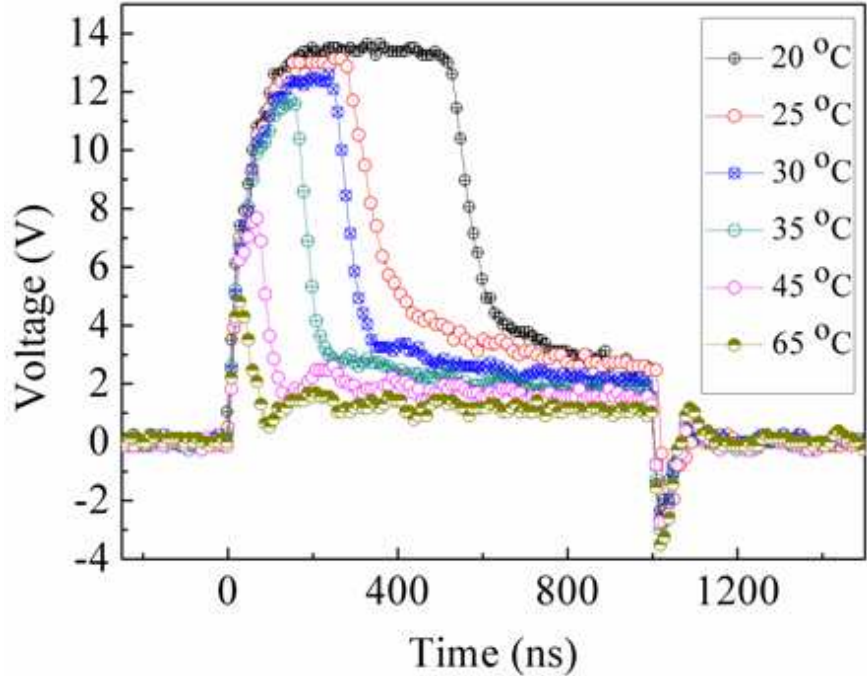


FIG. 5.8 Voltage over VO_2 two-terminal devices under different substrate temperature.

5.3.4 Summary

In conclusion, high-speed MIT was observed under combination of certain electric pulses parameters and ambient temperature. MIT in VO_2 thin films was found to be susceptible to pulses period, width, and amplitude as well as substrate temperature. Small variation in either parameter will result in obvious difference in transition response time. It is interesting that all the transition start at almost the same resistance (resistivity). After the MIT, the device resistance was further decreased by thermal heating; the RC oscillation prevailed when the final resistance was small enough. It is concluded that shorter period, longer width, larger amplitude and higher substrate temperature intend to shorten the MIT response time, which opens opportunity for fast switching performance.

Chapter 6

Electric Current Controlled MIT in VO₂ Thin Films

6.1 Abstract

This part of work investigates into the evolution process of VO₂ thin-films from the insulating phase to the metallic phase under current injection for the two-electrode based thin-film devices. Based on electrical characterization and Raman microscopic detection, it was found that there existed two critical current densities, based on which the insulator-to-metal transition process can be divided into three stages. In stage I with low current injection, VO₂ film in the insulating (semiconducting) phase acts as a resistor until the first critical current density, above which the insulator-metal transition is a percolation process with metallic rutile and insulating monoclinic phases coexisting (stage II); while beyond a second critical current density, a filamentary current path with pure metallic phase is formed with the remaining part outside of the current path receding back to the pure insulating phase (stage III).

6.2 Introduction

Vanadium dioxide (VO₂) has been proposed for several applications based on the nonlinearity and tunability of its electrical, dielectric and optical properties. It is known that VO₂ experiences a first-order metal–insulator transition (MIT) at a temperature of ~68 °C with a resistivity variation by 4-5 orders, accompanied by a structural phase transition from the low-temperature insulating monoclinic (M) phase to the high-temperature metallic rutile (R) phase. Across this phase transition, its dielectric function and optical properties undergo dramatic changes. These unique characteristics can be exploited for smart devices with reconfigurable or tunable capabilities, such as tunable metamaterials,⁵¹ microwave switching⁸⁰ and wavelength

conversion from mid-IR to near-IR for imaging.⁴⁶ The potential of using VO₂ thin films for terahertz modulation was previously reported, with more than a four-fold change of the transmitted electric field,²⁹ corresponding to a transmission intensity modulation depth of 95%, which is significantly higher than the reported~50% modulation depth of the state-of-the-art THz modulators.^{68, 81} To develop these potential devices which are based on the VO₂ MIT-related property change, it is critical to have convenient approaches to control the phase transition. In this regard, the VO₂ phase transition triggered by an electrical method is interesting. The electrically controlled VO₂ phase transition, either under metal-oxide-semiconductor (MOS) gate field control or under current injection, has been studied by several groups,^{56, 74, 79} and the Mott effect has been attributed to the observed phase transition. However, the MIT mechanism and the transition process are still in controversy^{82, 83} because of the closely coupled Joule heating effect related with the current injection. Even for the MOS structure, the thermal effect related to the gate leakage current cannot be completely excluded. From the scientific point of view, it is important to understand the fundamental principles of MIT in VO₂ although it has been debated for several decades. On the other hand, it is also necessary to elucidate the MIT evolution process under electric control for application development. To this end, by combining electrical measurement with micro-Raman spectroscopic probing, we report in this paper the evolution process of how the insulator phase is transformed into the conductor phase in VO₂ thin films under current injection.

6.3 Experiments

150 nm thick VO₂ thin films were epitaxially deposited on c-sapphire substrates by reactive DC magnetron sputtering of a high purity (99.95%) vanadium metal target in an Ar and O₂ gas mixture. The growth temperature and sputtering gas ambient are optimized and precisely controlled to yield a pure VO₂ phase. The sputtering pressure was set at 3 mTorr with an O₂/Ar flow ratio of 11%, and the

growth temperature was maintained at 575 °C. No post-growth annealing process was carried out. The deposited VO₂ was found to be epitaxial films with (020)_M as the growth plane. Since M-phase bulk VO₂ has a β angle of 122.6°, different from the hexagon structure of c-sapphire, triple-domain structure in VO₂ films was observed. The details of material growth and its properties can be found in.⁸⁴ VO₂ two-terminal devices were fabricated based on photolithography, mesa etching, electron-beam metal deposition and liftoff process. Ti/Au metal stack was used as electrodes. Current–voltage (I–V) relation was measured, which reveals a critical current density for the onset of MIT and current path formation. Micro-Raman spectroscopy based on a LabRAM HR 800 confocal micro-Raman spectrometer with a 514.5 nm Ar+ laser excitation and a reduced power of a few mW was employed to investigate the phase evolution process by discriminating the different phases in and out of the current path.

6.4 Results and discussion

In the so-called I mode, the applied current through the two-terminal device was ramped up, and the voltage variation with current was recorded, as shown in Figure 6.1 for a representing VO₂ device ($L = 20 \mu\text{m}$, $W = 120 \mu\text{m}$), similar with the observation from Lee et. al.⁷⁵ The curve can be divided into three distinctive sections, corresponding to three stages of the transition from the insulating *M*-phase to the metallic *R*-phase. In stage I represented by points A to C', V almost linearly increased with small I, indicating that the device had a roughly constant resistance and VO₂ was in the insulating M-phase. In stage II represented by C' - E, when I reached a first critical value at point C', V experienced a sharp drop from C' to C, indicating the occurrence of a sharp resistance drop. With the applied current continuously ramped up, the device behaved with a negative resistance until it reached a second critical current value at point E' where it experienced a second sharp voltage drop to point E, and at the same time a dark color path between the two electrodes was observed under an optical microscope, as shown by the inset of Figure 6.1. This filamentary path, as will be

confirmed later on, is the metallic phase VO_2 which forms the continuous low-resistive path for the current flow between the electrodes. In stage III beyond point E, once the metallic current path is formed, V over the device maintained an almost constant value while the width of the dark color current path widened itself proportionally with the increment of the injected current, similar phenomenon previously reported by Joe's group.⁸³ It is worth emphasizing that if we measure the I-V relation in the V mode by applying swept voltage, the more common single-step MIT will be observed.

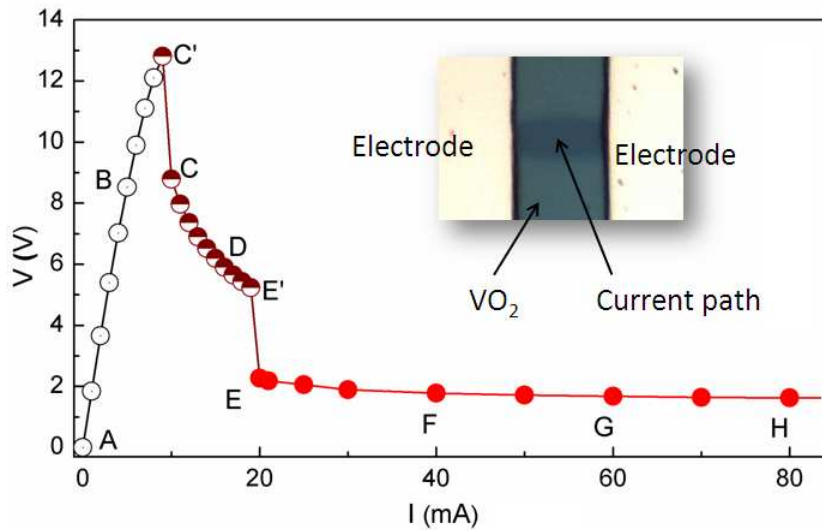


FIG. 6.1. Voltage drop on a representative two-terminal device ($L=20 \mu\text{m}$, $W=120 \mu\text{m}$) with injected current ramped up. The inset is the optical microscopic image of VO_2 channel at E point, and the dark color current path is clearly observable.

It is noted that for the same device, the current path will appear at the same location in the repeated measurements, which provides the possibility to probe the phase evolution process. Figure 6.2(a) shows the micro-Raman spectra of the same current path area at different injected currents, and Figure 6.2(b) is the zoom-in view of the rectangular region of Figure 6.2(a). The laser beam was focused at the known area where the current path would show up when I reached to ~ 20 mA. Under the applied current conditions corresponding to points A and B in Figure 6.1, Raman spectrum had seven peaks located at 186 , 218 , 304 , 334 , 388 , 493 , and 610 cm^{-1} , all of which can be assigned to Ag active modes of the VO_2 insulating *M*-phase,^{85, 86} indicating the

insulating *M*-phase in the stage I of Figure 6.1. As *I* increased (points C and D), the intensities of these seven Ag modes declined and some peaks vanished, while a new peak at around 560 cm^{-1} gradually appeared, which is assigned as the A_{1g} active mode of rutile VO_2 . The zoom-in view of Figure 6.2(b) clearly presents the changing trend with the A_{1g} peak growing while the A_g peaks (610 cm^{-1}) fading. These observations point to a mixed insulating *M*-phase and metallic *R*-phase coexistence during the stage II of Figure 5.1. When *I* further increased to point E where an observable current path began to appear, all the monoclinic A_g peaks disappeared and the only peak remained is the A_{1g} peak, indicating that the current path region was transformed to the pure metallic *R*-phase, corresponding to stage III of Figure 6.1

Figure 6.2(c) shows the Raman spectra measured under the same current conditions as those in Figure 6.2(a), but for the part of VO_2 that was out of the current path, and 5.2(d) is the zoom-in view of the rectangular area of 6.2(c). By comparing Fig. 6.2(c) and (d) with 6.2(a) and (b), it is noticed that in stage I and II, that is, before the observable current path appeared, the spectra were the same, but after the metallic current path was formed, the region that was out of the current path retreated from the mixed metallic *R*- and insulating *M*- phases back to the pure insulating *M*-phase.

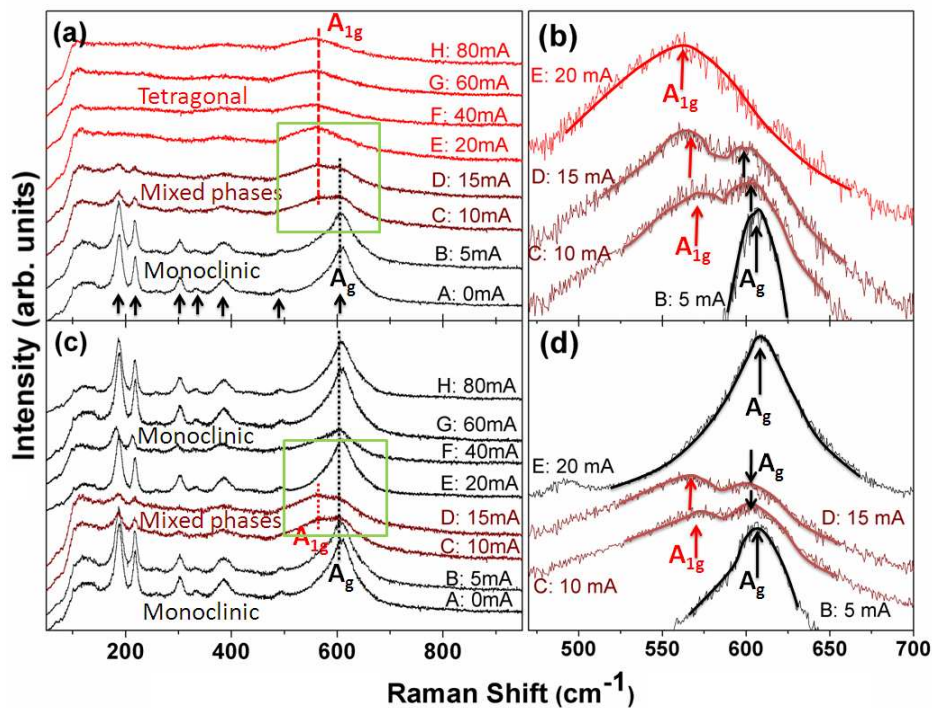


FIG. 6.2. (a) Micro-Raman spectra along the current path at different injected current, and (b) its zoom-in view of selected modes. (c) Micro-Raman spectra for the area out of the current path, and (d) its zoom-in view of selected modes. The spectra were shifted in vertical direction for clear view.

With these observations, the evolution process of VO_2 metal-insulator transition under current injection can be summarized as the following: in stage I with a low current density (J) or electric field (E), VO_2 is in its pure insulating M -phase, acting as a linear resistor; as the E or J arrives at a critical value, metallic R -phase begins to nucleate in the background insulating M -phase to form low resistive islands, inducing a steep reduction of the total resistive value, corresponding to the sharp drop of V from C' to C in Figure 6.1. As these metallic islands grow with I ramping-up, the total resistive value of the VO_2 device diminished, leading to the negative resistance behavior in stage II. The evolution picture in this stage is consistent with the percolation theory of the thermally-driven first-order phase transition.^{72, 87} When the metallic islands finally connected with each other to form a continuous low-resistive path from one electrode to the other, a second sharp voltage sharp drop happens from point E' to E with a discernible dark-color current path formed. Unlike the uniformly heating driven MIT, the low-resistive current path formation leads current density in the region out of the current path to dramatically diminish below the critical value, so the metallic islands in this part of VO_2 disappear and retreat back to the pure insulating phase as in stage I. This statement also suggests that it is the current density which is more critical than the electric field for the MIT transition of VO_2 thin-films under current injection condition; otherwise, the low-resistive current path should fill the whole width of the device channel, where the electric field is the same.

6.5 Summary

In this section the evolution process of VO_2 thin-film phase transition under current injection was investigated. Through electrical characterization and Raman

microscopic probing of the insulating and metallic phases, we found that the MIT of VO₂ under current injection is a three stage process, determined by two critical current densities. VO₂ is in the pure insulating phase below the first critical current density, which determines the onset of insulator-to-metal transition. Above this current density, the insulator-to-metal transition is a percolation process with metallic phase nucleation and growth in the background of the insulating phase. Beyond the second critical current density, a pure metallic current path is formed between the two electrodes with the remaining part of VO₂ material receding back to the pure insulating phase. With further increase of injected current, the metallic current path will expand. These findings will facilitate the development of electrically controlled VO₂ devices in several potential applications.

Chapter 7

Structural, Electrical, and Terahertz Transmission Properties of VO₂

Thin Films Grown on c-, r-, and m-plane Sapphire Substrates.

7.1 Abstract

The structure, metal-insulator transition (MIT), and related Terahertz (THz) transmission characteristics of VO₂ thin films obtained by sputtering deposition on *c*-, *r*-, and *m*-plane sapphire substrates were investigated by different techniques. On *c*-sapphire, monoclinic VO₂ films were characterized to be epitaxial films with triple domain structure caused by β -angle mismatch. Monoclinic VO₂ β angle of 122.2° and the two angles of V⁴⁺-V⁴⁺ chain deviating from a_m axis of 4.4° and 4.3° are determined. On *r*-sapphire, tetragonal VO₂ was determined to be epitaxially deposited with VO₂ (011)_T perpendicular to the growth direction, while the structural phase transformation into lower symmetric monoclinic phase results in (2̄11) and (200) orientations forming twinned structure. VO₂ on *m*-sapphire has several growth orientations, related with the uneven substrate surface and possible inter-diffusion between film and substrate. Measurements of the electrical properties show that the sample on *r*-sapphire has MIT property superior to the other two samples, with a resistivity change as large as 9×10^4 times and a transition window as narrow as 3.9 K, and it has the highest resistivity with the lowest free carrier density in the insulating phase. THz transmission measurements on VO₂ films grown on *r*-plane sapphire substrates revealed intensity modulation depth as large as 98% over a broadband THz region, suggesting that VO₂ films are ideal material candidates for THz modulation applications.

7.2 Introduction

The metal-insulator transition (MIT) of vanadium dioxide (VO₂) has drawn

intense scientific interest for understanding fundamental mechanisms of these transformations.⁸⁸ Single crystal VO₂ exhibits an abrupt change of electrical resistivity up to five orders of magnitude within 0.1 °C at a temperature of ~ 68 °C, accompanied by concomitant changes in the observed optical properties, e.g., transmission and reflectivity, especially in the terahertz (THz) and far infrared (IR) spectral ranges.^{29, 89, 90} These properties render VO₂ a promising candidate for a number of interesting applications in electronics and photonics. The phase transition may also be triggered by optical excitation³⁵ and application of electric field,⁵⁶ providing more convenient approaches to control prospective devices. These unique characteristics can be exploited for smart devices with reconfigurable or tunable capabilities, such as photo-induced sub-picosecond shifting of the photonic bandgap,⁹¹ radio frequency (RF)/microwave switches,⁴⁵ wavelength conversion from mid-IR to near-IR for imaging,⁴⁶ and tunable metamaterial devices⁴⁷ or with memory effect.⁹²

One particular potential of VO₂ application is to develop THz optical switches, filters and modulators for imaging, spectroscopy, and wireless communication applications. The performance of such THz devices is critically dependent on the modulation depth. Two-dimensional electron gas based modulators can only achieve a few percentage of modulation,³¹ while the state-of-the-art meta-material based THz switches and modulators have an intensity modulation depth of 52% but with an intrinsically very narrow bandwidth at the designed resonant frequency.^{68, 81} Consequently, alternative materials are needed to implement efficient THz switches and modulators with larger modulation depths. Since insulating VO₂ is highly transparent above 45 μm (i.e., below 6.7 THz) with very low loss mainly caused by low-density ($\sim 10^{18}$ cm⁻³) free carrier absorption, while metallic VO₂ has a high free carrier concentration ($>10^{21}$ cm⁻³) with large absorption, VO₂ is an ideal candidate for THz modulation applications.

In order to achieve a large modulation depth with a small insertion loss for THz or infrared applications, it is critical to control the background free carrier density of insulating VO₂ and reach a large resistivity variation in the phase transition. However,

the MIT characteristics of VO₂ thin films, such as transition temperature, resistivity, resistivity-change amplitude and hysteresis window, vary in a wide range due to crystal quality, grain size and boundaries, built-in strain related with substrates, defects related self-doping, and other factors.^{16, 93-95} Since the performance such as modulation depth and insertion loss of terahertz modulators and switches is directly related to VO₂ material and MIT transition properties, VO₂ thin films with improved MIT characteristics is a key requirement. Sapphire is relatively transparent to THz waves and is a suitable substrate for epitaxial growth of VO₂ thin films. Although considerable efforts have been dedicated to improve MIT characteristics in VO₂ films grown on sapphire substrates under different growth conditions, the effects of the substrate orientation remain practically unexplored. In this paper we performed a detailed investigation on the morphological, structural, electrical and optical properties of VO₂ thin films grown on *c*-, *r*-, and *m*-plane sapphire substrates under identical growth conditions. Our results indicate that the properties of VO₂ films are strongly influenced by the sapphire substrate orientation. VO₂ films grown on *r*-plane sapphire substrates exhibited lower MIT transition temperature and hysteresis window and larger THz intensity modulation depth when compared to similar samples grown on *m*- and *c*-plane sapphire substrates.

7.3 Experiments

VO₂ thin films with ~120 nm in thickness were grown on *c*-, *r*- and *m*-plane sapphire substrates under identical conditions by computer controlled pulsed DC reactive sputtering deposition from a high purity vanadium target (99.95%). Considering the complex phases of vanadium oxide material system, the growth temperature and sputtering gas ambient were optimized and precisely controlled to yield high purity VO₂ phase. The sputtering pressure was set at 3 mTorr with an O₂/Ar flow ratio of 11%. All three samples were grown at 575 °C. No post-growth annealing process was carried out. This growth condition was confirmed to give high quality VO₂

film on *c*-plane sapphire.⁸⁴

The structural and morphological properties of the three samples were studied by X-ray diffraction (XRD), scanning electron microscopy (SEM), and transmission electron microscopy (TEM). XRD θ - 2θ and Φ scans were performed using a Philips X’Pert Diffractometer with Cu K α radiation. The surface morphology images were acquired using field-emission SEM. Tecnai F20 analytical microscope was used to acquire high-resolution TEM (HRTEM) images and selected-area-electron-diffraction (SAED) patterns on different samples. Room temperature Raman spectra were obtained in the backscattering configuration using 514.5 nm laser excitation with less than 10 mW at the sample. The resistivity dependence on sample temperature (T) in heating and cooling cycles were measured based on van der Pauw method using a Hall system. For reliable resistivity and Hall measurements, Ti (50 nm)/Au (120 nm) metal stacks deposited by e-beam evaporation and lift-off process were used as electrodes. Reliable Hall data across MIT is difficult to measure because of an inhomogeneous composite oxide with mixed insulating and metallic phases.^{72, 96, 97} Hall measurement reported here was taken at room temperature for the homogeneous *M*-phase VO₂. Time-domain THz transmission experiments were performed using an ultrafast fiber laser emitting at \sim 1560 nm wavelength which produces 90 fs pulses at 100 MHz repetition rate with an average power of 250 mW. The THz emitter/detector consists of photoconductive antennas based on low-temperature InGaAs/InAlAs multi-layer structures. The modulated photocurrent in the THz detector is measured using a lock-in amplifier and the THz pulse waveform is obtained by performing a Fourier transform of the delay time, which is varied using a retro-reflector mounted to a linear translation stage. A detailed description of time-domain THz transmission measurement can be found in the literature.^{98, 99} All THz transmission measurements were performed at normal incidence in the 0.1-2.0 THz range. Throughout all THz transmission measurements the laser power was kept constant.

7.4 Results and Discussion

The three VO₂ samples grown on *c*-, *r*-, and *m*- sapphire substrates are abbreviated C, R, and M. Figure 7.1(a) shows a representative example of a THz transmission measurement for the R sample at two different temperatures: 40 °C (insulating phase) and 90 °C (metallic phase). The THz transmission curves comprise of the main transmission pulse and low intensity reflected pulses at the substrate/VO₂-air interface. Figure 7.2(b) shows the truncated Fourier transform (without the reflected pulses) of the time-domain transmission shown in Figure 7.1(a). Here we focus on the first order information; detailed discussion of the THz properties will be presented in a separate publication. It can be noticed from Figure 7.1(a) that the amplitude of the electric field of the transmitted THz wave varies significantly as VO₂ changes between the insulating and metallic phase. This is confirmed in Figure 7.1(b) where the field change ratio is uniform throughout the detection range of our measurement system. The transmitted field amplitude ratio of insulator phase to the metallic phase (E_I/E_M), modulation depth of the electric-field (MD_E), transmitted beam intensity ratio (I_I/I_M), and intensity modulation depth (MD_I) for the three samples are listed in Table I. Here MD_E and MD_I are defined as: $MD_E = (E_I - E_M)/E_I$ and $MD_I = (I_I - I_M)/I_I$.⁸¹ A maximum field modulation depth of 85% and intensity modulation depth of 98% is determined for the *R*-sample. The modulation depths obtained for all three VO₂ samples are much higher than previous reported values,^{68, 81} confirming that VO₂ is an ideal material for THz modulation applications. Another significant merit of VO₂ MIT based THz modulator is that, in contrast to the state-of-the-art metamaterial counterparts that only works at the designed resonant frequency, it is intrinsically broadband with essentially constant modulation depth across the investigated THz range, as evidenced from Figure 7.1(b), considering that the modulation is mainly caused by the free charge carrier absorption.

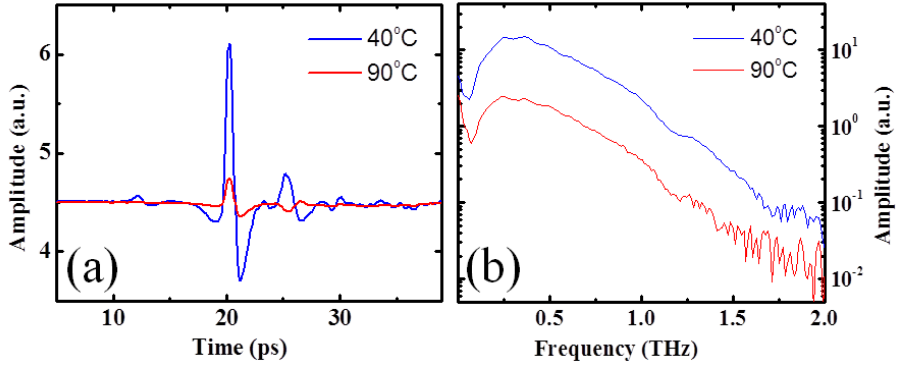


FIG. 7.1 Representative (a) time-domain and (b) frequency-domain THz transmission of VO₂ thin-film on sapphire substrate (R-sample). Only the dominant peak in (a) was used in the Fourier transformation to obtain the frequency-domain transmission in (b).

Table II Comparison of THz modulation performance, electrical properties at 300 K, and MIT properties of the three samples.

Sample	THz modulation				Electrical properties (300K)			Metal-insulator Transition		
	$\frac{E_I}{E_M}$	MD_E (%)	$\frac{I_I}{I_M}$	MD_I (%)	ρ (Ωcm)	n (10^{18}cm^{-3})	μ (cm^{-2}/Vs)	ΔR (10^4)	T _c (K)	ΔH (K)
C	3.9	74	15.2	93	16.3	6.7	0.052	4.8	344	6.1
R	6.4	85	41.0	98	18.2	3.1	0.107	9.4	337	3.9
M	5.9	83	34.8	97	12.3	2.9	0.172	5.5	338	5.2

The THz transmission can be described based on the dielectric property of solids which is determined by the Drude mechanism, Debye relaxation, and phonon resonance. In the measured THz frequency region the free-carrier effect is dominant. To understand the different THz performance among these three samples that are listed in Table I, the electric property at room temperature, including resistivity (ρ), free electron concentration (n) and mobility (μ) were determined from Hall measurements, and are also listed in Table I. The resistivity changes through MIT as a function of temperature are presented in Figure 7.2. All three samples undergo abrupt resistivity change across MIT. VO₂ MIT characteristics, including resistivity change ratio (ΔR) across MIT,

critical transition temperature under temperature ramping-up (T_c), and hysteresis window (ΔH) are also summarized in the Table. At room temperature, the insulating phase VO_2 of the R-sample has the highest resistivity and the largest ΔR of 9.4×10^4 through MIT, giving the largest field modulation depth of 85%, while C-sample, although has a slightly higher resistivity than M-sample, has the highest resistivity at metallic phase with a smallest ΔR of 4.8×10^4 through MIT, leading to lowest field modulation depth (~74%). The changes on the electrical properties of the VO_2 films with the temperature is consistent with that obtained from the THz transmission measurements, confirming that free electron related Drude mechanism is the dominant factor determining the THz dielectric property of VO_2 . In addition, we determined that the R-sample has the narrowest ΔH of 3.9 K and T_c of 337 K, while the C-sample has the widest ΔH of 6.1 K and highest T_c of 344 K.

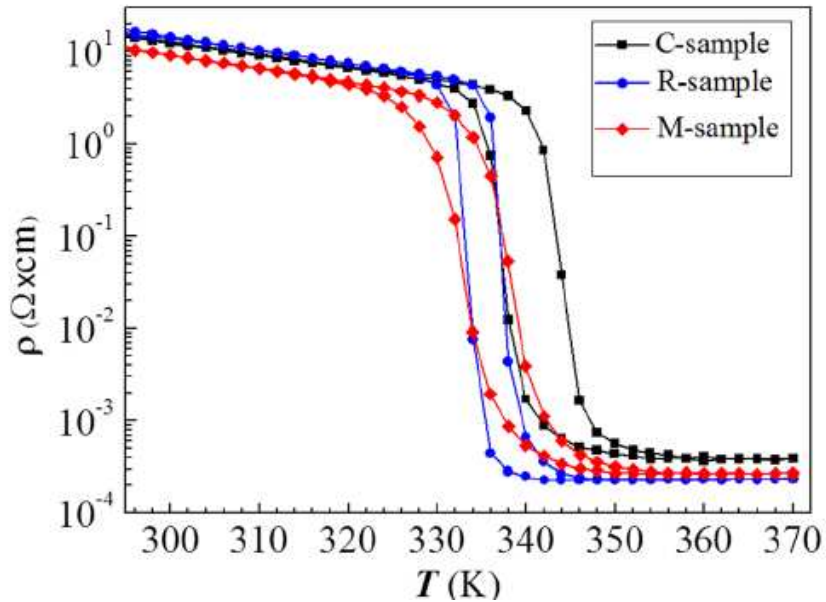


FIG. 7.2 R-T hysteresis curves for the three samples through the MIT process.

It is anticipated that VO_2 films grown on the different orientation of sapphire substrates will exhibit different crystal orientation and quality, including grain boundary, grain size, built-in strain, and V-V bond orientation related to the growth direction. These differences may impact free carrier density, MIT temperature, and

hysteresis, and thus affecting the THz modulation performance. Figure 7.3 shows the surface morphology of the three samples based on SEM measurements. All the samples exhibited crystalline morphology, with the R-sample exhibiting the largest grain size with elongated shape in one direction and the C-sample having the smallest one. More prominent is that the C-sample appears to have a porous, discontinuous top surface, while R- and M- samples have compact and closely connected grains forming a continuous film. We provide below a detailed crystal structure analysis for the three samples. The MIT process in VO_2 is accompanied by a crystal-structure transformation from a high-temperature tetragonal-type (space group $P4_2/mnm$) to a low-temperature monoclinic (space group $P2_1/c$) structure. Although VO_2 was grown at high temperature, i.e., in tetragonal (T) phase, most of the structural characterization reported here was carried out at room temperature with VO_2 in a monoclinic (M) phase. Therefore, the nomenclatures used are based on monoclinic structure, unless specified otherwise.

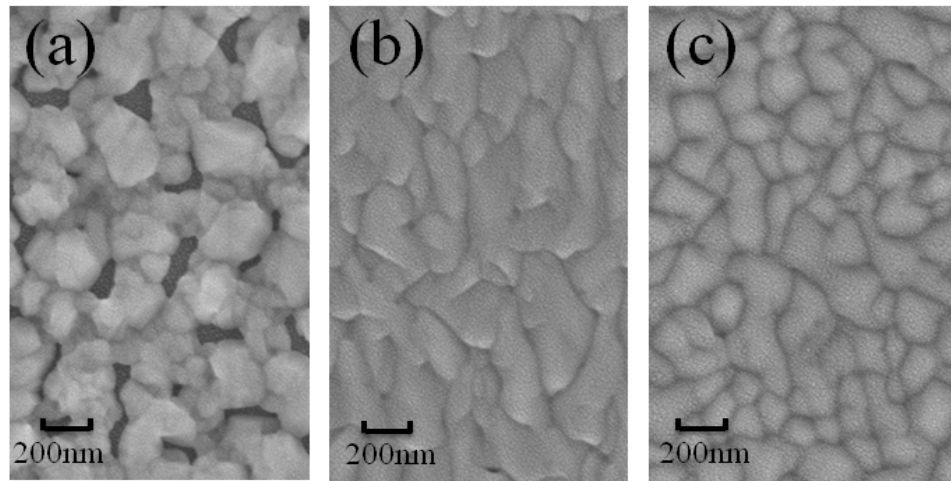


FIG. 7.3 The surface morphology of the three samples (a) C-sample, (b) R-sample, and (c) M-sample observed by SEM.

Figure 7.4 shows the XRD patterns of the C-sample with (a) θ - 2θ and (b) and (c) Φ scans, indicating a triple-domain hetero-epitaxial structure. In Figure 7.4(a), two peaks related to VO_2 were observed in the θ - 2θ scan at $2\theta \approx 39.83^\circ$ and 85.85° . These can be assigned to either the (020) & (040) or the (002) & (002) diffractions,

respectively, since these two group peaks are very close to each other. One method to differentiate them is to find the in-plane orientation of the thin film by performing off-axis Φ scans. Consequently, we measured the VO_2 (011) diffraction at $2\theta=27.88^\circ$ and $\Psi=44.93^\circ$, and the VO_2 (102) diffraction at $2\theta=53.10^\circ$ and $\Psi=17.61^\circ$.⁶⁹ Figure 35(b) shows the six-fold periodic Φ scan peaks corresponding to VO_2 (011), while Φ scan of VO_2 (102) yields no peaks (not shown here). We conclude that VO_2 films in the *M* phase epitaxially grows on *c*-sapphire with VO_2 (020)// Al_2O_3 (0006), and the two peaks in Fig. 35(a) are the in-plane diffractions from the (020) and (040) planes. This conclusion is further confirmed by the SAED pattern in Figure 7.5(b), which will be discussed later. The result is consistent with previous reports,^{61, 100} but differs from the conclusion in a recent publication¹⁰¹ that VO_2 grown on *c*-sapphire has an out-of plane growth direction of [002].

Considering that the in-plane angle β of *M*-phase bulk VO_2 is $\sim 122.6^\circ$, different from 120° angle of the hexagonal structure in sapphire basal plane, triple domain structure based on triple symmetry of the *c*-sapphire plane will be formed in (020) VO_2 growth plane.¹⁰⁰ Further considering the two-fold symmetry of monoclinic structure, six-fold symmetric (011) peaks are observed. More interestingly, double peaks at each 60° symmetric position are observed in Figure 7.4(b). This phenomenon has only been reported for VO_2 synthesized by oxidizing V_2O_3 at high temperature (1000°C).¹⁰⁰ The observed double peaks at each 60° symmetric position can be understood by considering the β angle mismatch.²⁹ The six-fold symmetry with twin peaks at each 60° position was caused by β -angle mismatch. Three-fold symmetric Al_2O_3 (1 $\bar{1}$ 02) peak positions are also shown indicating a $\sim 30^\circ$ rotation of VO_2 [100] from Al_2O_3 [$\bar{2}$ 110] direction. Al_2O_3 (1 $\bar{1}$ 02) Φ scan peaks are also presented in Figure 7.4(b), corresponding to the triple-fold symmetry of Al_2O_3 (1 $\bar{1}$ 02) planes. The relative position between Al_2O_3 (1 $\bar{1}$ 02) peak and VO_2 (011) peak indicates $\sim 30^\circ$ rotation between VO_2 [100] and Al_2O_3 [$\bar{2}$ 110] directions. Figure 7.4(c) is the VO_2 (220) Φ scan measured at $2\theta=55.65^\circ$ and $\Psi=43.05^\circ$, again showing the six-fold symmetry. Interestingly, at each 60° symmetric position, symmetric triple peaks were measured.

In the structural phase transformation from the tetragonal rutile type to the monoclinic type, V^{4+} ions pair and twist from the originally equal spaced rutile position, leading to the zigzag chain. The observed triple peaks at each 60° symmetric position is attributed to V^{4+} - V^{4+} pair chain rotation away from the a_m axis of a monoclinic cell. The paired V^{4+} - V^{4+} chain forms angle δ_1 with a_m axis and the unpaired neighboring V^{4+} - V^{4+} gives angle δ_2 . Based on the relative angle of the three peaks at each 60° symmetric position, average values $\delta_1=4.40^\circ$ and $\delta_2=4.29^\circ$ were determined.

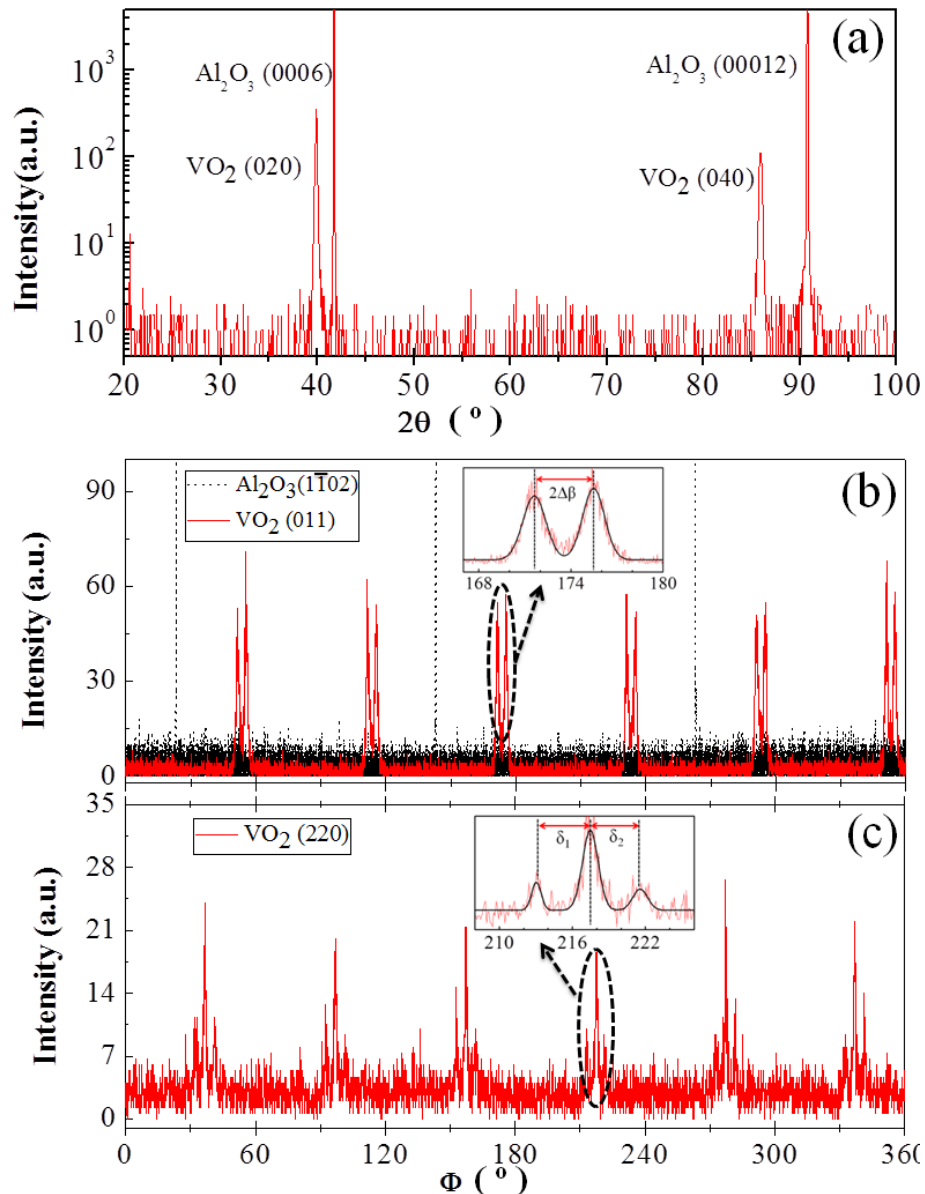


FIG. 7.4 XRD patterns of VO_2 thin film on c -sapphire. (a) In-plane θ - 2θ scan, (b) Off-axis (011) plane Φ scan, and (c) Off-axis VO_2 (220) plane Φ scan

TEM results for sample C are presented in Figure 7.5. The granular structure, with discontinuous surface morphology observed by SEM in Figure 7.2(a), is confirmed by the cross-sectional TEM micrograph in Figure 7.5(a). The TEM reveals that the columnar grains are well connected. The abrupt interface between the VO_2 layer and the sapphire substrate indicates no substantial chemical interaction took place. The high resolution TEM study (not shown here) reveals that in each grain, the film is defective at the interface area, possibly due to the high oxygen vacancy density; above the interface, the grain grows epitaxially without obvious defects in the film lattices. Figure 7.5(b) shows the corresponding SAED pattern along Al_2O_3 [10 $\bar{1}$ 0] zone. The indexes in SAED patterns again verify that the in-plane orientation of VO_2 is (020) rather than (002). The complete epitaxial relationship between VO_2 and *c*-sapphire hence can be concluded as VO_2 (020) || Al_2O_3 (0006) in the growth direction and VO_2 ($\bar{2}$ 02) || Al_2O_3 (11 $\bar{2}$ 0) in the growth plane.

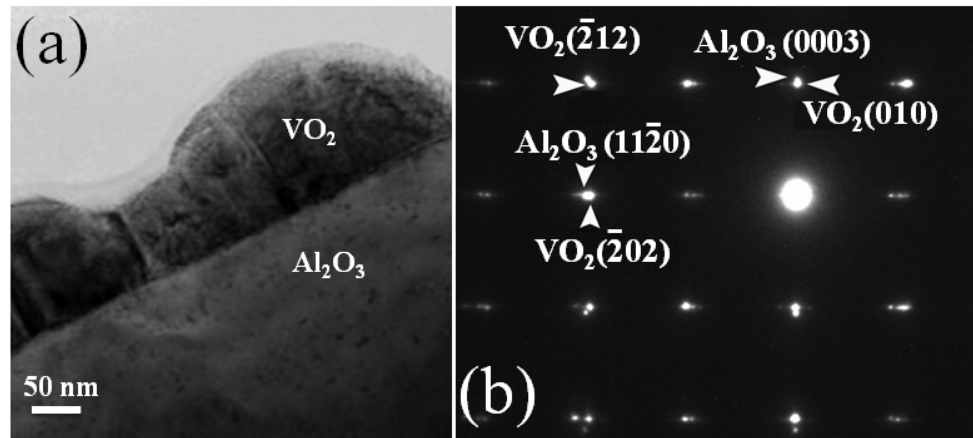


FIG. 7.5 TEM study of C-sample: (a) Cross-sectional TEM image, and (b) SAED pattern along *c*-sapphire [10 $\bar{1}$ 0] zone.

Figure 7.6(a) is the on-axis θ - 2θ scan of sample R, with a single VO_2 peak observed at 37.08° . This peak is very close to the expected Bragg angles of the VO_2 (200) and ($\bar{2}$ 11) planes at $2\theta=37.140^\circ$ and $2\theta=37.069^\circ$, respectively. To further confirm the growth orientation of the VO_2 thin film, Φ scans of the off-axis peak VO_2 (210) at $2\theta = 42.353^\circ$ were performed. It is interesting that for both $\Psi=68.19^\circ$ and 29.06° ,

which are calculated angles between planes (210) & ($\bar{2}11$) and planes (210) & (200), respectively, Φ scan peaks were observed (not shown here). This indicates that sample R might have both ($\bar{2}11$) and (200) growth orientations on *r*-sapphire, which is resulted by the twin domains formation in the sample, as confirmed by the TEM study. Figure 7.6(b) shows the comparing of high temperature tetragonal VO_2 (011)_T peak with the room temperature monoclinic VO_2 ($\bar{2}11$)/(200) peak, indicating the structural transformation to the low symmetric monoclinic phase leading to the single (011)_T growth plane split into twinned (200)/($\bar{2}11$) orientations.

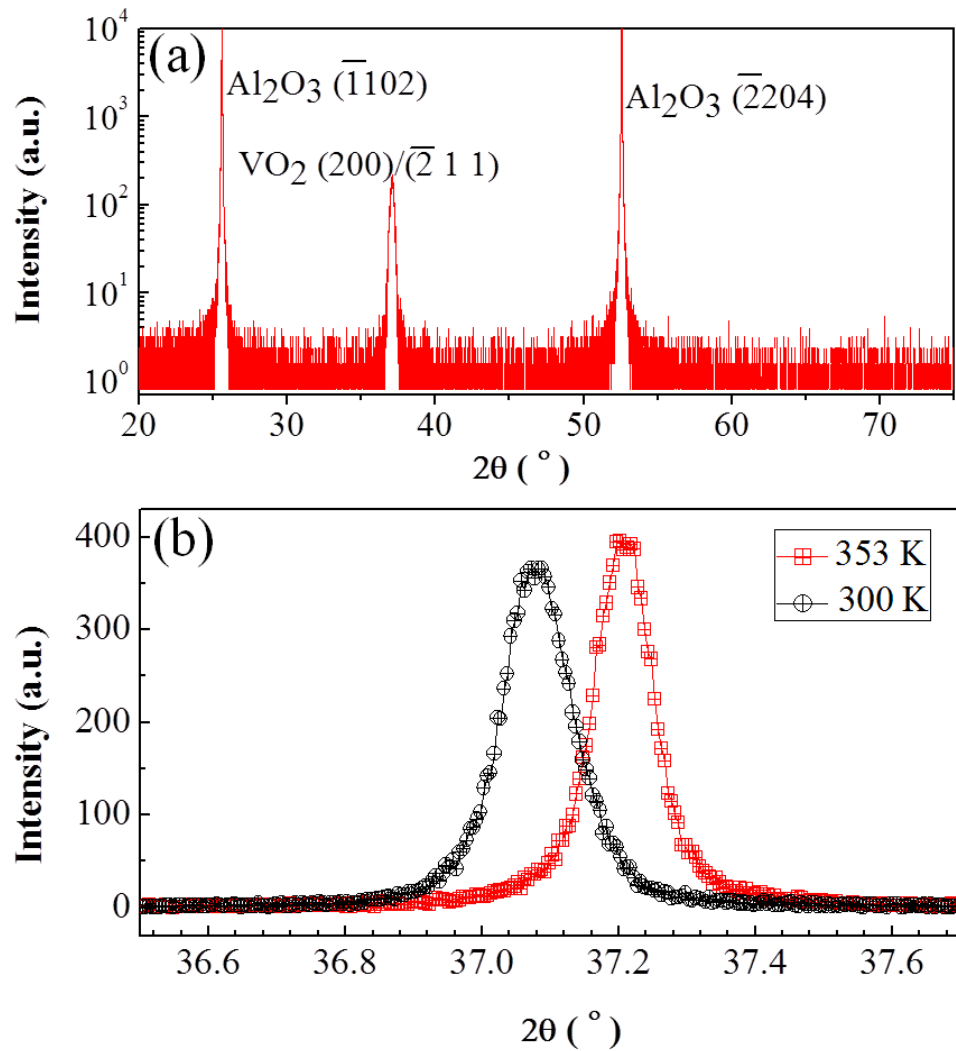


FIG. 7.6 XRD patterns of VO_2 thin film on *r*-sapphire. (a) In-plane θ - 2θ scan (b) θ - 2θ scan for ($\bar{2}11$)/(200) peak at room temperature and (011)_T peak at 353 K.

The cross-sectional TEM image in Figure 7.7(a) clearly shows that VO₂ film of sample R has high epitaxial quality with obvious twin structures. The twin boundaries are tilted relative to the growth direction with an angle, marked as “A” in Figure 7.7(a), measured to be $\sim 45^\circ$. Figure 7.7(b) is the high resolution TEM image of the interfacial area between the VO₂ layer and the substrate. A very clean VO₂-sapphire interface and VO₂ lattices indicate the high quality growth of the film. Two twin interfaces along with their two side mirror lattices are clearly observed and marked in Figure 7.7(b). The SAED in Figure 7.7(c), obtained from the film-substrate interface, consists of two sets of VO₂ diffraction spots both from zone [111] and one set of sapphire spots from the [2 $\bar{2}$ 01] zone. The two sets of VO₂ diffractions are symmetric along the thin line labeled in the diffraction pattern. This again suggests the twin structure that is consistent with the low magnification and HRTEM images where clear twin interfaces were observed. The twin direction is $\sim 45^\circ$ from the out-of-plane direction and is again consistent with the TEM images (Figure 7.7 a and b). The SAED results confirm the off-axis XRD Φ scan results. The epitaxial relationship for one set of the VO₂ diffraction dots is concluded as VO₂($\bar{2}11$) || Al₂O₃($\bar{1}102$) and VO₂[111] || Al₂O₃[2 $\bar{2}$ 01]; while for the other diffraction set, it is VO₂($\bar{2}11$) || Al₂O₃(0 $\bar{1}12$) and VO₂[111] || Al₂O₃[2 $\bar{2}$ 01]. Using the standard reference data from JCPDS Card. No. 72-0514, the angle between VO₂ planes (200) and ($\bar{2}11$) is calculated to be 44.79° , very close to the 45° tilt angle of the twin boundaries relative to the growth direction.

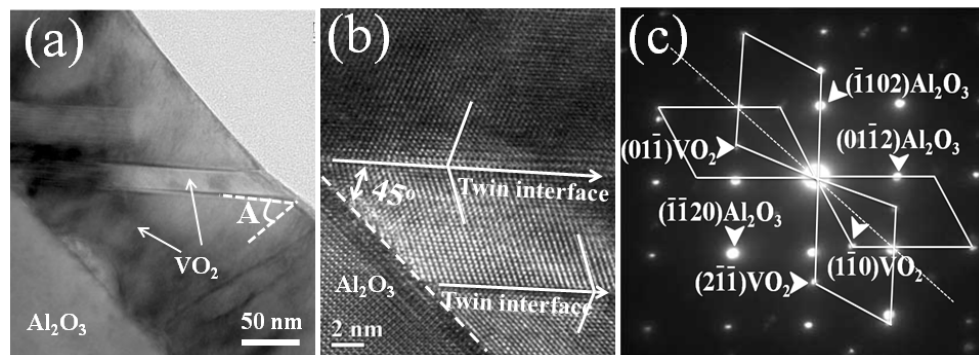


FIG. 7.7. TEM study of VO₂ on *r*-sapphire: (a) cross-sectional TEM image, (b) HRTEM image of interfacial region, and (c) SAED pattern from the VO₂-sapphire interface with sapphire in zone [2 $\bar{2}$ 01] and VO₂ from zone [111].

It is well-known that the formation of twins is to be expected if a structure phase transition takes place from a space group to another less symmetric space group. Fillingham¹² reported that VO₂ bulk crystal domains were formed upon cooling from the high-temperature tetragonal to the low-temperature monoclinic phase. This is because the monoclinic form removes the degeneracy between the two equivalent directions of the tetragonal form. Specifically for VO₂ films grown on *r*-sapphire, Yang et al.¹⁰² inferred that VO₂ was deposited at the growth temperature with (011)_T orientation in tetragonal phase; during the transformation to monoclinic phase, vanadium atoms rearrange in two ways, leading to the (200) and ($\bar{2}11$) monoclinic orientations. To verify this point, on-axis θ - 2θ XRD measurements were performed from room temperature up to 80 °C. Representative results are shown in Figure 7.6(b). In the metallic tetragonal phase measured at high temperature, the peak at 37.21° is unambiguously assigned to VO₂ (011)_T plane since the 2θ angles of other planes are far away from this value. As the temperature is reduced to room temperature, the same peak gradually shifts to 37.08°, the peak position of VO₂ ($\bar{2}11$)_M and (200)_M planes with twinned interfaces. This evidence strongly supports the hypothesis that VO₂ was deposited at the growth temperature with (011)_T orientation in the tetragonal phase, and the structural phase transformation into the low symmetric monoclinic phase results in two possible ($\bar{2}11$) and (200) monoclinic orientations. These two orientations naturally lead to the formation of the twin interfaces ((111) twins) in the film.

Figure 7.8(a) shows the on-axis θ - 2θ XRD pattern of sample M, and the three observed VO₂ peaks are assigned to ($\bar{1}02$) (33.41°), ($\bar{4}02$) (64.96°) and (202)/($\bar{2}31$) (70.51°). This result indicates that the VO₂ film on *m*-sapphire has a few orientations with ($\bar{4}02$) as the dominant. The weak diffraction intensity from Al₂O₃ [30 $\bar{3}$ 0] peak also indicates a low substrate quality. These are confirmed by the TEM results. The grain boundaries in the film can be noticed in the cross-sectional image of Figure 7.8(b). The high resolution image of Figure 7.8(c), obtained from the film/substrate interface, exhibits no clear interface, caused by the uneven surface of *m*-sapphire substrate at micro scale and possible atomic inter-diffusion between VO₂ and *m*-cut sapphire. In

spite of these, several areas in the film show good epitaxial growth of the film even though neighboring grains have different grain orientations.

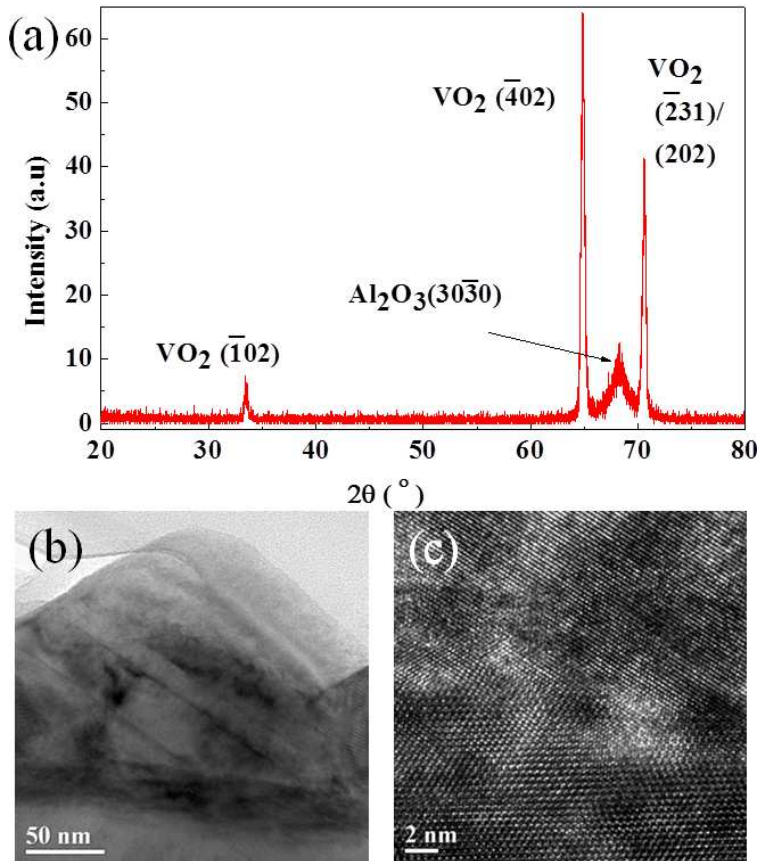


FIG. 7.8. VO_2 thin-film grown on m-cut sapphire: (a) in-plane θ - 2θ scan , Cross-section TEM image, and (c) HRTEM image of VO_2 -sapphire interfacial region.

VO_2 material quality is further confirmed by room-temperature Raman spectra, shown in Figure 7.9. From fits to the spectra for sample C, bands are observed at 195, 225, 263, 308, 339, 389, 442, 498, and 617 cm^{-1} , along with shoulders at 581 and 656 cm^{-1} . These peak positions are in agreement with previously published work.^{86, 103} The intensity variations between the samples for bands at 308, 339, 442, and 656 cm^{-1} may be due to differences in VO_2 crystal orientation. The Raman line widths are narrow, particularly at low frequency, confirming the high crystal quality. We note, however, a slight broadening of the lines for sample C, most clearly seen in the V-V band at 617

cm^{-1} . This broadening is attributed to the fine-scale grain size seen in Figure 7.3(a), and the possible presence of inhomogeneous strains in these grains. In addition, the main band near 617 cm^{-1} in samples M and R is seen to be red shifted by $\sim 4 \text{ cm}^{-1}$ relative to sample C. This is most likely due to substrate-induced strains in samples M and R, relative to C, which originate from the different epitaxial relationships between the VO_2 and sapphire under the growth conditions, and thermal expansion mismatches upon cooling to room temperature.

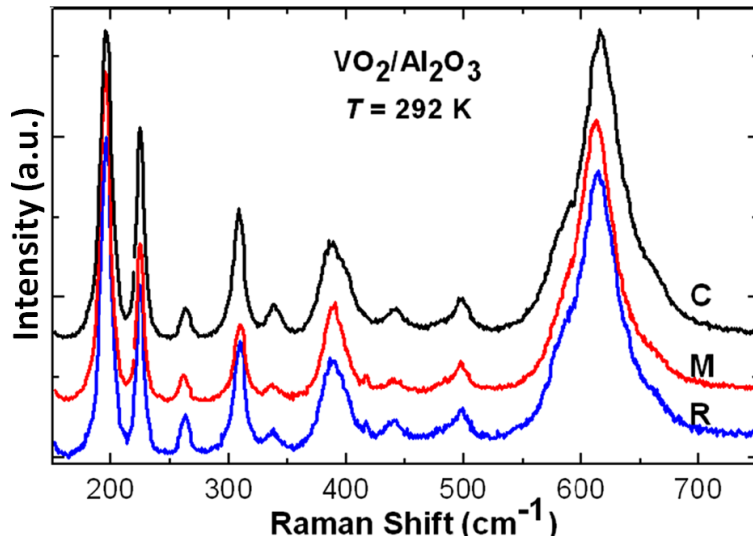


FIG. 7.9. Room-temperature measurement of Raman Spectra for the three samples.

It is widely accepted that the VO_2 thin-film MIT temperature and transition hysteresis window ΔH are closely correlated with the crystalline quality, grain size and boundary, and intrinsic strain.¹⁰⁴⁻¹⁰⁶ The substrate selection therefore has a profound effect on VO_2 MIT property.²⁴ Since the three samples reported here were grown with different epitaxial relations with respect to sapphire substrate, the built-in strain caused by the lattice mismatch is different. Muraoka et. al.²⁵ reported that T_c is directly correlated with the c -axis lattice constant: a shorter c -axis length reduces T_c below the bulk, unstrained value of 68°C (341K), while an increased c -axis lattice constant raises T_c . The slightly higher T_c (344 K) in sample C may be caused by either c -axis expansion arising from the in-plane tensile lattice mismatch²⁹ or by the porous surface. For

samples R and M, the lower T_C values of 337 K and 338 K indicate residual compressive strains are present along the c -axis. The smaller resistivity change in sample C, relative to M and R, results mainly from the higher oxygen vacancy concentration hence a relatively higher resistivity in the metallic phase.⁸⁴ The hysteresis window (ΔH) is reported to be closely related to the grain size and also to the grain boundaries. Sample C exhibits the smallest grains among the specimens investigated here, with greater dispersion in size, and a discontinuous surface. These factors result in higher barriers for metallic phase VO_2 nucleation and propagation, and hence a wider ΔH . In contrast, M- and R-samples exhibit grains which are larger and tightly connected, leading to a commensurately narrower ΔH . For THz modulation performance purposes, it is critical to reduce the background free carrier density and mobility in the insulating phase in order to minimize the insertion loss, to have a high carrier density and mobility at the metallic phase to achieve a high modulation depth, and have a minimized transition window ΔH . Comparing the three samples, VO_2 grown on the r -sapphire substrate provides the largest THz modulation performance, although the difference between them is not significant.

7.5 Summary

Pure phase VO_2 thin films were grown on c -, r -, and m -plane sapphire substrates. Surface morphology, crystal quality, and epitaxial structures were comprehensively analyzed. On c -sapphire, VO_2 was epitaxially grown in [020] direction with triple domain structure, caused by the in-plane β -angle mismatch between VO_2 and hexagonal c -sapphire. The β -angle of VO_2 and the two angles of V^{4+} - V^{4+} zigzag chain deviation from the monoclinic a_m axis were determined based on high resolution XRD Φ scans. On r -sapphire, VO_2 was epitaxially grown in the tetragonal phase with $(011)_T$ perpendicular to the growth direction, while the structural transformation to low symmetric monoclinic phase leads to the formation of $(\bar{2}11)$ and (200) orientations which forms twin structure with (111) interfaces. The result is a grain structure with 45°

tilted twin boundaries. VO₂ grown on *m*-sapphire has several orientations caused by the uneven surface of the substrate and possible inter-diffusion between VO₂ and sapphire. The R-sample shows the largest THz modulation depth during MIT while the C-sample has the smallest, in good correspondence with the measured magnitude of resistivity change. The relationship between the THz transmission performance and the MIT property with the film crystal structures was discussed. Our findings are will guide the selection of the most suitable sapphire substrate for THz modulation and other applications that employ VO₂ thin film MIT property.

Chapter 8

Tuning Properties of VO₂ Thin Films Through Growth Temperature for IR and THz Modulation

8.1 Abstract

In this part of work, the electrical and optical properties of VO₂ thin films were tuned by adjusting growth temperature to introduce varied intrinsic vacancies. A group of VO₂ thin films were grown at same condition but varied Ts (550, 575, 600, 625, 650, 675, 700 °C) via reactive sputtering and denoted as S550-S700. For all 7 samples, high resolution XRD scans revealed that VO₂ (020) contour consists of 2 distinctive sub-peaks for all 7 samples, for which one is narrow with high intensity and the other is broad with low intensity. The broad peak is assumed to be from the relatively low-quality and defected interfacial component. The position of both peaks underwent obvious shifts among different samples. Based on the R-T curves, SEM and XRD data, those 7 samples could be divided into 3 groups: G1 (S550-S600), G2 (S625-S650) and G3 (S675-S700). G1 samples show the largest insulating and metallic resistivity, good grain structures and with broad peaks on the left of narrow peak, which suggests the existence of dense vanadium vacancies; G2 samples shows reduced insulating resistivity and the smallest metallic resistivity with damped grain surface, and broad peaks located underneath narrow ones and shifted to a larger position, which indicating the whole sample is strained with less defects; G3 samples shows a further reduced insulating resistivity, with intermediate grain structure and broad peaks on the right side, suggesting the existence of abundant oxygen vacancies. Moreover, the NIR transmittance and THz-TDS unveiled that G1 samples show the largest transmittance at metallic state while G3 samples display largest transmittance at insulating state, both of which impair the optical modulation depth, giving G2 samples superior modulation

depth up to 97% both in NIR ($\lambda = 3 \mu\text{m}$) and THz range.

8.2 Introduction

Although the fundamental mechanisms that govern the metal-insulator transition (MIT) of vanadium dioxide (VO_2) has been in debate for several decades, and remains an active research topic in fundamental physics, a great deal of interest is also being devoted to VO_2 thin-film deposition control with the aim to exploit its MIT for tunable device development. Across this transition, its electronic conductivity dramatically changes by 3-5 orders, accompanied by considerable variation of its optical properties.^{89, 70, 90} The unique properties of VO_2 render it a promising candidate for tunable switching and modulation applications in infrared, terahertz (THz), and microwave wavelengths.^{47, 107, 108} Especially in the THz field, there are great needs for reconfigurable and tunable THz wave switches, filters and modulators for imaging, spectroscopy, and communication applications. However, the progress in this field is strongly limited by the modulation depth of traditional semiconductor materials and devices. Since insulating VO_2 is highly transparent between 2 to 10 μm and above 45 μm (i.e., below 6.7 THz), with very low loss mainly caused by low-density free carrier absorption, while metallic VO_2 has a high free carrier concentration ($>10^{20} \text{ cm}^{-3}$) with large absorption, VO_2 could be an ideal candidate for THz wave modulation. Previously, we have reported that THz electric field modulation depth of more than 85%, corresponding to power modulation depth of more than 95% based on VO_2 thin-film is achievable.¹⁰⁹ Since the insertion loss mainly depends on the carrier concentration in the insulating state of VO_2 while the modulation depth is critically determined by the conductivity in the metallic state, control VO_2 thin-film growth to tune its properties is critical.

Suffering from the existence of multivalent vanadium ions, it is challenging to yield pure VO_2 out of the complex VO_x compounds. For VO_2 , in addition to V^{4+} , other valence states of vanadium, particularly V^{5+} and V^{3+} are easily produced due to growth

condition random fluctuation. A lot of research efforts were devoted to growth of high quality VO₂ thin films through various techniques. However, we believe that the slight deviation from the VO₂ stoichiometry with V vacancy or O vacancy, corresponding to hole or electron doping with V⁵⁺ or V³⁺ formation, in fact, may be a powerful tool that can be exploited to engineer VO₂ thin-film electrical and optical properties for good use. With this aim, we conducted a systematic study of VO₂ thin-film sputtering deposition under a set of growth temperatures (T_s). In this Letter, we unveil the influence of T_s on the structural and electrical properties of VO₂ thin films, and hence the possibility to tune its transmission modulation at THz wavelength.

8.3. Experiments

A serial of seven VO₂ thin films, with a thickness of around 120 nm, were grown on c-cut (0001) sapphire substrate by reactive DC magnetron sputtering of a 99.95% vanadium metal target in Ar/O₂ ambient. The total gas mixture pressure was maintained at 3 mTorr with 11% O₂/Ar flow ratio. All seven samples were grown under the same condition but with a varied substrate heater temperature T_S of 550, 575, 600 , 625, 650, 675, and 700 °C, respectively (note: the substrate temperature is lower than this nominal heater temperature). These samples are denoted as S550, S575, S600, S625, S650, S675, and S700. The as-sputtered samples were characterized by high-resolution X-ray diffraction (XRD), and their surface morphologies were observed using scanning electron microscopy (SEM). The resistivity-temperature (R-T) curves were acquired by Van der Pauw method using a thermal-controllable Hall system with a temperature resolution of 0.01K. To make reliable electrodes for electrical tests, Ti (20 nm) / Au (120 nm) metal stacks were deposited by e-beam evaporation. Terahertz Time-domain spectroscopy (THz-TDS) were employed to measure corresponding optical and THz modulation performance based on transmission measurements.

8.4 . Results and Discussion

The surface morphology of these samples were observed using SEM, and are presented in Figure 8.1. All SEM images were taken at same magnification and the bar length equals 200 nm. 3 nm thin Au films were deposited on top of sample surface to avoid serious charging effect. It is obvious that growth temperature has a significant effect on the growth mode and surface morphology. We can roughly divide the seven samples into three groups, with S550, S575, and S600 as group 1 (G1), S625 and S650 as group 2 (G2), and S675 and S700 as group 3 (G3). It should be emphasized that there is no clear boundary between the groups. In fact, S675 probably locates between G2 and G3, but is categorized into G3 only for description convenience. The three samples in G1 have very rough surface with clear grain structure, and the average grain sizes are around 200-300 nm. Based on cross-sectional SEM observation (not shown here), it was found that some grains are much higher than others, resulting in the porous surface morphology. The two samples in G2 exhibit highly compact and smooth surface with fine grain structure. With growth temperature further increases, the samples in G3, especially S700, again exhibits grainy morphology with rough surface, although they do not show the porous surface as those in G1.

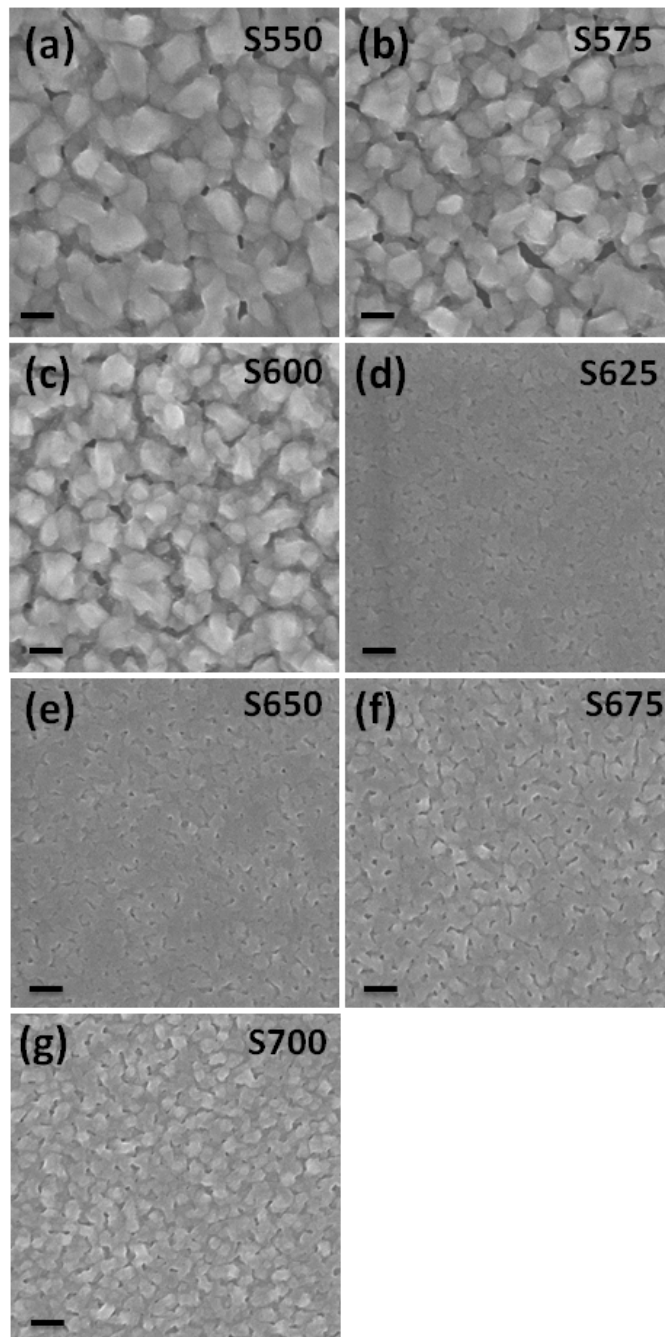


FIG. 8.1 SEM images of surface morphology for all 7 samples.

XRD measurements were conducted to unveil the influence of growth temperature on sample structure and composite properties. Figure 8.2(a) presents the typical XRD scan result with two typical peaks at $\sim 40^\circ$ and 86° that belong to VO_2 (020) and (040) reflections, together with Al_2O_3 (0006) and (00012) peaks. No other

peaks were observed, indicating the preferred growth orientation of VO₂ on c-sapphire. However, high-resolution single peak XRD scans conducted in the neighboring range of (020) peaks yield different peak contours as shown in Figure 8.2(b)-(h). The relative intensity is plotted in linear scale. Interestingly, the seven samples can also be categorized into G1-G3, same as the division based on SEM observation. Using Gaussian multi-peak simulation, each peak could be divided into a broad low-intensity peak (P2) and a relatively narrow high-intensity peak (P1). Both the contour shape and peak position of broad and narrow peaks underwent obvious shift with varied growth temperature. For S550 and S575, the broad peak centered at 39.85 ° showed up at left shoulder of the narrow peak (39.89 °); for S600, the broad peak (centered at 39.88 °) was underneath the narrow peak located at 39.89 °; while for S625-S650, the broad peaks showed up underneath the narrow peaks, but with peak position shifted up to 39.95 °; finally for S675 and S700, the broad peaks showed up at right shoulder of the narrow peak and (P2). R_{P2} is the ratio of P2 area over whole peak contour area centered at 39.98°. The change trends of P1 and P2 peak position were summarized in Figure 8.3.

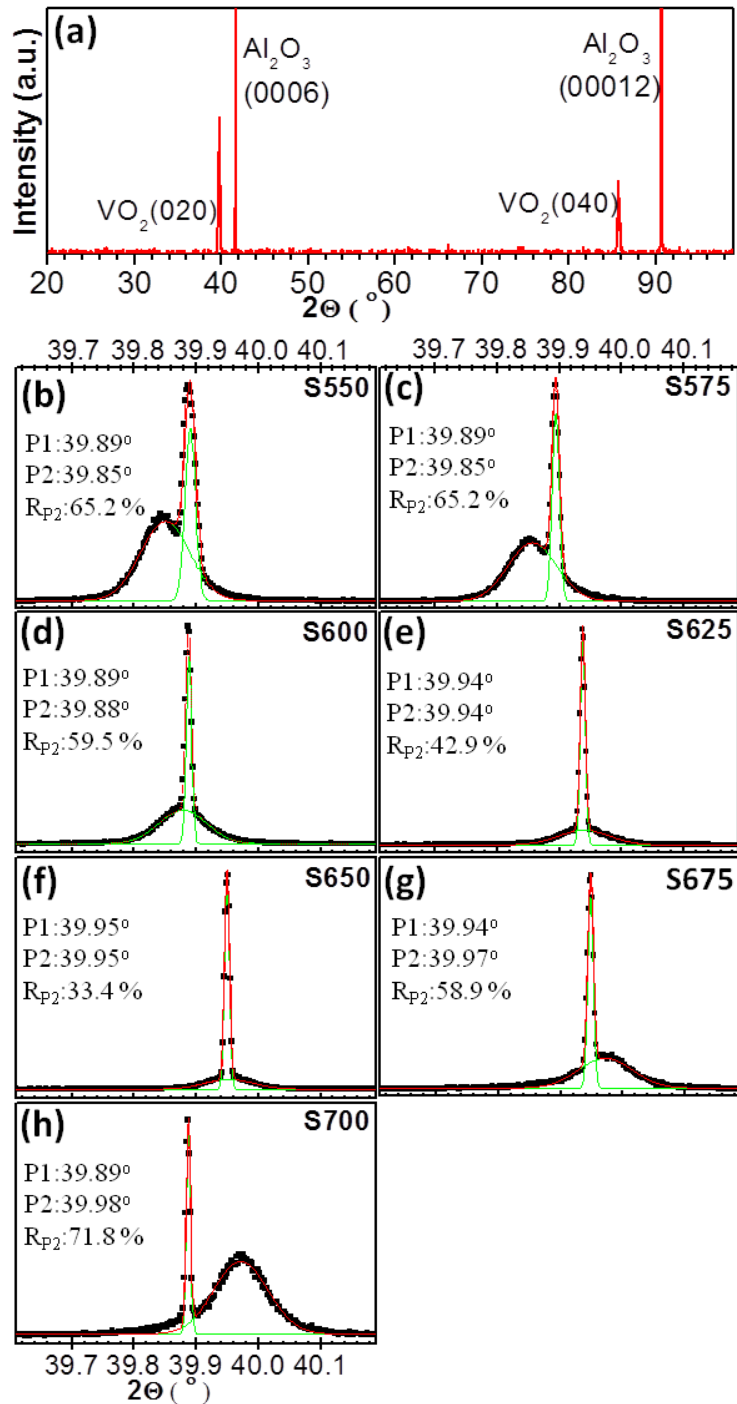


FIG. 8.2 (a) Typical XRD $2\theta-\theta$ full scan patterns for VO_2 epitaxially grown on c-cut sapphire, and (b)-(h) are high-resolution scan of VO_2 (020) peak for all 7 samples, with peak intensity normalized for comparison..

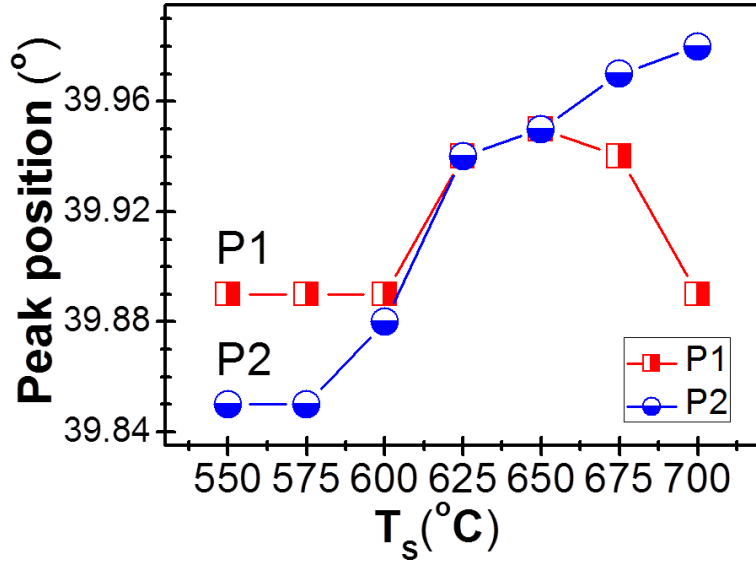


FIG. 8.3 Sub-peak position of VO_2 (020) for samples grown vs their substrate growth temperature.

The temperature-dependant resistivity (R-T) curves of all the seven samples are plotted in Figure 8.4. Symmetric Ti/Au stacks were deposited to form ohmic contacts. The inset is enlarged image of R-T curves above T_C from 3 selected samples. Except for S700, typical MIT behaviors with more than 3 orders change in resistivity were observed. In insulating state, the sample resistivity decreases as the growth temperature increases. However, they show obvious discrepancy and can also be categorized into G1-G3, with S675 at the boundary between G2 and G3. The inset in Figure 8.4 shows the metallic state resistivity of one sample as an example from each group. It is interesting to note that in metallic state, G1 has the highest resistivity and G2 has a resistivity even lower than G3.

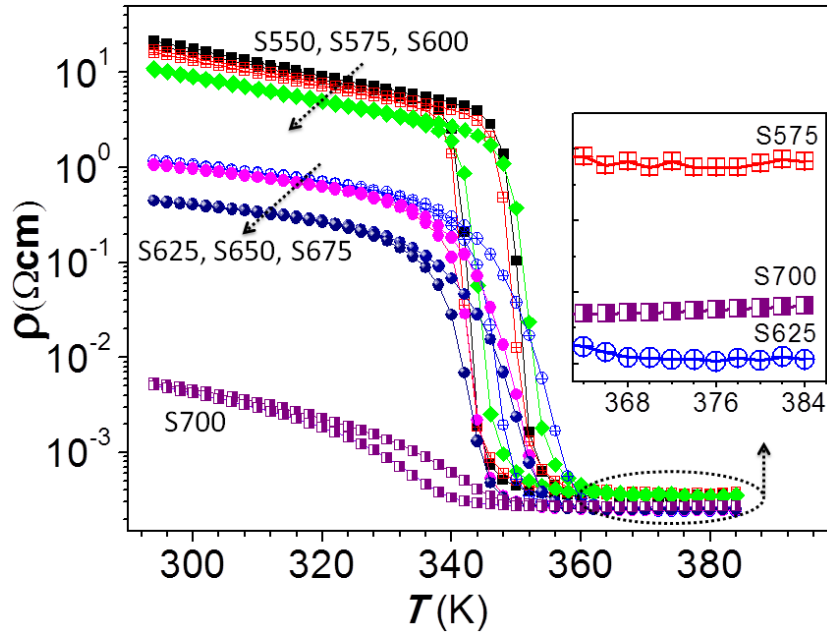


FIG. 8.4 Resistance-Temperature (R-T) curves of all 7 samples.

The structural characterization and the electrical property are clearly correlated with the samples categorized into the same three distinctive groups. The results in Figure. 8.1-8.4 can be understood from the V/O stoichiometry variation since it is anticipated that as T_s increases, V/O ratio decreases, probably due to O sticking coefficient diminishing.¹¹⁰ It is pointed out that excessive V atoms produce O vacancies (V_O^{2+}) with the defect reaction $O_O^X \rightleftharpoons V_O^{2+} + 2e' + \frac{1}{2}O_2$ (O_O^X being O in the lattice), to maintain charge neutrality, and electrons (e') are trapped at V^{4+} octahedral sites to create $V^{(4-n)+}-V^{4+}$ pairs ($n=1, 2$, or 3). Whereas, O excess generate V vacancies (V_V^{4+}) and holes (h^+) with reaction $O_2 \rightleftharpoons V_V^{4+} + 4h^+ + 2O_O^X$, and these holes are trapped at nearest-neighbor V^{4+} sites to create V^{5+} ($3d^0$) so that the $V^{4+}-V^{4+}$ pairs become $V^{5+}-V^{4+}$ pairs.¹⁶ Not shown here, the measured electron density of these samples monotonically increases with T_s , due to hole compensation from V vacancies for G1 samples and extra donated electrons from O vacancies for G3 samples, and hence it is unsurprised that the resistivity at insulation state monotonically diminishes with T_s for all the samples.

It is known that VO_2 epitaxially grows on c-sapphire with a domain structure due to its $\sim 122^\circ \beta$ angle mismatch with the sapphire hexagonal and the lattice constant mismatch.^{102, 111} Localized volume defects can be easily formed between misaligned domains and other regions to accommodate vacancies and to partially release strains. In addition to isolated vacancies, it is anticipated that when V/O ratio is relatively far away from VO_2 stoichiometry with high density of O or V vacancies formation, vacancies may pair up leading to other phases of vanadium oxides nucleated in the dominant VO_2 framework, especially considering that there exists a variety of phases between VO_2 and V_2O_5 with the general formula $\text{V}_n\text{O}_{2n+1}$, and between VO_2 and V_2O_3 with the general formula $\text{V}_n\text{O}_{2n-1}$ (Magnéli phases).¹¹² We tentatively attribute the observed XRD peaks in Figure 8.2(b-h) to this scenario. G2 samples probably were grown under relatively stoichiometric condition with less vacancy and defective density, therefore, epitaxial VO_2 is under compressive strain with its dominant peak at 39.95° , deviated from its bulk value of 39.884° . The weak and broad background peak is attributed to its minor part of low-quality component, which can also be noticed from the XRD result in our previous report.⁸⁴ It should be emphasized that even in the stoichiometric condition, fluctuation during the growth may also introduce small quantity of isolated vacancy related V^{5+} and V^{3+} states. The two clearly-separated peaks of G1 samples are the consequence of high density of V vacancies. The dominant narrow peak at 39.89° fits the bulk value of VO_2 , indicating VO_2 in relax state due to strain release by defective components that may also be in relax state and give the broad peak centered at 39.85° . It is worth to notice that of all $\text{V}_n\text{O}_{2n+1}$, V_3O_7 has its (712) pattern at 39.85° perfectly fitting this broad background peak. Although we have no unambiguous evidence that V_3O_7 minor phase does exist in G1 samples, it is reasonable to contemplate that when V vacancy (V^{5+}) density is above a certain level, phase separation might occur to minimize free energy by the formation of “pure” V^{4+} (VO_2) phase and a mixed V^{4+} and V^{5+} phase that is $\text{V}^{4+}\text{V}_2^{5+}\text{O}_7$, or V_3O_7 for G1 samples. Across the relatively stoichiometric samples in G2 with VO_2 in strained state, in the other end of vacancy spectrum, G3 samples clearly have dominant O vacancy that gives V^{3+} state. The VO_2

peak position of 39.89° of S700 indicates it is in relaxation state again with a broad background peak centered at 39.98° . Similarly, in addition to the “pure” V^{4+} (VO_2) phase, this broad peak might be assigned to the (1-17) pattern of V_8O_{15} , which is a mixed V^{4+} and V^{3+} phase ($V_6^{4+}V_2^{3+}O_{15}$). It is worth to note that in the transition from G2 to G3, sample S675 has the partially relaxed VO_2 peak at $\sim 39.92^\circ$.

The above explanation of the observed XRD patterns based on V/O stoichoimetric variation with T_s is consistent with the resistivity data in Fig. 43. As is known, of the oxides of V^{5+} , V^{4+} , V^{3+} , V_2O_5 has the highest room temperature resistance and V_2O_3 has the lowest. The room temperature resistance of G1 sample is the highest and that of G3 samples is the lowest. Furthermore, as the inset of Fig. 43 shows, above the phase transition temperature of VO_2 , G1 sample maintains the highest resistivity due to the background of insulating V^{5+} related phase. However, G2 sample but not G3 sample, has the lowest resistivity, due to the metallic VO_2 has a lower resistivity than V^{3+} related phase that exists in G3 sample.¹¹³

Tuning the electronic conductivity by vacancy related doping through T_s control directly impacts the optical signal transmission. To investigate their optical modulation performance, three represented samples: S575 (G1), S625 (G2), and S700 (G3) were studied using UV-Vis-NIR spectroscopy and Time-domain THz spectroscopy. Figure 8.5(a) shows the transmittance across the MIT process measured at a fixed wavelength of $3\ \mu m$, and Table II compares their insertion loss (IL) and modulation depth (MD). In the insulating state, S575 exhibits the highest transmittance of 81% with the lowest IL of 19%, while S700 has the lowest transmittance (33%) and highest IL (70%), corresponding to their resistivity variation. It is noticed that all samples show transmittance-temperature hysteresis curves similar to those of their R-T curves. In the metallic state, although S575 has a slightly higher resistance with a slight higher transmittance, the overall MD (93%) of S575 is comparable to the other two samples. We concluded that the VO_2 sample grown at relatively lower substrate temperature by introducing a certain amount of V^{5+} state is better choice for NIR optical modulation, beneficial from its lower IL and large MD.

On the other hand, their THZ behavior is different. THZ-TDS of the three samples were measured at insulating and metallic states. The transmitted time-domain electric field amplitudes are compared in Figure 8.5(b). Table in Figure 8.5(c) also lists THz field-amplitude based IL and MD. Although the resistivity of S575 is more than one order higher than S625, the transmitted E-fields are similar and hence both give an IL of 27%, in contrast with S700 that has a much lower IL of 38% due to its high conductance at room temperature. However, in the metallic state, a slight higher resistivity of S575 has a dramatic effect on its THz field transmission, leading to a smallest MD of 79%, in contrast to the 84% MD of S625. From these THz data we can conclude that for VO₂ based material, the most critical parameter to obtain a large MD is its conductivity in the metallic state,⁷⁰ and the resistivity in insulating state only plays a trivial role if it is at the magnitude of 1 Ωcm. Further increasing ρ by introducing V⁵⁺ state will not help. On the other hand, introducing V³⁺ to decrease insulating state resistivity may be useful for current injection based electrical control of MIT, but much low resistivity will augment IL and diminish MD. All transmittance data was normalized according to sapphire.

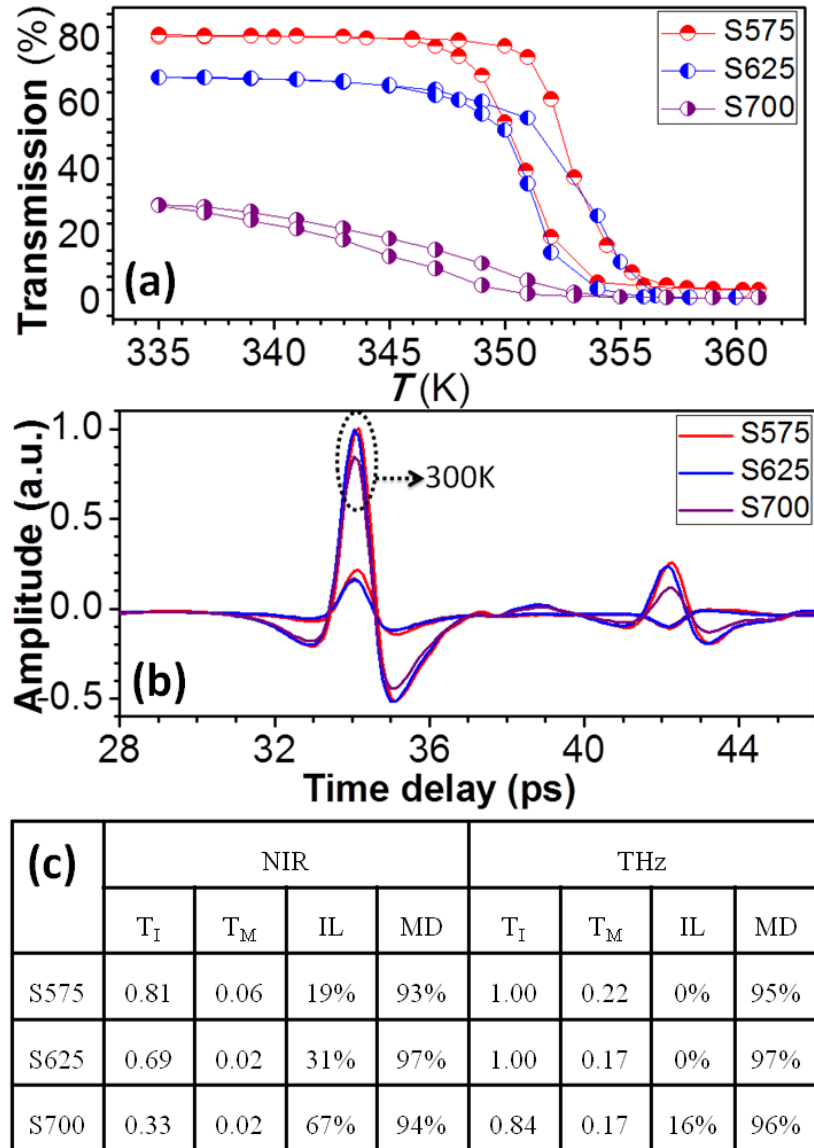


FIG. 8.5 Optical modulation performance of S575, S625 and S700:(a) NIR transmittance across the MIT process at $\lambda = 3 \mu\text{m}$, (b) THz time-domain responses at insulating and metallic states and (c) insertion loss and modulation depth calculated with data from (a) and (b).

8.5. Summary:

In summary, the electrical and optical properties of epitaxial VO_2 thin films were successfully tuned through adjusting the growth temperature T_S during sputtering process. The samples were systematically studied with combination of R-T

curves, XRD high resolution scans and SEM scans. It is found that varied T_s introduced vacancies with different density and types into samples. At relatively low T_s (550, 575 and 600 °C), lots of vanadium vacancies were introduced, and at relatively high T_s (675, 700 °C), large amount of oxygen vacancies were generated, while at 625 and 650 °C, the samples were strained with minimum intrinsic vacancies. The introduction of vacancies dramatically altered both the insulating and metallic resistivity for VO₂ thin films; moreover, the optical transmittance at insulating and metallic states also underwent commensurate modification. It is found that samples grown at intermediate temperatures, e.g., 625 and 650 °C, yield the best modulation performance at both NIR and THz range, with radiation intensity modulation depth up to $\sim 97\%$.

Chapter 9

Electric Current Controlled THz Spatial Light Modulator Based on Metal-Insulator Transition in Sputtered VO₂ Thin Films

9.1 Abstract

In this part of work, two types of multi-pixel terahertz spatial modulator (TSLM) designed and demonstrated based on metal-insulator transition (MIT) in vanadium dioxide (VO₂) thin films. Two VO₂ thin films samples with varied MIT characteristics were firstly grown under 575 °C (S575) and 625 °C (S625). The first prototype (TSLM1) was fabricated on S575, with zigzag Ti/Au wires deposited to serve as heaters, while the other one (TSLM2) was fabricated on S625, with comb-like Ti/Au wires deposited to form ohmic contacts. Both TSLM devices consist of 2×2 pixel arrays, and each pixel can be independently turned ‘off’ by external current sources. Electric current was input to generated joule heat and trigger MIT in TSLM1 pixels, while it directly controlled the transition in TSLM2 pixels. Overall, TSLM1 displayed modulation depth of around 89% in THz amplitude and TSLM2 achieved a modulation depth up to ~99%. THz-TDS based raster-scanning were conducted on both devices and yielded distinct transmission gray graphs for the ‘on’ and ‘off’ pixels, demonstrating the ability for THz spatial modulation applications.

9.2 Introduction

In the past decade, owing to the increasing demand for high-speed wireless communication,¹¹⁴ THz-ray based imaging,¹¹⁵ as well as advanced non-contact technique for materials investigation,¹¹⁶ homeland security and defense,^{117, 118} intense research interest and efforts were devoted to THz technology, and substantial

progresses were reported on THz source and detection.¹¹⁹⁻¹²¹ However, scarce progresses were reported concerning devices that could directly and conveniently modulate and process THz beam signals, suffering from the lack of natural materials that can generate considerable response to THz radiation. Kleine et al.³¹ proposed a modulator that employed the 2-dimensional electron gas (2DEG) based on high electron mobility transistor (HEMT), which yielded a limited modulation depth of around 3-4%; Fekete et al.¹²² reported an optically controlled modulation depth of ~ 50% based on photonic crystal; while majority of efforts were devoted to tunable meta-materials working in THz range,^{63, 123, 124} which could achieve modulation depth up to 50% under external stimulation.

THz spatial light modulator (TSLM), similar to its compartment of visible range light-spatial modulator,¹²⁵ is one of the aforementioned key devices that remain underdeveloped. TSLM can directly control the spatial transmission of the input THz beams, steer THz beam¹²⁶ and encode information in THz wave front.⁶⁸ To the best of our knowledge, the first demonstration of TSLM is based on active meta-materials, which is controlled by external voltage and displayed uniform modulation depth of ~ 40% for beam frequency between 0.3 to 0.4 THz.⁶⁸ Other than that, no TSLM prototype was proposed thereafter. Therefore, TSLM with good modulation performance and convenient operation at room temperature is still of great research interest. We previously reported the good THz modulation performance of VO₂ thin films across its metal-insulator transition (MIT).²⁹ Moreover, MIT in VO₂ thin films could be triggered by several factors, such as thermal heating,¹¹ electric-field / current,^{56, 75, 127} and optical excitation.⁵⁵ Taking advantage of those interesting characteristics of MIT in VO₂ thin films, two novel TSM prototypes were designed, among which one is designed to be thermally controlled and the other electrically activated.

9.3 Experiment

2 high quality epitaxial VO₂ thin films samples were grown on c-plane sapphire using magnetron sputtering technique. All growth parameters were maintained the same but with varied substrate temperatures (T_S), with one at 575 °C (S575) and the other at 625 °C (S625).⁸⁴ The resistivity-temperature (R-T) curves of both samples were measured through van der Pauw method. Two modulator prototypes, denoted as TSLM1 and TSLM2, were respectively fabricated on S575 and S625. For device fabrication, well-rinsed samples were firstly patterned into 2 × 2 pixel arrays by standard photolithography and RIE/ICP dry etch, and then second photolithography was conducted for Ti/Au wires deposition. For TSLM1, zigzag metal wires were deposited onto S575 to serve as joule heater, while for TSLM2, comb-like wires were deposited onto S625 to form ohmic contacts. Both samples were mounted onto center-hallowed test beds with contacts connected to external conducting wires by wire-bonding. Terahertz time-domain spectroscopy (THz-TDS) technique was employed to characterize modulator performance. The laser power was kept stable during all transmission measurements. THz beam was confined by ~ 1 mm diameter tapered waveguide and then directed to modulators at normal incidence. Modulators were kept on a program-controlled micro-position system and were placed very close to the waveguide tip to get uniform and focused THz radiation. It is noted that the devices were put with all their long metal wires paralleling to THz polarization to minimize their modulation effect on THz beam size.^{128, 129}

9.4 Results and discussion

Figure 9.1 (a) shows the resistivity-temperature (R-T) curves for S575 and S625 sample. Both curves shows more than 3 orders of resistivity change across the MIT, however, S625 displays a much smaller insulating resistivity (<T_C) and a relatively

smaller metallic resistivity ($>T_C$), which mainly resulted from more carriers (electrons) introduced by oxygen vacancies in S625.⁸⁴ The inset plot shows the differentials of the log (ρ) for R-T curves during heating process, which implies that S575 has a T_C of 350 K while S625 has an elevated T_C of 356 K. Taking into consideration of sharp transition slope and relatively lower T_C for S575, we chosen it for fabrication of thermally-controlled TSLM1, while S625 is chosen for electrically-controlled TSLM2 based on its higher T_C and relatively smaller insulating resistivity (less voltage required for controlling). Figure 9.1(b) displays the THz-TDS response of S575 and S625. At 300K, both two samples yielded transmitted amplitude of around 1.22, while at 363 K, S575 showed damped amplitude of 0.27 and S625 showed further reduced amplitude of 0.19, accounting for amplitude change ratios equal 4.5 and 6.4, respectively. The smaller amplitude for S625 resulted from the relatively smaller resistivity at its metallic state, which implies stronger photon scattering and absorption as described by classical Smith-Drude model.^{30,70} We noted that MIT had completed in both samples at 363K, as also indicated by the phase reverse of the reflected peaks in Figure 9.1(b).

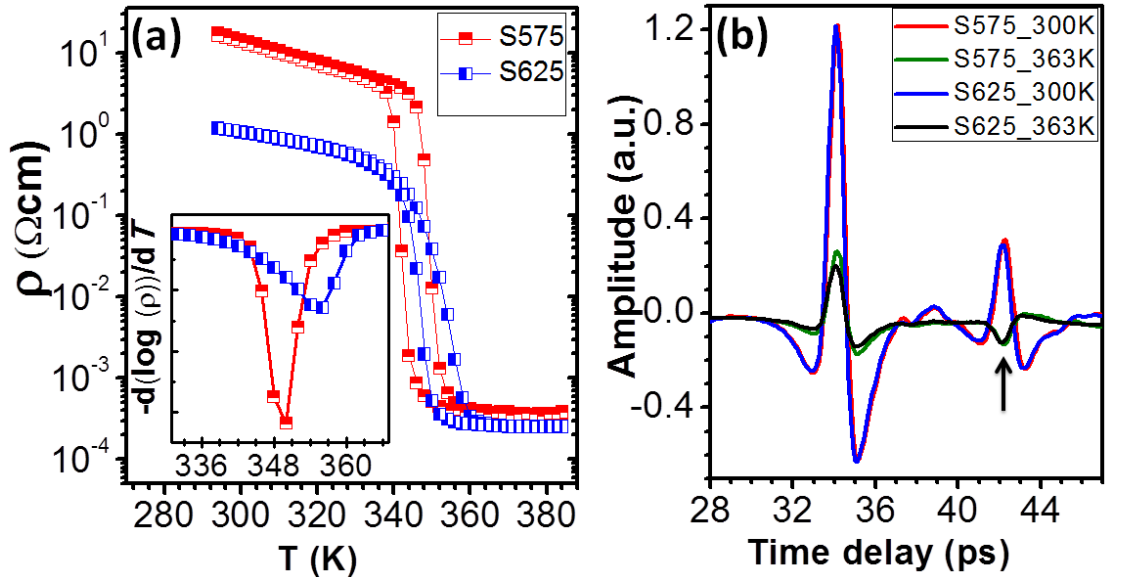


FIG. 9.1 (a) R-T curves of two VO_2 thin films samples and the inset plot shows the respective differentials of $\log(\rho)$ during heating cycle. (b) THz-TDS response of these two VO_2 thin films samples at 300K and 363K. Black arrow indicates the reflected THz peaks from the samples.

Figure 9.2(a) shows the structure diagram of a 2×2 pixel arrays based TSLM1 device. All pixels are $1 \text{ mm} \times 1 \text{ mm}$ in size and separated by $500 \mu\text{m}$ gap. $20 \mu\text{m}$ wide and 120 nm thick Ti/Au wires were uniformly deposited onto each VO_2 pixel, with $180 \mu\text{m}$ spacing between neighboring wires. External current source was applied to trigger and control MIT in selected pixels and hence alter their THz transmittance. The sharp transition slope of S575 guaranteed the possibility of large transmittance discrepancy within narrow temperature range. Figure 9.2(b) shows the THz-TDS response of one pixel to be turned off under different current conditions. The THz dominant pulse had amplitude of 0.98 in air, which dropped to 0.72 ('0 mA') and delayed in time-scale, as caused by device insertion. The transmitted dominant peak did not show obvious change until a relatively larger current value was inputted. At current input of 60 mA, 80 mA and 100 mA, the peak amplitude was damped to 0.23, 0.17 and 0.13, respectively. An amplitude modulation ratio equals 5.5 was achieved at 100 mA current input, interestingly larger than that of pure S575 (4.5). The reflected peak underwent a phase change as the current input increased up to 80 and 100 mA, implying that MIT already started in VO_2 pixel. When the input current was set at 100 mA, all 'on' pixels underwent a considerable drop in transmittance, especially for the areas close to 'off' pixel, implying that thermal dissipation heated up VO_2 around these areas close to T_C (data not shown here). To minimize the thermal cross-talk influence on device modulation performances, a reduced current value of 80 mA was selected for operation. Figure 9.2(c) shows the corresponding gray graph generated from peak amplitude data acquired from THz raster-scan. The THz transmittance across the pixel considerably damped as it was turned off by current, and ~ 4.2 folds amplitude change was achieved at current injection of 80 mA, though the modulation is not ideally uniform. The poor performance at the edge area of 'off' pixel stemmed from the relatively bigger THz beam size ($\sim 1 \text{ mm}$ in diameter) that partially went through the gap area during the scan and hence yielded a larger transmission. Suffering from the thermal diffusion from the two turned-off pixels, the transmission of the two 'on' pixels were also damped, with area closer to the 'off' pixels underwent a larger transmission drop as

told by the deeper gray color change trend. Figure 9.2(d) shows the cross-talk at 80 mA injection on neighboring pixel. The peak amplitude dropped from ~ 0.72 at 0 mA to ~ 0.54 , accounting for $\sim 25\%$ performance degrading. Overall, the device performance is acceptable with about 3 folds change in THz amplitude, accounting for $\sim 89\%$ in modulation depth.

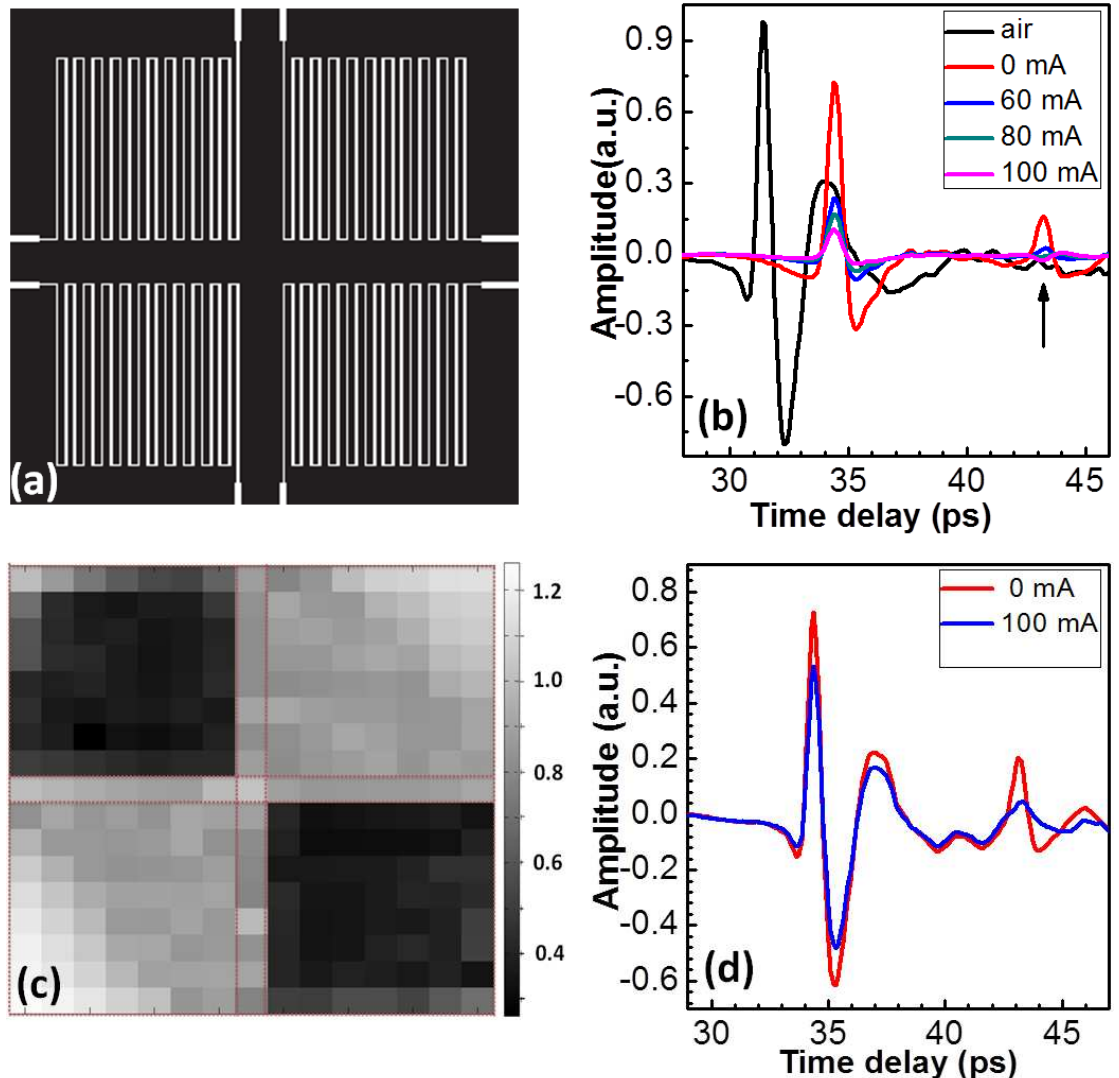


FIG. 9.2 (a) Device diagram of TSLM1. (b) THz-TDS response of the pixel with varied current injection. (c) Gray graph of THz-TDS raster-scan with 2 one pixel turned off and 0.5 mm scan step. (d) Thermal cross-talk influence on THz transmittance of ‘on’ pixel under current injection of 80 mA.

Figure 9.3(a) demonstrates the 2×2 pixel arrays based TSLM2 structure diagram,

with pixels separated by 800 μm gap. Each contact contains a wide bus-contact and a group of sub-contacts. Sub-contact wires are 40 μm in width and 50 μm in spacing, with one end connected to a 200 μm wide bus-contact. It is critical that the current input is large enough to trigger majority of VO₂ grains into metallic puddles, but should not exceed the critical current for conducting filament formation, otherwise, the appearance of filament will make non-filamentary pixel area recede back to insulating state and lose most of modulation ability.¹²⁷ The whole pixel will be completely transited into metallic state if current value is large enough to support the critical current density of filament.⁸³ However, more power will be consumed and more thermal energy will be generated to cause serious cross-talk among pixels. Therefore, a proper operation current is also critical to determine performance of TSLM2. Figure 9.3(b) displays the THz-TDS response of one pixel under current injection. The insertion of TSM2 reduced the pulse peak amplitude to around 0.58 as compared to that of 0.98 in air, which resulted from larger surface area ratio covered by metallic contacts. The transmitted pulse peak amplitude underwent negligible change even at 400 mA current injection, and it started to drop to 0.38 at 500 mA and then further decreased to \sim 0.06 at 550 mA, accounting for around 9.7 in amplitude change ratio, which is again considerably larger than that of pure S625 (6.4). The peak amplitude maintained value of around 0.06 when further increased the current injection up to 600 mA (not shown in plot), and the voltage was read to be around 2.1 volts. Figure 9.3(c) shows the gray graph of TSLM2 at step of 0.5 mm, which shows more distinctive pixel images and negligible thermal cross-talk as compared to TSLM1. Uniform modulation performance was achieved across the device with average modulation depth up to 89%. The wide bus-contacts also damped transmission at both top and bottom end area of each pixel, but did not considerably impair the overall modulation performance. Figure 9.3(d) shows the frequency domain response of THz pulses transmitted through TSLM2 at selected current injection conditions, which shows an almost uniform modulation performance from around 0.2 THz to 1.6 THz. The work frequency range is limited by the pulse frequency of our THz-TDS system as well as the detector

sensitivity, and the actual work frequency would be even broader.

It is noted that the amplitude modulation ratio for the ‘off’ pixel of TSLM2 (9.7) are superior to that of pure S625 (6.4) thin films at 550 mA, which is more interesting considering that MIT was actually not fully completed in this ‘off’ pixel. We tentatively attribute the modulation improvement to current injection, which formed series of paralleling quasi current (carriers) flows between neighboring sub-contacts, with their orientation perpendicular to THz polarization. As aforementioned, these carrier flows served similarly as wire-grating polarizer and further decreased the pixel transmittance. The amplitude modulation ratio discrepancy between ‘off’ pixel of TSLM1 (5.5) and pure S575 (4.5) is also caused by similar mechanism. Compared with TSLM2, TSLM1 is more susceptible to thermal dissipation introduced cross-talk and hence displayed deteriorated modulation performance. The relatively smaller modulation depth of S575 also impaired the modulation performance, which could be improved by growing higher quality thin films, e.g., on other substrates.¹⁰⁹ TSLM2 yields a much better modulation depth, which stemmed from the relatively larger modulation depth of S625, less thermal cross-talk influence as well as more current injection contribution. Finally, insertion loss for both modulators could be engineered and minimized by adjusting the width and spacing of metal wires in the future work, and the pixel numbers and sizes can also be scaled for specific applications.

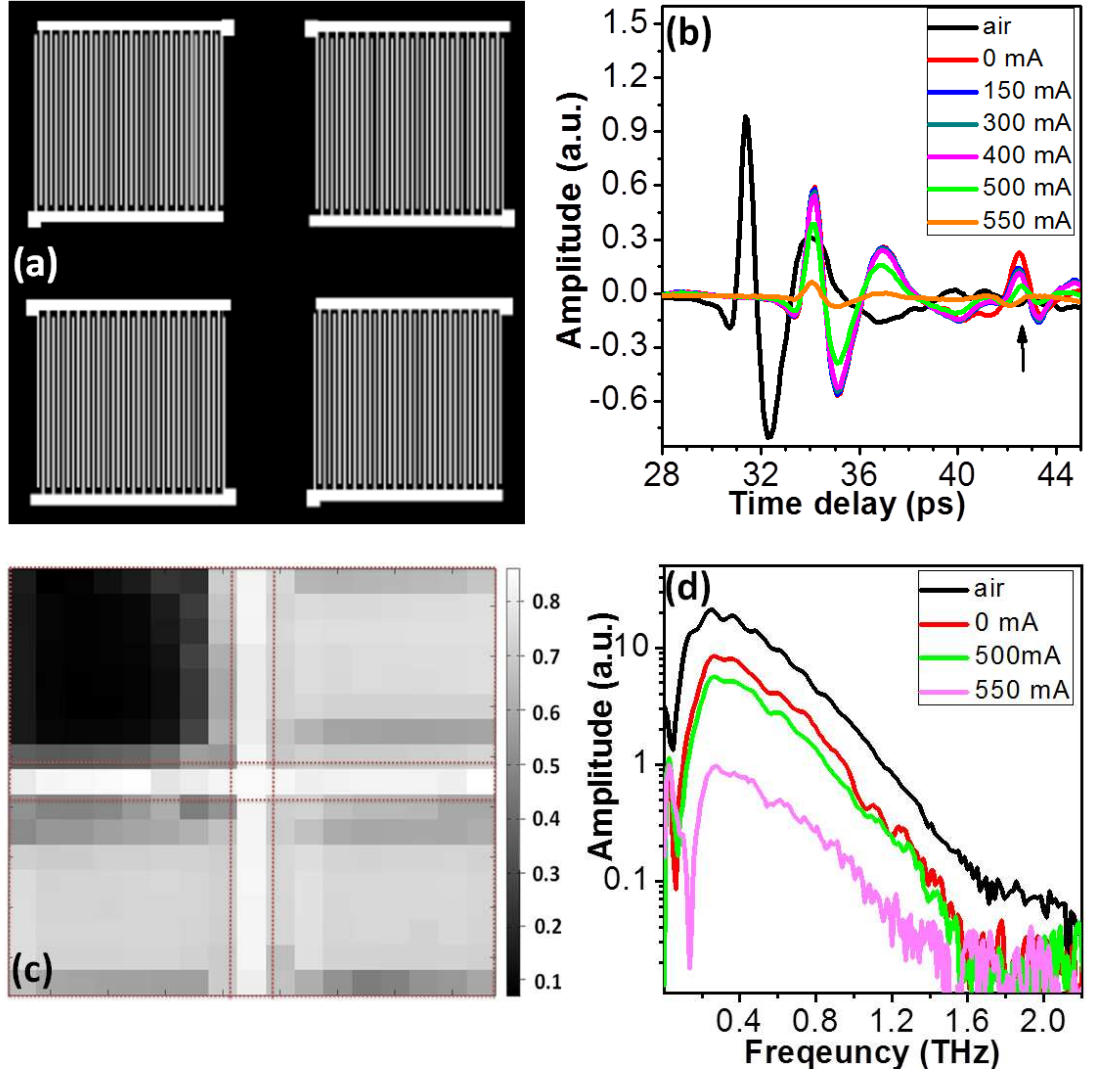


FIG. 9.3 (a) Device diagram of TSLM2. (b) THz-TDS response of the pixel under current injection. (c) Gray graph of THz-TDS raster-scan with one pixel turned off at 580 mA and 0.5 mm scan step. (d) THz response in frequency-domain at selected current value, acquired from Fourier transform of dominant peak in (b).

9.5 Conclusion

To conclude, we have demonstrated two prototypes of 2×2 THz spatial modulator (TSLM) based on VO₂ thin films. TSLM1 was formed by depositing zigzag wires onto films with higher insulating resistivity and sharper transition slope, while TSLM2 were fabricated by forming comb-like ohmic contacts onto films with relatively smaller insulating resistivity and smoother transition slope. Electric current

was input to thermally turn off TSLM1 pixels by generating joule heating, while it directly triggered MIT in TSLM2 pixels. By conducting THz raster scan under selected current input, distinct transmission gray graphs were acquired from both two modulators, which proves that the pixels could be independently controlled and uniformly modulated. Overall, TSLM1 yielded a ~89% modulation depth and TSLM2 displayed a modulation depth up to 99% across wide frequency range (0.2-1.5 THz). Both two modulators demonstrated ability to operate at room temperature and could be conveniently controlled by electric current, implying the potential applications in future THz high-speed communication, imaging processing and other THz related techniques.

Reference

1. B. G. Streetman and S. Banerjee, *Solid state electronic devices*. (Prentice-Hall, 1995).
2. N. F. Mott, *Reviews of Modern Physics* **40**, 677 (1968).
3. J. Hubbard, *Proceedings of the Royal Society of London. Series A. Mathematical and Physical Sciences* **276**, 238 (1963).
4. M. Cyrot, *Journal de Physique* **33**, 125 (1972).
5. A. Pergament, *Journal of Physics: Condensed Matter* **15**, 3217 (2003).
6. G. Grüner, *Reviews of modern physics* **60**, 1129 (1988).
7. P. W. Anderson, *Physical review* **109**, 1492 (1958).
8. F. Evers and A. D. Mirlin, *Reviews of Modern Physics* **80**, 1355 (2008).
9. Z. Yang, C. Ko and S. Ramanathan, *Annual Review of Materials Research* **41**, 337 (2011).
10. R. Heckingbottom and J. Linnett, *Nature* **194**, 678 (1962).
11. F. J. Morin, *Physical review letters* **3**, 34 (1959).
12. P. J. Fillingham, *Journal of Applied Physics* **38**, 4823 (1967).
13. V. Eyert, *Annalen der Physik* **11**, 650 (2002).
14. J. B. Goodenough, *Journal of Solid State Chemistry* **3**, 490 (1971).
15. M. M. Qazilbash, A. Schafgans, K. Burch, S. Yun, B. Chae, B. Kim, H.-T. Kim and D. Basov, *Physical Review B* **77**, 115121 (2008).
16. C. Chen and Z. Fan, *Applied Physics Letters* **95**, 262106 (2009).
17. W. W. Li, J. J. Zhu, X. F. Xu, K. Jiang, Z. G. Hu, M. Zhu and J. H. Chu, *Journal of Applied Physics* **110**, 013504 (2011).
18. S. Shin, S. Suga, M. Taniguchi, M. Fujisawa, H. Kanzaki, A. Fujimori, H. Daimon, Y. Ueda, K. Kosuge and S. Kachi, *Physical Review B* **41**, 4993 (1990).
19. D. H. Youn, J. W. Lee, B. G. Chae, H. T. Kim, S. L. Maeng and K. Y. Kang, *Journal of Applied Physics* **95**, 1407 (2004).
20. H. Futaki and M. Aoki, *Japanese journal of applied physics* **8**, 1008 (1969).
21. L. Whittaker, T. L. Wu, A. Stabile, G. Sambandamurthy and S. Banerjee, *ACS nano* **5**, 8861 (2011).

22. D. Brassard, S. Fourmaux, M. Jean-Jacques, J. Kieffer and M. El Khakani, Applied Physics Letters **87**, 051910 (2005).
23. R. Lopez, T. Haynes, L. Boatner, L. Feldman and R. Haglund Jr, Physical Review B **65**, 224113 (2002).
24. Y. Cui and S. Ramanathan, Journal of Vacuum Science & Technology A: Vacuum, Surfaces, and Films **29**, 041502 (2011).
25. Y. Muraoka and Z. Hiroi, Applied Physics Letters **80**, 583 (2002).
26. H. S. Choi, J. S. Ahn, J. H. Jung, T. W. Noh and D. H. Kim, Physical Review B **54**, 4621 (1996).
27. A. Barker Jr, H. Verleur and H. Guggenheim, Physical Review Letters **17**, 1286 (1966).
28. A. Perucchi, L. Baldassarre, P. Postorino and S. Lupi, Journal of Physics: Condensed Matter **21**, 323202 (2009).
29. C. Chen, Y. Zhu, Y. Zhao, J. H. Lee, H. Wang, A. Bernussi, M. Holtz and Z. Fan, Applied Physics Letters **97**, 211905 (2010).
30. N. V. Smith, Physical Review B **64**, 155106 (2001).
31. T. Kleine-Ostmann, P. Dawson, K. Pierz, G. Hein and M. Koch, Applied physics letters **84**, 3555 (2004).
32. A. Zylbersztein and N. F. Mott, Physical Review B **11**, 4383 (1975).
33. R. M. Wentzcovitch, W. W. Schulz and P. B. Allen, Physical review letters **72**, 3389 (1994).
34. T. M. Rice, H. Launois and J. P. Pouget, Physical review letters **73**, 3042 (1994).
35. A. Cavalleri, T. Dekorsy, H. H. W. Chong, J. C. Kieffer and R. W. Schoenlein, Physical Review B **70**, 161102 (2004).
36. H. T. Kim, Y. W. Lee, B. J. Kim, B. G. Chae, S. J. Yun, K. Y. Kang, K. J. Han, K. J. Yee and Y. S. Lim, Physical review letters **97**, 266401 (2006).
37. M. B. Sahana, M. S. Dharmaprakash and S. A. Shivashankar, Journal of Materials Chemistry **12**, 333 (2002).
38. D. H. Kim and H. S. Kwok, Applied Physics Letters **65**, 3188 (1994).
39. M. Soltani, M. Chaker, E. Haddad, R. V. Kruzelecky and D. Nikanpour, Journal of Vacuum Science & Technology A: Vacuum, Surfaces, and Films **22**, 859 (2004).
40. K. Okimura and N. Kubo, Thin Solid Films **515**, 4992 (2007).

41. B. G. Chae, H. T. Kim, S. J. Yun, B. J. Kim, Y. W. Lee, D. H. Youn and K. Y. Kang, *Electrochemical and solid-state letters* **9**, C12 (2006).
42. S. Lu, L. Hou and F. Gan, *Advanced Materials* **9**, 244 (1997).
43. K. Nagashima, T. Yanagida, H. Tanaka and T. Kawai, *Journal of applied physics* **100**, 063714 (2006).
44. K. G. West, J. Lu, J. Yu, D. Kirkwood, W. Chen, Y. Pei, J. Claassen and S. A. Wolf, *Journal of Vacuum Science & Technology A: Vacuum, Surfaces, and Films* **26**, 133 (2008).
45. F. Dumas-Bouchiat, C. Champeaux, A. Catherinot, A. Crunteanu and P. Blondy, *Applied Physics Letters* **91**, 223505 (2007).
46. S. Bonora, U. Bortolozzo, S. Residori, R. Balu and P. V. Ashrit, *Optics letters* **35**, 103 (2010).
47. T. Driscoll, S. Palit, M. M. Qazilbash, M. Brehm, F. Keilmann, B. G. Chae, S. J. Yun, H. T. Kim, S. Y. Cho and N. M. Jokerst, *Applied Physics Letters* **93**, 024101 (2008).
48. J. S. Kyoung, M. A. Seo, S. M. Koo, H. R. Park, H. S. Kim, B. J. Kim, H. T. Kim, N. K. Park, D. S. Kim and K. J. Ahn, *physica status solidi (c)* **8**, 1227 (2010).
49. B. J. Kim, Y. W. Lee, S. Choi, S. J. Yun and H. T. Kim, *Electron Device Letters, IEEE* **31**, 14 (2010).
50. J. Sakai, *Journal of Applied Physics* **103**, 103708 (2008).
51. T. Driscoll, H. T. Kim, B. G. Chae, B. J. Kim, Y. W. Lee, N. M. Jokerst, S. Palit, D. R. Smith, M. Di Ventra and D. N. Basov, *Science* **325**, 1518 (2009).
52. H. Coy, R. Cabrera, N. Sepulveda and F. E. Fernandez, *Journal of Applied Physics* **108**, 113115 (2010).
53. S. Babulanam, T. Eriksson, G. Niklasson and C. Granqvist, *Solar energy materials* **16**, 347 (1987).
54. D. Newns, J. Misewich, C. Tsuei, A. Gupta, B. Scott and A. Schrott, *Applied physics letters* **73**, 780 (1998).
55. A. Cavalleri, C. Toth, C. W. Siders, J. A. Squier, F. Raksi, P. Forget and J. C. Kieffer, *Physical review letters* **87**, 237401 (2001).
56. C. Chen, R. Wang, L. Shang and C. Guo, *Applied Physics Letters* **93**, 171101 (2008).

57. Z. Yang, Y. Zhou and S. Ramanathan, *Journal of Applied Physics* **111**, 014506 (2012).
58. M. Nakano, K. Shibuya, D. Okuyama, T. Hatano, S. Ono, M. Kawasaki, Y. Iwasa and Y. Tokura, *Nature* **487**, 459 (2012).
59. F. B. Dejene and R. O. Ocaya, *Current Applied Physics* **10**, 508 (2010).
60. J. Li and J. Dho, *Applied Physics Letters* **99**, 231909 (2011).
61. Z. P. Wu, S. Yamamoto, A. Miyashita, Z. J. Zhang, K. Narumi and H. Naramoto, *Journal of Physics: Condensed Matter* **10**, L765 (1998).
62. M. Israelsson and L. Kihlborg, *Materials Research Bulletin* **5**, 19 (1970).
63. D. Shrekenhamer, S. Rout, A. C. Strikwerda, C. Bingham, R. D. Averitt, S. Sonkusale and W. J. Padilla, *Optics Express* **19**, 9968 (2011).
64. I. Libon, S. Baumgartner, M. Hempel, N. Hecker, J. Feldmann, M. Koch and P. Dawson, *Applied Physics Letters* **76**, 2821 (2000).
65. J. Szelc, H. Rutt and Z. Moktadir, 2nd Annual Meeting on THz Measurement Techniques, London, UK, 29 Jun 2009.
66. M. C. Beard, G. M. Turner and C. A. Schmuttenmaer, *The Journal of Physical Chemistry B* **106**, 7146 (2002).
67. R. Piesiewicz, T. Kleine-Ostmann, N. Krumbholz, D. Mittleman, M. Koch, J. Schoebel and T. Kurner, *Antennas and Propagation Magazine, IEEE* **49**, 24 (2007).
68. W. L. Chan, H. T. Chen, A. J. Taylor, I. Brener, M. J. Cich and D. M. Mittleman, *Applied Physics Letters* **94**, 213511 (2009).
69. A. Gupta, R. Aggarwal, P. Gupta, T. Dutta, R. J. Narayan and J. Narayan, *Applied Physics Letters* **95**, 111915 (2009).
70. Y. Zhu, Y. Zhao, M. Holtz, Z. Fan and A. A. Bernussi, *journal of the optical society of America B* **29**, 2373 (2011).
71. M. M. Qazilbash, M. Brehm, G. O. Andreev, A. Frenzel, P. C. Ho, B. G. Chae, B. J. Kim, S. J. Yun, A. V. Balatsky, *Physical Review B* **79**, 075107 (2009).
72. M. M. Qazilbash, M. Brehm, B. G. Chae, P. C. Ho, G. O. Andreev, B. J. Kim, S. J. Yun, A. V. Balatsky, M. B. Maple and F. Keilmann, *Science* **318**, 1750 (2007).
73. D. Stroud, *Physical Review B* **12**, 3368 (1975).
74. G. Stefanovich, A. Pergament and D. Stefanovich, *Journal of Physics: Condensed Matter* **12**, 8837 (2000).

75. Y. W. Lee, B. J. Kim, J. W. Lim, S. J. Yun, S. Choi, B. G. Chae, G. Kim and H. T. Kim, *Applied Physics Letters* **92**, 162903 (2008).
76. L. Cario, C. Vaju, B. Corraze, V. Guiot and E. Janod, *Advanced Materials* (2010).
77. M. F. Becker, A. B. Buckman, R. M. Walser, T. Lepine, P. Georges and A. Brun, *Applied Physics Letters* **65**, 1507 (1994).
78. H. Guo, K. Chen, Y. Oh, K. Wang, C. Dejoie, S. A. Syed Asif, O. L. Warren, Z. Shan, J. Wu and A. M. Minor, *Nano letters* **11**, 3207 (2011).
79. H. T. Kim, B. G. Chae, D. H. Youn, G. Kim, K. Y. Kang, S. J. Lee, K. Kim and Y. S. Lim, *Applied Physics Letters* **86**, 242101 (2005).
80. A. Crunteanu, J. Givernaud, J. Leroy, D. Mardirvirin, C. Champeaux, J. C. Orlianges, A. Catherinot and P. Blondy, *Science and Technology of Advanced Materials* **11**, 065002 (2010).
81. H. T. Chen, H. Lu, A. K. Azad, R. D. Averitt, A. C. Gossard, S. A. Trugman, J. F. O'Hara and A. J. Taylor, *Optics Express* **16**, 7641 (2008).
82. K. Okimura, Y. Sasakawa and Y. Nihei, *Japanese journal of applied physics* **45**, 9200 (2006).
83. J. Sakai and M. Kurisu, *Physical Review B* **78**, 033106 (2008).
84. C. Chen, Y. Zhao, X. Pan, V. Kuryatkov, A. Bernussi, M. Holtz and Z. Fan, *Journal of Applied Physics* **110**, 023707 (2011).
85. G. I. Petrov, V. V. Yakovlev and J. Squier, *Applied Physics Letters* **81**, 1023 (2002).
86. M. Nazari, C. Chen, A. A. Bernussi, Z. Y. Fan and M. Holtz, *Applied Physics Letters* **99**, 071902 (2011).
87. J. Rozen, R. Lopez, R. F. Haglund Jr and L. C. Feldman, *Applied Physics Letters* **88**, 081902 (2006).
88. M. Imada, A. Fujimori and Y. Tokura, *Reviews of Modern Physics* **70**, 1039 (1998).
89. M. Nakajima, N. Takubo, Z. Hiroi, Y. Ueda and T. Suemoto, *Applied Physics Letters* **92**, 011907 (2008).
90. R. Balu and P. V. Ashrit, *Applied Physics Letters* **92**, 021904 (2008).
91. D. A. Masurenko, R. Kerst, J. I. Dijkhuis, A. V. Akimov, V. G. Golubev, A. A. Kaplyanskii, D. A. Kurdyukov and A. B. Pevtsov, *Applied Physics Letters* **86**, 041114 (2005).

92. M. Goldflam, T. Driscoll, B. Chapler, O. Khatib, N. Marie Jokerst, S. Palit, D. Smith, B.-J. Kim, G. Seo and H.-T. Kim, *Applied Physics Letters* **99**, 044103 (2011).
93. J. Nag, E. A. Payzant, K. L. More and R. F. Haglund, *Applied Physics Letters* **98**, 251916 (2011).
94. D. Ruzmetov, K. T. Zawilski, V. Narayanamurti and S. Ramanathan, *Journal of Applied Physics* **102**, 113715 (2007).
95. K. Nagashima, T. Yanagida, H. Tanaka and T. Kawai, *Journal of applied physics* **101**, 026103 (2007).
96. W. Rosevear and W. Paul, *Physical Review B* **7**, 2109 (1973).
97. D. Ruzmetov, D. Heiman, B. B. Claflin, V. Narayanamurti and S. Ramanathan, *Physical Review B* **79**, 153107 (2009).
98. P. U. Jepsen, B. M. Fischer, A. Thoman, H. Helm, J. Y. Suh, R. Lopez and R. F. Haglund Jr, *Physical Review B* **74**, 205103 (2006).
99. H. Roehle, R. Dietz, H. Hensel, J. Böttcher, H. Künzel, D. Stanze, M. Schell and B. Sartorius, *Optics Express* **18**, 2296 (2010).
100. I. Yamaguchi, T. Manabe, T. Tsuchiya, T. Nakajima, M. Sohma and T. Kumagai, *Japanese Journal of Applied Physics* **47**, 1022 (2008).
101. T.-H. Yang, C. Jin, R. Aggarwal, R. Narayan and J. Narayan, *Journal of Materials Research* **25**, 422 (2010).
102. T. H. Yang, R. Aggarwal, A. Gupta, H. Zhou, R. J. Narayan and J. Narayan, *Journal of Applied Physics* **107**, 053514 (2010).
103. P. Schilbe, *Physica B: Condensed Matter* **316**, 600 (2002).
104. F. C. Case, *Journal of Vacuum Science & Technology A: Vacuum, Surfaces, and Films* **2**, 1509 (1984).
105. J. Y. Suh, R. Lopez, L. C. Feldman and R. F. Haglund Jr, *Journal of Applied Physics* **96**, 1209 (2004).
106. J. Narayan and V. M. Bhosle, *Journal of Applied Physics* **100**, 103524 (2006).
107. D. J. Shelton, K. R. Coffey and G. D. Boreman, *Opt. Express* **18**, 1330 (2010).
108. M. Dragoman, A. Cismaru, H. Hartnagel and R. Plana, *Applied Physics Letters* **88**, 073503 (2006).
109. Y. Zhao, J. Hwan Lee, Y. Zhu, M. Nazari, C. Chen, H. Wang, A. Bernussi, M. Holtz and Z. Fan, *Journal of Applied Physics* **111**, 53533 (2012).
110. Y. Ningyi, L. Jinhua and L. Chenglu, *Applied surface science* **191**, 176 (2002).

111. F. J. Wong, Y. Zhou and S. Ramanathan, Journal of Crystal Growth (2012).
112. U. Schwingenschlögl and V. Eyert, Annalen der physik **13**, 475 (2004).
113. S. Yonezawa, Y. Muraoka, Y. Ueda and Z. Hiroi, Solid state communications **129**, 245 (2004).
114. J. Federici and L. Moeller, Journal of Applied Physics **107**, 111101 (2010).
115. W. L. Chan, K. Charan, D. Takhar, K. F. Kelly, R. G. Baraniuk and D. M. Mittleman, Applied Physics Letters **93**, 121105 (2008).
116. P. H. Siegel, Microwave Theory and Techniques, IEEE Transactions on **52**, 2438 (2004).
117. R. Appleby and H. B. Wallace, Antennas and Propagation, IEEE Transactions on **55**, 2944 (2007).
118. M. R. Leahy-Hoppa, M. J. Fitch, X. Zheng, L. M. Hayden and R. Osiander, Chemical Physics Letters **434**, 227 (2007).
119. B. S. Williams, H. Callebaut, S. Kumar, Q. Hu and J. L. Reno, Applied Physics Letters **82**, 1015 (2003).
120. R. Huber, A. Brodschelm, F. Tauser and A. Leitenstorfer, Applied Physics Letters **76**, 3191 (2000).
121. W. Knap, F. Teppe, N. Dyakonova, D. Coquillat and J. Lusakowski, Journal of Physics: Condensed Matter **20**, 384205 (2008).
122. L. Fekete, F. Kadlec, P. Kuzel and H. Nemec, Optics Letters **32**, 680 (2007).
123. H. T. Chen, W. J. Padilla, M. J. Cich, A. K. Azad, R. D. Averitt and A. J. Taylor, Nature photonics **3**, 148 (2009).
124. O. Paul, C. Imhof, B. Lagel, S. Wolff, J. Heinrich, S. Hofling, A. Forchel, R. Zengerle, R. Beigang and M. Rahm, Optics Express **17**, 819 (2009).
125. T. Martinez, D. Wick and S. Restaino, Optics Express **8**, 555 (2001).
126. D. Engström, J. Bengtsson, E. Eriksson and M. Goksör, Optics express **16**, 18275 (2008).
127. Y. Zhao, J. Hao, C. Chen and Z. Fan, Journal of Physics: Condensed Matter **24**, 035601 (2012).
128. K. Shiraishi, S. Oyama and C. S. Tsai, Journal of Lightwave Technology **29**, 670 (2011).
129. I. Yamada, K. Takano, M. Hangyo, M. Saito and W. Watanabe, Optics letters **34**, 274 (2009).